ABSOLUTE MEASUREMENT OF HADRONIC BRANCHING FRACTIONS OF CHARMED-STRANGE MESONS

A Dissertation

Presented to the Faculty of the Graduate School

of Cornell University

in Partial Fulfillment of the Requirements for the Degree of

Doctor of Philosophy

by

Peter Uchenna Ezenweze Onyisi

August 2008

ABSOLUTE MEASUREMENT OF HADRONIC BRANCHING FRACTIONS OF CHARMED-STRANGE MESONS

Peter Uchenna Ezenweze Onyisi, Ph.D.

Cornell University 2008

The branching fractions of decays of the D_s^+ meson normalize many measurements of processes involving charm quarks. Using 298 pb^{-1} of e^+e^- collisions recorded by the CLEO-c detector at the Cornell Electron Storage Ring, we determine absolute branching fractions for eight D_s^+ decays with a double tag technique. In particular we determine the branching fraction $\mathcal{B}(D_s^+ \to K^-K^+\pi^+) = (5.50 \pm 0.23 \pm 0.16)\%$, where the uncertainties are statistical and systematic respectively. The uncertainty in these determinations is roughly a factor of two better than previous world averages. We also search for possible *CP* asymmetries and provide partial branching fractions for kinematic subsets of the $K^-K^+\pi^+$ decay mode.

BIOGRAPHICAL SKETCH

Peter Uchenna Ezenweze Onyisi was born to Tony Onyisi and Mary Smith on 15 May 1982 in a district of the United States which, while being the seat of the federal government and having a population larger than Wyoming, has no voting representation in Congress. He followed his parents to Brazil and then Nigeria, his father's native land. This gave him an identification with sub-Saharan Africa and the British Commonwealth, a love of guarana-flavored soda and tropical thunderstorms, and an accent that you can perhaps hear if you listen carefully. His high school's best known alumnus wrote The Da Vinci Code; his university years were spent at the University of Chicago where he majored in physics and applied mathematics, to spite his friends in pure math; and he has lived the last five years as a grad student commuting up and down East Hill.

If his loving parents, who are of the humanities/social sciences persuasion, were ever surprised by his interest in the physical sciences, they never let on. In fact, they actively encouraged it. In roughly chronological order, he wanted to be an inorganic chemist, a planetary astronomer, a physicist of some kind, a computer scientist studying distributed systems, and a particle physicist. Thanks to a wonderful boss, he worked on the CDF experiment at Fermilab as an undergrad, where he learned the sociolect and the joys of meetings. A certain wanderlust brought him to Cornell and the CLEO experiment in 2003, where he wound up with a fantastic advisor. One of the fields in which he now has expertise is hadronic open-charm decays, a niche specialty if there ever was one.

Peter looks forward to the Large Hadron Collider era, where he would like nothing better than for strong electroweak symmetry-breaking dynamics to provide a new and involved spectroscopy. This not being considered likely at the moment, he is keeping his mind open.

To those who've been, those going with me, and those coming after.

And, especially, my parents.

ACKNOWLEDGEMENTS

First of all, I am very grateful to my advisor, Anders Ryd, without whose encouragement, patience, and direction this document would not exist.

It is a truth universally acknowledged that all work that emerges from large experimental collaborations owes a lot to many people. The CLEO-c detector and our understanding of the data it produced were the product of almost thirty years of the (quite literally) blood, sweat, and tears of many. The collisions were provided by the indefatigable efforts of our colleagues at CESR, and hundreds of thousands of CPU-hours were made available to me by the LEPP computer group.

This analysis particularly benefitted from the work done to understand the systematic uncertainties in the analysis of hadronic D^0 and D^+ decay branching fractions — work done largely by (in no particular order) Anders Ryd, Steve Stroiney, Werner Sun, Ian Brock, Roy Briere, and David Cassel.

I owe a huge amount to teachers and advisors official and unofficial — in particular Henry Frisch, Ed Thorndike, David Cassel, Jon Rosner, Zuming Feng, and Ruth Ugorji.

My family have always been my greatest cheerleaders, even when it was not particularly clear what I was up to.

To all the people who put up with my random walks through Wilson, and the friends who have kept me sane over the last few years, many thanks: Chanda, Matt, Sydney, Dan, Emilie, James, the Jims, Laura, Richard, Steve, Xin, David, Hanna, Jean, Karl, Werner, Brian, Eric, Jackson, Melissa, Paras, Pete, Andrew, Sarah, Jessica, Justin, Paul, Jackie, Katagiri Sensei and Bieri Sensei ...

For my entire graduate school career, I have been in one way or another funded by the National Science Foundation (in particular the Graduate Research

Fellowship I enjoyed for three years). By way of appreciation I've tried to make my impacts as broad as I can.

Finally, thanks to Hermann Zapf, who in 1948 created the Palatino typeface in which this dissertation is set.

TABLE OF CONTENTS

LIST OF TABLES

LIST OF FIGURES

CHAPTER 1

INTRODUCTION

1.1 Meson Branching Fractions and Tests of the Standard Model

The Standard Model (SM) of particle physics is the accepted theory of the behavior of fundamental forces and matter at energies below the electroweak scale, $\mathcal{O}(100\ \text{GeV})$. Confidence in the SM is gained from overconstraining the parameters of the model. These parameters, which are constants that appear in the SM Lagrangian density, determine the masses of particles and the strength of their interactions with each other. Many experimental tests of the Standard Model constitute consistency checks on the values of these parameters; ignoring recent developments in the neutrino sector, one parameter (the Higgs boson mass) remains to be measured.

As an example of such tests, consider the couplings of quarks to the weak force, mediated by the $W^{\pm}$ and Z^0 bosons. The relevant terms in the Standard Model Lagrangian are (in the formalism of [1])

$$\begin{aligned}\mathcal{L} \ni\ & \frac{ie}{\sqrt{2}\sin\theta_{\text{w}}}(W^{+}_{\mu}u^{\dagger}_{iL}V_{ij}\sigma^{\mu}d_{jL} + W^{-}_{\mu}d^{\dagger}_{jL}V^{\dagger}_{ji}\sigma^{\mu}u_{iL}) \\ & + \frac{ie}{\sin\theta_{\text{w}}\cos\theta_{\text{w}}}Z_{\mu}\left[\left(\frac{1}{2} - \frac{2}{3}\sin^2\theta_{\text{w}}\right)(u^{\dagger}_{iL}\sigma^{\mu}u_{iL}) - \frac{2}{3}\sin^2\theta_{\text{w}}(u^{\dagger}_{iR}\bar{\sigma}^{\mu}u_{iR})\right. \\ & \qquad \left. + \left(-\frac{1}{2} + \frac{1}{3}\sin^2\theta_{\text{w}}\right)(d^{\dagger}_{jL}\sigma^{\mu}d_{jL}) + \frac{1}{3}\sin^2\theta_{\text{w}}(d^{\dagger}_{jR}\bar{\sigma}^{\mu}d_{jR})\right],\end{aligned}$$

where e is the electric charge, θ_{w} is the Weinberg angle, V_{ij} is the Cabibbo-Kobayashi-Maskawa (CKM) matrix, the quark spinors are written in the mass basis, and each term is summed over the generation indices i (up-type) and j (down-type). From the Lagrangian we see that interactions with the $W^{\pm}$ connect different generations of (left-handed) quarks with amplitudes proportional to the values V_{ij}. On the other hand, Z^0 interactions do not change quark family and depend on whether the quarks are up- or down-type, but are generation-independent.

By construction the CKM matrix is unitary in the Standard Model, and $W^{\pm}$ interactions are the only perturbative processes that change quark flavor. Additional physics beyond the SM can modify either of these results. A fourth generation of quarks would have a weak mixing matrix that was unitary as a 4×4 matrix, but only a complete decoupling of the fourth generation from the other three would leave the 3×3 CKM submatrix that we observe unitary. New particles, such as a charged Higgs $H^{\pm}$, might couple different generations together, and induce new flavor-changing processes. Both of these possibilities would manifest as modifications of three-generation SM rates for weak interactions. The self-consistency of the SM can be checked by determining the magnitudes and relative phases of the CKM matrix elements in multiple processes, each of which might be sensitive to different new physics, and verifying the matrix's unitarity. Similarly, the structure of Z^0 interactions — the generation-universality, the difference in left- and right-handed couplings, the relative size of up- and down-type couplings, and the lack of flavor-changing couplings — is a necessary prediction of the SM, and could be altered by, for example, a new boson Z'^0 mixing with the Z^0. The fact that flavor-changing neutral current processes (e.g. $b \to s\gamma$ or neutral meson mixing) occur in the SM only via loops makes experimental measurements very sensitive to new interactions that may appear in loops or even contribute at tree level. Constraining the couplings in the weak interaction Lagrangian through a variety of different measurements is the main thrust of the so-called "flavor physics" experimental program.

Charm quarks provide a unique window to weak interactions. The more accessible third generation quark, the b, decays primarily through $b \to cW^-$; this weak decay provides information on the matrix element V_{cb}, and also provides

a reference against which other b decays can be measured. The c is also the heaviest up-type quark that can be produced in the decays of anything lighter than the top quark (such as the $W^{\pm}$ and Z^0); as c production is easier to identify than u production due to its mass and large but finite lifetime, it is the best probe of the up-type sector.

Measurements of decay probabilities (branching fractions) are observables that can directly probe SM parameters. The probability for a decay to a particular state X is the rate for a particular decay divided by the rate for all decays, $\Gamma_X/\Gamma_{\text{total}}$. The decay width Γ_{total} can be determined from lifetime measurements, thus allowing access to Γ_X, which depends on the amplitude squared for the process, $|\mathcal{A}|^2$. For example, $\Gamma(b \to cW^-)$ is proportional to $|V_{cb}|^2$.

Due to the confining properties of the strong force, charm quarks are never produced alone; they are always observed bound with an antiquark to form a meson, or with two other quarks to form a baryon. Therefore, in practice detection of a charm quark is detection of a hadron containing a charm quark. The ground state combinations of a charm quark with a lighter antiquark are the D^0 ($c\bar{u}$), D^+ ($c\bar{d}$), and D_s^+ ($c\bar{s}$). Combinations that are not in the ground state tend to decay via low-multiplicity strong or electromagnetic processes to these lightest states. The ground states, on the other hand, can only decay via weak processes and have a rich spectrum. Although some understanding of two-body decay processes can be obtained through quark diagram arguments (see for example Ref. [2]), precision prediction of the decay width for any given final state is still not possible except in specific cases such as $D_{(s)}^+ \to \ell^+\nu$ [3] or $D \to (K, \pi)\ \ell^+\nu$ [4]. In particular the D decay final states that are easiest to reconstruct involve multiple hadrons, and their associated branching fractions cannot currently be predicted by lattice techniques.

Table 1.1: Examples of measurements dependent on D_s^+ branching fractions for interpretation. The uncertainties listed are, in order, statistical, systematic excluding D_s^+ branching fractions, and systematic due to D_s^+ branching fractions.

Observable	Probes	Value
$\mathcal{B}(B_s^0 \to D_s^+ D_s^-)/\mathcal{B}(B^0 \to D_s^+ D^-)$	B_s^0 mixing	$1.67 \pm 0.41 \pm 0.27 \pm 0.39$ (CDF [5])
Decay constant f_{D_s}	Lattice QCD	$283 \pm 17 \pm 7 \pm 14$ MeV (BaBar [6])
$\mathcal{B}(Z^0 \to c\bar{c})/\mathcal{B}(Z^0 \to \text{hadrons})$	$Z^0 c\bar{c}$ coupling	$(172.1 \pm 2.4 \pm 1.9 \pm 0.5) \times 10^{-3}$ (LEP, SLD [7])

Table 1.1 gives examples of cases where D_s^+ decays contribute significantly to the systematic uncertainties in other measurements. It should be noted that the LEP-only average for $\mathcal{B}(Z^0 \to c\bar{c})/\mathcal{B}(Z^0 \to \text{hadrons})$ has a much larger dependence on D_s^+ branching fractions than the result quoted in the table, which is combined with a SLD result using a very different method. We see that improved precision on D_s^+ decay rates will have a direct impact on a diverse set of measurements.

1.2 Overview of D_s^+ Decays

D_s^+ mesons decay via the weak interaction, either through a three-body decay of the c quark or through weak annihilation of the c and the $\bar{s}$. The three classes of possible final states are shown in Figure 1.1. The decay $c \to (s,d)\ell^+\nu$ gives rise to a final state with a charged lepton, a neutrino, and one or more hadrons (a "semileptonic" decay), while $c\bar{s} \to \ell^+\nu$ produces only a lepton and neu-

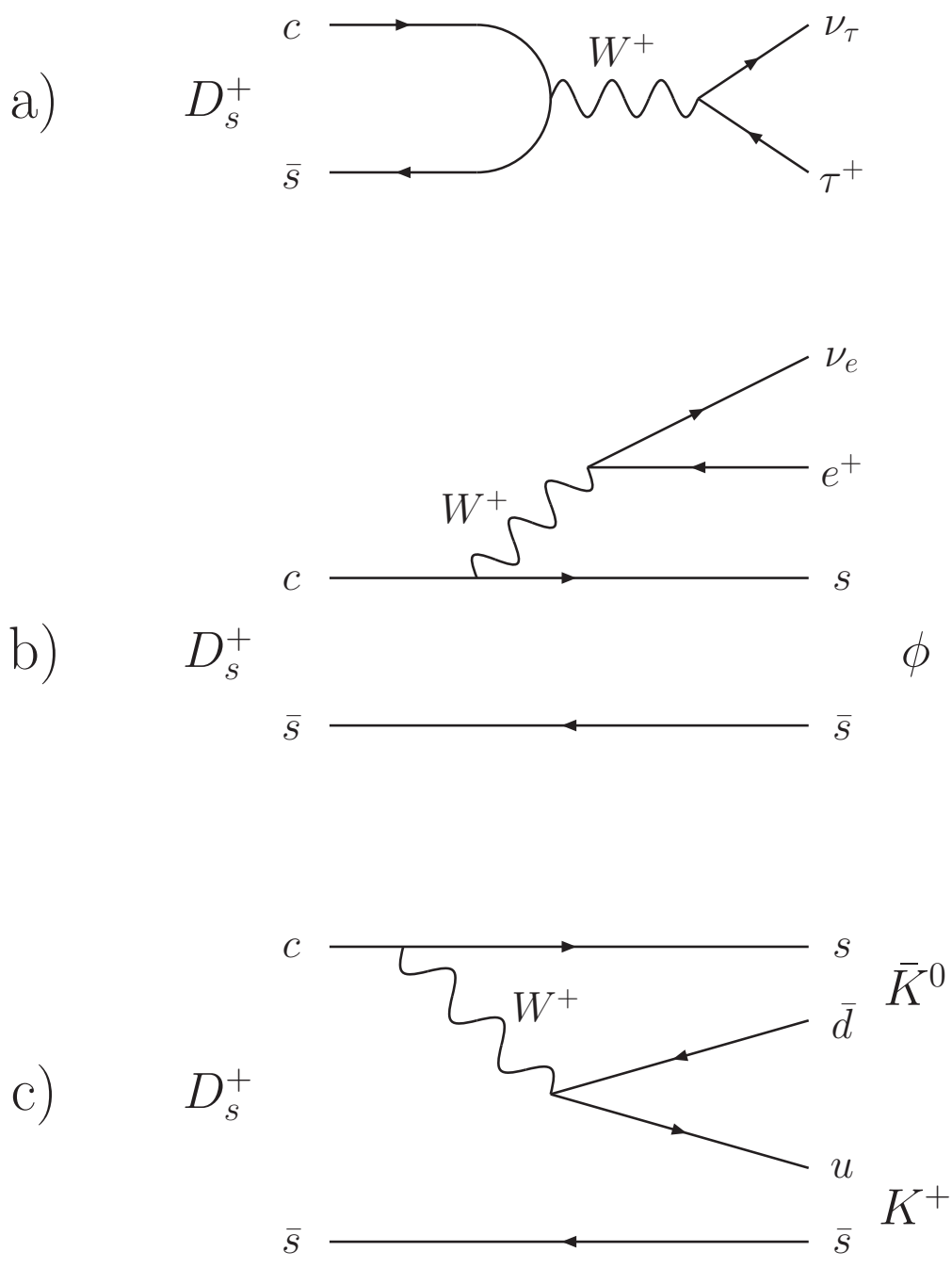

Figure 1.1: Representative quark level diagrams for the three classes of D_s^+ decays: a) leptonic, b) semileptonic, and c) hadronic. Other hadronic decays have additional topologies.

trino (a "leptonic" decay). These decays constitute a large fraction — probably around 20% — of the D_s decay width; $\mathcal{B}(D_s^+ \to \tau^+\nu)$ alone is $(6.5 \pm 0.7)\%$ [8], and while the inclusive semileptonic rate is badly-known (BES has measured $\mathcal{B}(D_s^+ \to e^+X) = (8^{+6}_{-5})\%$ [9]), known exclusive modes come close to saturating the inclusive measurement. Because of the neutrino in the final state, these decays cannot in general be fully reconstructed and are difficult to measure precisely, particularly in hadron collider or fixed target experiments where the initial state four-momentum is not known. Decays used for normalization thus tend to be ones where the W^+ decays to quarks, giving an all-hadronic final state.

In common with other weakly-decaying charm mesons, the primary hadronic decay of the charm quark in the D_s^+ is the Cabibbo-favored $c \to su\bar{d}$; there are also contributions from the Cabibbo-suppressed $c \to du\bar{d}$ and $c \to su\bar{s}$ and the doubly-Cabibbo-suppressed $c \to du\bar{s}$. In the D_s^+, there is already a $\bar{s}$ quark, so the Cabibbo-favored decay results in the presence of a $s\bar{s}$ pair. Depending on subsequent hadronization, these quarks can appear in separate strange mesons (giving a $K\bar{K}$ pair when observed), or together in mesons with large $s\bar{s}$ components (such as the η, η', ϕ, or $f_0(980)$).

The large fraction of neutral $s\bar{s}$ mesons in particular makes D_s^+ decays qualitatively different from D^0 and D^+ decays. Detectors tend to have much better momentum/energy resolution for charged particles than for photons, and backgrounds can make low-energy photon reconstruction difficult or impossible. Practically all η and η' decays involve at least one photon, making their reconstruction hard at best for a large number of experiments. This problem also affects decays with π^0 mesons.

For comparison between experiments and for normalization, a standard final state is generally chosen which is high rate and easy to reconstruct (the analogs

for the other ground state charmed mesons are $D^0 \to K^-\pi^+$ and $D^+ \to K^-\pi^+\pi^+$). In particular, for the reasons mentioned above, decays with photons are not good candidates. In addition, decays with neutral kaons are generally not used because K_L^0 is usually impossible to detect with precision and K_S^0 travels macroscopic distances before decaying. The reference mode chosen is therefore usually the lowest multiplicity Cabibbo-favored final state with all charged particles. For the D_s^+ this is $K^-K^+\pi^+$. Historically, the subset of these decays consistent with $D_s^+ \to \phi\pi^+ \to K^-K^+\pi^+$ has been used to reduce backgrounds while retaining a large fraction of the signal.

1.3 Measurement Techniques

All absolute branching fraction determinations are at heart a measurement of the ratio

$$\frac{\text{\# of decays into specific mode}}{\text{\# of mesons produced}}.$$

Frequently the hardest part of these measurements is obtaining the denominator. Before 1995 all measurements of $\mathcal{B}(D_s^+ \to \phi\pi^+)$ made model-dependent assumptions about D_s^+ production or decay properties to do so. The first model-independent measurement of $\mathcal{B}(D_s^+ \to \phi\pi^+)$ was made by BES in 1995 [10]; since then additional measurements have been obtained by CLEO-II [11] and BaBar [12, 13].

All the model-independent measurements share the use of a "tagging" technique, although of a very different kind between the BES and B-factory analyses. In a tagged measurement, a property of the event independent of the sought-after decay is used to signal the presence of the parent meson. The measurements at $\Upsilon(4S)$ energies use decays of the form $B \to D^{(*)}D_{s(J)}^{(*)+}$. By partially reconstructing

these events — using kinematic constraints to infer the presence of a D_s^+ without reconstructing its decay — these analyses can determine the denominator above.

By contrast, the BES measurement uses a charm tagging technique pioneered by Mark III for determining D^0 and D^+ branching fractions [14, 15] and for limiting $\mathcal{B}(D_s^+ \to \phi\pi^+)$ [16]. The core idea is to note that just above each threshold for charm meson pair production, the flavor-conserving properties of the strong and electromagnetic interactions require that the only allowable final states are $D^0\overline{D}^0$, D^+D^-, or $D_s^+D_s^-$. Events where a D_s^- are reconstructed thus tag the presence of a D_s^+ and provide the denominator. The BES result used data taken at a center-of-mass energy of 4.03 GeV.

The analysis presented in this dissertation uses a technique analogous to that used by BES, but at the slightly higher energy of 4.17 GeV, using the initial state $D_s^{*\pm}D_s^{\mp}$. The energy used is below the threshold for D_sDK, so it is still the case that D_s^- production signals a D_s^+ in the event, although now an additional particle (photon or π^0) from the D_s^* decay will be present as well. This work constitutes the first high-statistics measurement of D_s^+ branching fractions using $D_s^{*\pm}D_s^{\mp}$ events.

CHAPTER 2

THE CESR ACCELERATOR

The Cornell accelerator chain consists of three accelerators: a linear accelerator (linac), a synchrotron, and the Cornell Electron Storage Ring (CESR). The three accelerators are depicted in Figure 2.1. Between them, the three machines provide high luminosity collisions at a range of energies for the CLEO experiment, as well as synchrotron light for x-ray physics. A brief overview of the accelerators will be given here.

The 30 m long linac accelerates electrons emitted from a 120 kV electron gun up to 300 MeV. At the 150 MeV point, a tungsten target can be inserted into the beam; incoming electrons start electromagnetic showers in the target, and some of the positrons so produced are captured and accelerated. The produced positrons have a smaller acceleration length and exit the linac at 160 MeV. Two transfer lines, curved in opposite directions, act as spectrum analyzers to select electrons and positrons with specific momenta; these are then injected into the synchrotron.

The synchrotron accelerates the particles from the linac injection energy to the CESR storage energy. It is synchronized to the line frequency and cycles at 60 Hz (full acceleration occurs in 1/120 s). The largest energy gain occurs in this ring. Two transfer lines shunt electrons and positrons into CESR using fast kicker magnets.

The beams in CESR are highly structured. The particles in each beam are located in "bunches," with a length of around 40 ps (1.2 cm). Between three and five of these bunches follow each other at 14 ns (4.2 m) intervals; this sequence is referred to as a "train." In normal operation eight (or sometimes nine) trains are located around the ring, spaced by 220–240 ns ($\approx$ 70 m). Collisions can in principle occur at any crossing of the interaction point (IP) where both the electron and positron bunches are filled.

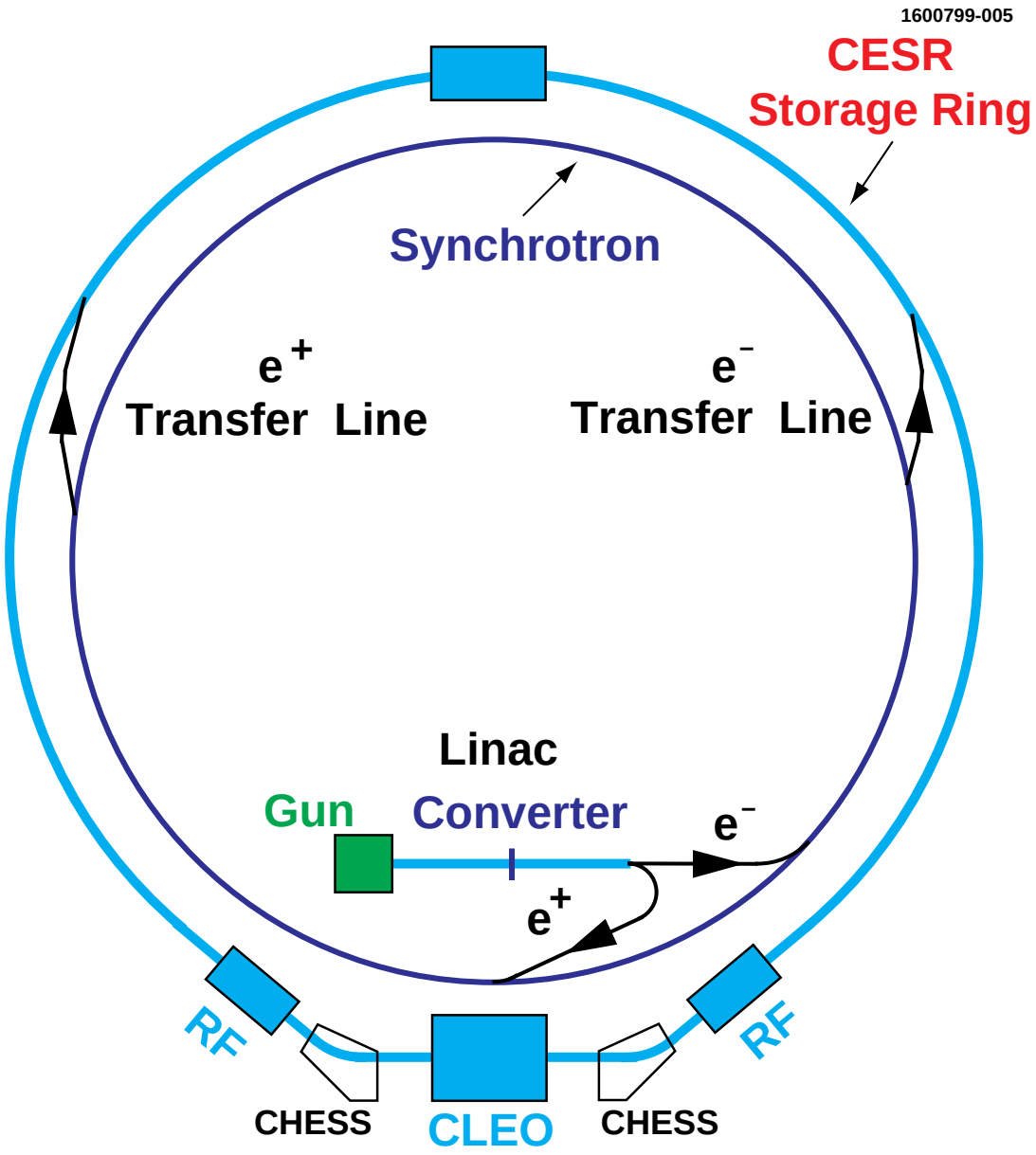

Figure 2.1: Schematic of the Cornell accelerator chain, showing the linac, synchrotron, and CESR.

CESR is a single ring device in which both electrons and positrons are stored in the same beampipe. To avoid collisions between the two beams at locations other than the CLEO IP, so-called "pretzel" orbits are used: electrostatic separators introduce opposite horizontal kicks to the electron and positron orbits near the IP; these cause oscillations around the undeflected path. The orbits are then arranged so that at any possible parasitic collision point the two beams will be separated. At the point directly opposite the ring from the IP, where even the deflected orbits would converge, vertical electrostatic separators are used to separate the beams.

Similarly, when two trains have arrived at the interaction region, efforts are made to prevent bunches from colliding at points other than the IP before the beams can be electrostatically separated. This is achieved by having the beams travel at a small angle (3 mrad) to the z axis; the beams are thus horizontally separated at the possible parasitic interaction points. This crossing angle means that particles produced in collisions will inherit a small horizontal momentum from the parent particles.

CESR was originally designed to provide collisions at center of mass energies from 9 to 16 GeV, not at charm threshold around 4 GeV. Running at lower energies produces an unusual challenge for a large e^+e^- ring. To produce beams with low emittance at high energy, CESR used the natural radiation damping of the ring: as the particle trajectories were bent by the dipole magnets, they emitted synchrotron radiation, and the lost energy was replaced by acceleration cavities. The net effect of this process was that momentum transverse to the beam direction was removed. The effectiveness of this process depends on the rate of synchrotron radiation emission, which varies with the beam energy as E^4. At low energy this process is therefore much slower, and the implied damping

times were considered unacceptable for multiple reasons. Additional radiation was induced by installing "wiggler" magnets, superconducting devices with alternating vertical magnetic fields along the beam path which cause the particles to oscillate in the horizontal plane. Radiation damping in the low energy CESR configuration is dominated by the wigglers. A wiggler-dominated ring induces a tradeoff between fast damping (which prefers high wiggler field and long field length) and low emittance (which favors the opposite). In particular the spread in the energy of the beam particles — which sets the inherent uncertainty in collisions center of mass energies — increases with the wiggler field, and was roughly 1.5 MeV in charm threshold operation (translating to a 2.1 MeV spread in the center of mass energy).

CHAPTER 3

THE CLEO-C EXPERIMENT

The CLEO-c detector is the last iteration of a series of detectors dating back to the late 1970s. For most of CLEO's lifetime, the detectors were used to pursue many topics in B, D, and bottomonium physics running at and near the $\Upsilon(4S)$. In its charm physics configuration, the main aims of the program were to provide precision tests of lattice QCD in the open charm system, to obtain precision measurements of D meson branching fractions, and to investigate charmonium spectroscopy and decays.

CLEO-c is a symmetric collider detector, with subsystems for charged particle momentum measurement and species determination, photon and electron energy measurement, and muon identification. In this chapter we describe the subdetectors most relevant to the D_s^+ hadronic branching fraction measurement. In particular the muon detection system is not discussed; muons with momentum below approximately 900 MeV/c are stopped by other detector material before reaching it, and at CLEO-c energies muons from D decays are largely below this threshold. Figures 3.1 and 3.2 show cut-away views of the CLEO-c detector, including all subdetectors discussed in this chapter.

3.1 The CLEO Coordinate System

The CLEO-c detector has an approximate cylindrical symmetry. Two coordinate systems are used to describe features of CLEO and reconstructed particle trajectories; both share an origin at the center of the detector. The first is a Cartesian system, where y is along the upward vertical, x points horizontally away from the center of the CESR ring, and z is parallel to the detector axis, pointing westward (the direction the positrons travel). The second and more commonly used system is cylindrical; this has the same z axis as the Cartesian system, a polar angle θ which is 0° in the $+z$ direction and 180° along the $-z$ direction, and an

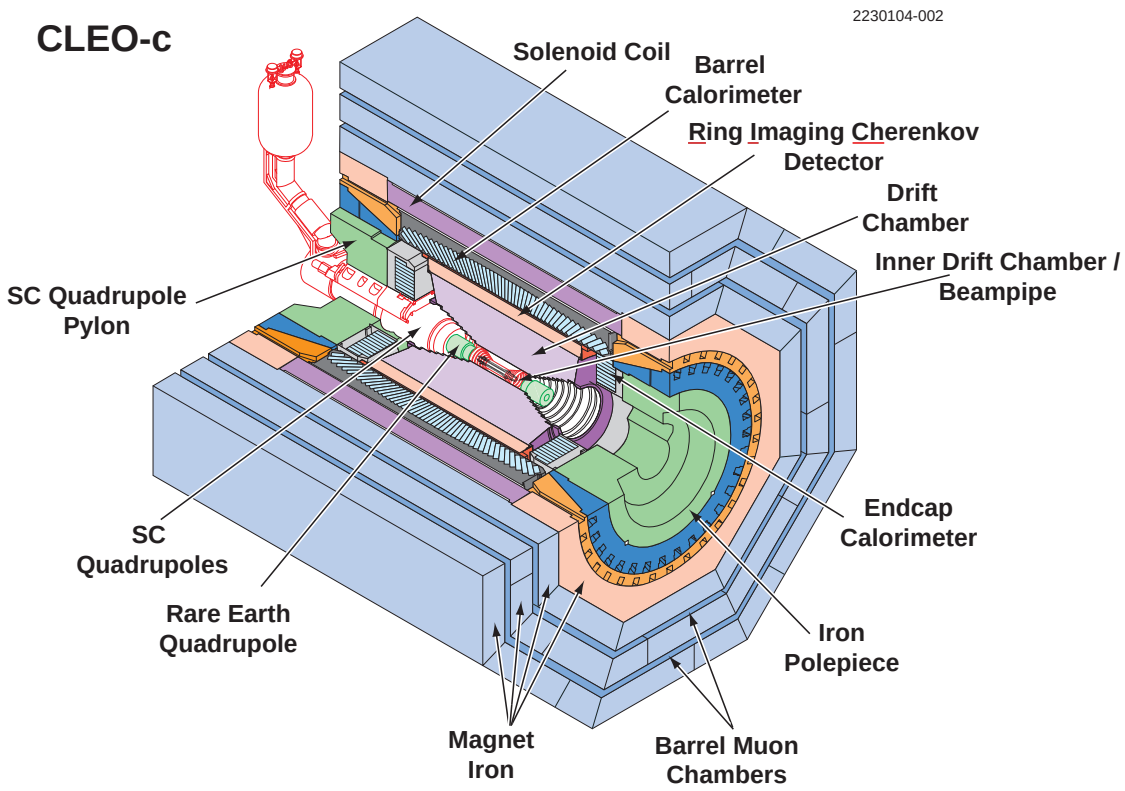

Figure 3.1: The CLEO-c detector

azimuthal angle ϕ which is zero along the $+x$ direction and from there increases towards $+y$.

3.2 Tracking System

The momenta of charged particles is measured with two concentric cylindrical drift chambers, the ZD [17] and the DR [18]. The two detectors have similar construction techniques and readout electronics. The entire tracking system is enclosed in an axial 1 Tesla magnetic field that causes the trajectories of charged particles to curve in the xy plane. The curvature is inversely proportional to the transverse momentum $p_T \equiv \sqrt{p_x^2 + p_y^2}$. Coupled with a measurement of the

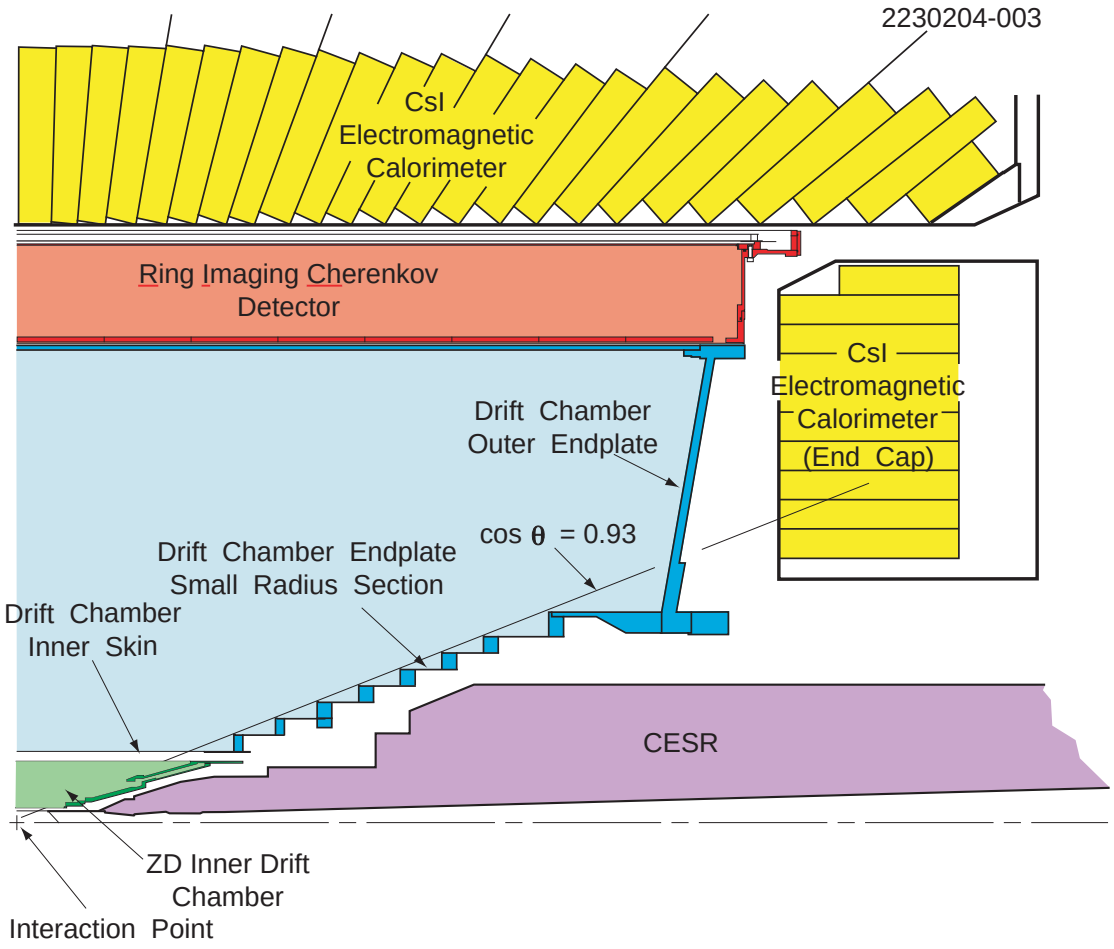

Figure 3.2: Side view of a quadrant of the CLEO-c detector

polar angle of the trajectory (which gives p_z/p_T), the full three-momentum can be reconstructed.

The basic unit in these detectors is the "cell," where a "sense" wire is surrounded by parallel "field" wires. The sense wire is held at high positive voltage relative to the field wires. In the ZD and DR, the cells have approximately square geometries, with 1.0 cm (1.4 cm) being a typical side length in the ZD (DR). Charged particles passing through the cell ionize the gas along their path; the gas used for both detectors is a 60:40 mixture of helium and propane. The liberated electrons then drift along trajectories determined by the electric field and

Lorentz forces from the magnetic field and eventually arrive at the sense wire (the drift is in the plane perpendicular to the wire except for diffusion effects). Drift chambers are operated in a regime where, for most of the drift, the speed of the electrons is largely independent of the applied electric field; for the ZD and DR that speed is approximately 28 μm/ns. When the electrons reach a region of sufficiently large electric field, they gain enough energy between collisions to ionize the gas, creating an avalanche of electrons which amplifies the signal for detection. For every point in the cell there is a nominal length of time it takes for electrons to drift from it to the sense wire and initiate an avalanche.

The detected signal gives two pieces of information. First, the time it takes for the electrons to reach the sense wire after their production can be used to precisely determine how far away from the wire the parent charged particle was; this relies on the drift velocity of the electrons being largely independent of details of the field, so electrons released at points the same distance from the wire arrive at roughly the same time. Secondly, the avalanche amplification gives a specific gain, so the charge arriving at the wire is proportional to the number of electrons liberated by the incident charged particle. The charge thus gives a measure of the energy loss rate of the incident particle in the gas (dE/dx) which is a universal function of the particle's velocity given by the Bethe-Bloch formula [19].

A given cell is only able to determine particle position in the plane perpendicular to its axis. To measure position along the axis of the cylindrical drift chamber (z), cells will be instead aligned along axes that are slightly offset from the main chamber axis. These are "stereo" cells as opposed to the "axial" cells that are aligned with the chamber. The position measured by a stereo cell will depend on a function of the particle position both perpendicular and parallel

to the chamber axis; by using layers with opposite stereo offsets (and hence different functions), the degeneracy can be broken and the z position measured.

The inner chamber, the ZD, is designed to provide z measurements close to the particle interaction vertex, while keeping the amount of material to a minimum. It has 300 sense wires arranged in six layers, with the inner and outer three having opposite stereo angles. To achieve good z resolution, the stereo angles are large (12°–15°).

The outer chamber, the DR, was designed to provide good resolution while accommodating the CESR final focus magnets that needed to be placed close to the interaction region. To achieve this, the DR endplate consists of two sections. The inner one follows the cone $|\cos\theta| = 0.93$ and includes 16 axial sense wire layers. The outer section is a much shallower cone and includes 31 stereo sense wire layers, arranged into eight superlayers of four layers each (except for the outermost superlayer which has three layers). Within each superlayer the sign of the stereo angle is the same, and the stereo direction alternates every superlayer. The stereo angles in the DR are 1.2°–1.7°. This geometry means that while tracks with $|\cos\theta| \lesssim 0.93$ will pass through all axial layers, only tracks with $|\cos\theta| \lesssim 0.83$ will pass through all stereo layers. There are a total of 9,796 sense wires.

Part of the field shaping for the outer layer of the DR is provided by a segmented cathode. The strips are instrumented and record the z position of passing particles. This information is used to further constrain the track parameters.

The detected current from each DR and ZD wire is amplified and converted to a voltage. The timing of the leading edge of the pulse is recorded (to give the time information), and the integrated size of the pulse is encoded as a time (to

give the charge information). The two signals are recorded by time-to-digital converters and read out. The known timing structure of CESR is used to help establish the time of the initial collision to turn these times into drift distances. A Kalman filter [20] provides best-fit track parameters at the particle's point of production, taking into account energy loss. The tracking system gives a momentum resolution $\sigma_p/p \sim 0.6\%$ for 1 GeV/c tracks that traverse every layer.

3.3 Ring Imaging Cherenkov System

Particle identification (PID) at CLEO-c consists of discriminating various kinds of charged particles from each other. A momentum measurement of a charged particle does not indicate if it is a pion, kaon, or electron; they can, however, be distinguished if one has access to information on the particle's velocity as well. The dE/dx measurements in the DR comprise one such measurement. The other velocity-measurement system is the Ring Imaging Cherenkov detector (RICH) [21].

The RICH lies immediately outside the DR and covers $|\cos\theta| \lesssim 0.8$. At the inner radius of the detector, charged particles pass through a 1 cm thick lithium fluoride crystal. If a charged particle's velocity exceeds the speed of ≈ 150 nm light in LiF (refractive index 1.5), Cherenkov light will be emitted in a cone with a velocity-dependent opening angle. The LiF radiators at $\theta \sim 90^\circ$ have a "sawtooth" pattern on the outer radius side to minimize total internal reflection. Electrons from Bhabha scattering produce an average of ten photons in the used wavelength range while traversing the radiators. The photons traverse a 16 cm long region filled with inert nitrogen gas, where the cone expands to measurable size. They then pass through a calcium fluoride window into region filled with a methane-triethylamine gas mixture. The photons ionize the gas, and the

resulting electrons are then amplified in a multi-wire chamber; the charges are detected via induced signals on 7.5 mm × 8 mm cathode pads. The consistency of various particle species hypotheses with the observed Cherenkov photon positions is used to compute likelihood differences between those hypotheses.

The RICH has by far the most material of any detector system in front of the calorimeter (13% of a radiation length at normal incidence). This means that a large fraction of photons produced in the initial decay will convert in the RICH system. The e^+e^- pair are spread apart in azimuth by the magnetic field as they pass through the expansion volume, and the resulting energy distribution in the calorimeter will not be reconstructed as a single good photon. This is one of the major sources of inefficiency in photon reconstruction.

3.4 Crystal Calorimeter

CLEO uses scintillating crystals in the Crystal Calorimeter (CC) for electromagnetic shower energy measurement [22]. Photons and electrons interact with the material, producing narrow, contained energy deposits. For photons this is the primary detection method.

The crystals used are made of thallium-doped cesium iodide. The crystals are 5 cm × 5 cm × 30 cm, with the long axis corresponding to over 16 radiation lengths. The crystals are arranged into three systems: the central (barrel) region and two endcaps. The crystals in the barrel are arranged in a "pseudoprojective" geometry where their axes are aligned with points close to but displaced from the interaction region, while the endcap crystals are all parallel to the z axis. The pseudoprojective arrangement means that photons are less likely to interact primarily in uninstrumented space. Although photons emitted from the origin with $|\cos\theta| < 0.95$ will hit *a* crystal, there is a gap between the barrel and the

Table 3.1: Calorimeter regions. The crystal geometry is not cylindrically symmetric in the endcap, causing the overlap between the transition and good endcap regions and the approximate boundaries.

Good Barrel	$\lvert\cos\theta\rvert < 0.82$
Transition	$0.82 < \lvert\cos\theta\rvert \lesssim 0.86$
Good Endcap	$0.85 \lesssim \lvert\cos\theta\rvert \lesssim 0.93$
Inner Endcap	$0.93 \lesssim \lvert\cos\theta\rvert < 0.95$

endcaps (for ZD, DR, and RICH services) which results in a large degradation of detection quality in the so-called "transition" region between the two subsystems. In addition the ends of the barrel region are shadowed by the RICH endplate structure which puts more material in front of the calorimeter, and similarly the DR inner radius structure shadows the endcap for $|\cos\theta| > 0.93$.

Four photodiodes mounted at the end of each crystal detect the scintillation light. The Molière radius of the crystals is 3.8 cm, while the transverse size of a crystal is 5 cm; the vast majority of the energy of an electromagnetic shower will thus be deposited in a crystal and its immediate neighbors. A photon candidate is a narrow energy deposition that is not associated with a track. Other kinds of particles can also produce a calorimeter signal: charged particles will leave an ionization trail even in the absence of other interactions, and pions and kaons, including the neutral K_L^0 have a good chance of undergoing a nuclear interaction in the crystals. Particles produced in these nuclear interactions have large mean free paths and will often interact in a different part of the calorimeter from where they were created, giving rise to "splitoff" shower candidates that can appear to be isolated from tracks. These satellite showers are a significant background to photon signals.

For showers in the good barrel and good endcap regions, the CC provides energy resolution $\sigma_E/E \sim 5\%$ at 100 MeV.

3.5 Trigger and Data Acquisition

The CLEO-c trigger [23] and data acquisition (DAQ) [24] hardware were originally developed for the requirements of high luminosity B physics.

The main roles of the trigger system are to quickly identify bunch crossings with interesting events and to determine the time of the event for tracking purposes. Although in principle collisions can occur at every bunch crossing (spaced by 14 ns), the actual collision rate is less than 100 Hz, which is well within the capacity of the DAQ system; therefore, unlike in hadron collider experiments, the criterion for "interesting event" is very loose and is primarily intended to reduce non-collision backgrounds such as interactions of beam particles with the beampipe. The CLEO-c trigger uses information from the DR and CC to make its decisions. Multiple dedicated electronics boards emit information on the track and shower topology of events; when these match any of a number of preprogrammed trigger conditions, an accept signal is asserted and, if the DAQ system is not already reading out another event, the event that caused the trigger is recorded.

The tracking trigger has two components: one looks for tracks in the inner axial wires only, while the other looks for tracks in the outer stereo layers. These two systems operate on the same principle: all patterns of hits on tracks that could be generated by tracks with transverse momenta above 133 MeV/c (axial) or 167 MeV/c (stereo) with impact parameters up to 5 mm are stored and matched against the observed patterns from every event. For the axial layers the basic unit of the pattern is an individual wire; for the stereo layers it is 4×4 blocks of wires

(each block is contained within a specific superlayer). The stereo system looks for tracks separately for the two different orientations of the superlayers. The stereo segments are then correlated with axial tracks. At the end, the tracking trigger system produces a count of axial tracks, the correlated axial+stereo tracks (generally just called "stereo tracks"), and location information.

The calorimeter trigger has to account for the fact that showers usually occupy multiple crystals, so a trigger on shower energy has to be capable of summing these together. The solution for CLEO-c is to trigger on 8×8 blocks of crystals called "tiles." Each tile shares the 4×4 block at each corner with another tile. Since showers are essentially contained within a 5×5 block, at least one tile should contain the complete shower energy. Processing is applied to try to ensure that only one full-energy hit is reported in the case of a cluster being present in multiple tiles, instead of having the same shower appear multiple times. If the hit passes one of three thresholds (low, medium, and high, set separately in the barrel and endcap regions) then it will be kept for further consideration. The thresholds in CLEO-c are set to 150, 500, 1000 MeV (150, 500, 750 MeV) for the barrel and endcap regions.

Once the low-level tracking and calorimetry information is available, an overall trigger decision can be made. A large number of possible trigger conditions ("lines") are available. Of particular interest here are

- the two track trigger, which requires two axial tracks;
- the eltrack trigger, which requires one axial track and a medium barrel shower.

Between these two triggers, essentially all usable D_s^+ events are recorded.

CHAPTER 4

D MESON RECONSTRUCTION

The reconstruction of D mesons is critical to the CLEO-c open charm program. A standard software package has been developed to provide uniform reconstruction and selection criteria to all users. In this chapter we summarize the generic D reconstruction algorithm and selections shared by many CLEO-c measurements. In Chapter 5 the specific selections used in this analysis, which are a superset of the ones in this chapter, will be discussed.

4.1 Overview

The reconstruction of short-lived particles is essentially a combinatorics problem. The basic procedure is:

- Identify all candidates for the final state daughters.
- Form all possible combinations of the daughters consistent with the decay chain. There may be constraints on allowed combinations; for example, in $D_s^+ \to K^-K^+\pi^+$ the two kaon candidates must be of opposite sign, and the same track cannot be used as both K^+ and π^+.
- Apply kinematic selection criteria (invariant mass, momentum constraints, etc.) to the reconstructed decay chain to reduce the number of bad combinations.

The final state daughters used in this analysis are $\pi^\pm$, $K^\pm$, and photons. From these we can reconstruct intermediate states: $K_S^0 \to \pi^+\pi^-$, $\pi^0 \to \gamma\gamma$, $\eta \to \gamma\gamma$, and $\eta' \to \pi^+\pi^-\eta \to \pi^+\pi^-\gamma\gamma$. When we refer to a $D_s^+ \to \pi^+\eta'$ candidate, for instance, the final state that is actually detected is $\pi^+\pi^+\pi^-\gamma\gamma$, where we have required that the $\gamma\gamma$ pair be consistent with an η decay and that a $\pi^+\pi^-\gamma\gamma$ combination be consistent with an η' decay.

4.2 K^0_S Selection

The K^0_S meson is reconstructed using its $\pi^+\pi^-$ decay, which is 69% of its decay width [19]. The K^0_S $c\tau$ is 2.7 cm; we expect many K^0_S mesons to decay a macroscopic distance away from the interaction point. For this reason we use different track selections compared to those in the next selection; the tracks are merely required to have been reconstructed properly.Tracks with opposite charges are combined together and their helix parameters and error matrices are used in a constraint where the two tracks are forced to originate at a common vertex, which may be displaced from the beamspot. If a valid solution ($\chi^2 < 1000$) is found, new initial momentum values are found for the tracks, and an invariant mass is computed; if this is consistent with the true K^0_S mass the candidate is accepted and a K^0_S four-vector is evaluated using the revertexed track momenta. A plot of K^0_S candidate mass is shown in Figure 4.1. For generic candidates, the reconstructed dipion mass $M(K^0_S)$ must satisfy 467.7 MeV/c^2 $< M(K^0_S) <$ 527.7 MeV/c^2; in this particular analysis the requirements are stricter, as described in Section 5.6.1.

4.3 Charged Track Selection

There are two classes of selections applied to tracks. First, basic quality selections are imposed to choose only reasonably-measured tracks. Second, tracks that are consistent with pion or kaon hypotheses are chosen, with the remaining tracks receiving no further consideration.

The track quality selections are listed in Table 4.1. Tracks are generally not reconstructed below 50 MeV/c, and tracks genuinely from D decays are kinematically forbidden from having momentum much above 1 GeV/c, so the

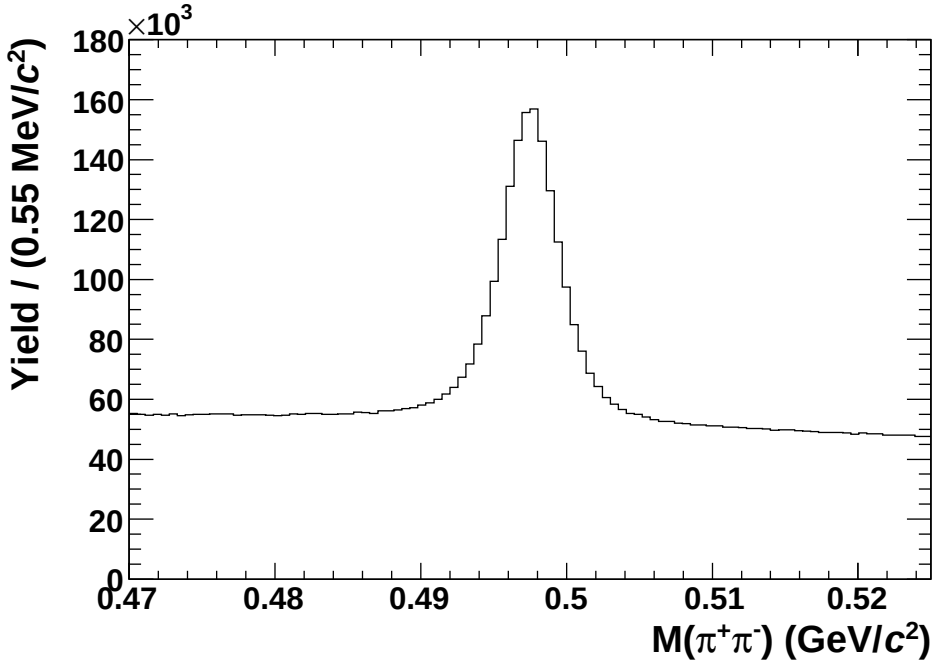

Figure 4.1: Invariant mass of K^0_S candidates in D^+_s dataset

momentum requirements are very loose. Similarly few tracks are found with $|\cos\theta| > 0.93$ due to the DR geometry; those that are are badly measured, so we restrict the acceptance. The track fit must return a reasonable χ^2, and at least half of the layers that the track is expected to traverse should have reconstructed hits. Finally the track should approach within 5 mm of the beamspot in the xy plane (d_b) and within 5 cm in the z direction (z_0).

Particle species selection proceeds as follows. Information from the PID systems is used to determine how consistent tracks are with various hypotheses. From the dE/dx measurement we obtain a residual of the observed energy loss to that expected for the given hypothesis, normalized by the known resolution of the measurement; for pions and kaons this value is denoted σ_π and σ_K, respectively. The observed Cherenkov photons in the RICH are used to compute

Table 4.1: Quality requirements for $\pi^{\pm}$ and $K^{\pm}$ candidates from the primary vertex.

$0.050\ \text{GeV}/c \leq \lvert\mathbf{p}\rvert \leq 2.0\ \text{GeV}/c$
Fit $\chi^2 < 100000$
$\lvert\cos\theta\rvert \leq 0.93$
Hit fraction ≥ 0.5
$\lvert d_b\rvert \leq 5$ mm
$\lvert z_0\rvert \leq 5$ cm

minus log likelihoods for pion and kaon hypotheses, termed L_π and L_K (note that these are more negative the more consistent they are with the hypothesis).

RICH information is only used for tracks with momentum above 700 MeV/c and with $|\cos\theta| < 0.8$, to avoid efficiency losses for slow tracks and for tracks near the edge of the acceptance. If neither dE/dx nor RICH information is available for a track, the track can be used as either a pion or a kaon. If dE/dx information is available, it must be consistent with the considered hypothesis within 3σ. A likelihood difference $\mathcal{L}$ is then formed. If only dE/dx information is being used, $\mathcal{L} = \sigma_\pi^2 - \sigma_K^2$; if RICH information is used as well, $\mathcal{L} = \sigma_\pi^2 - \sigma_K^2 + L_\pi - L_K$. The track is identified as a pion (kaon) if $\mathcal{L} \leq 0$ (≥ 0). Finally, if RICH information is used, the pion or kaon hypothesis must associate at least three photons with the track. The efficiencies and fake rates induced by this selection are shown in Figure 4.2. The efficiencies are above 85% and fake probabilities below $\sim 5\%$ for the entire kinematic range of interest.

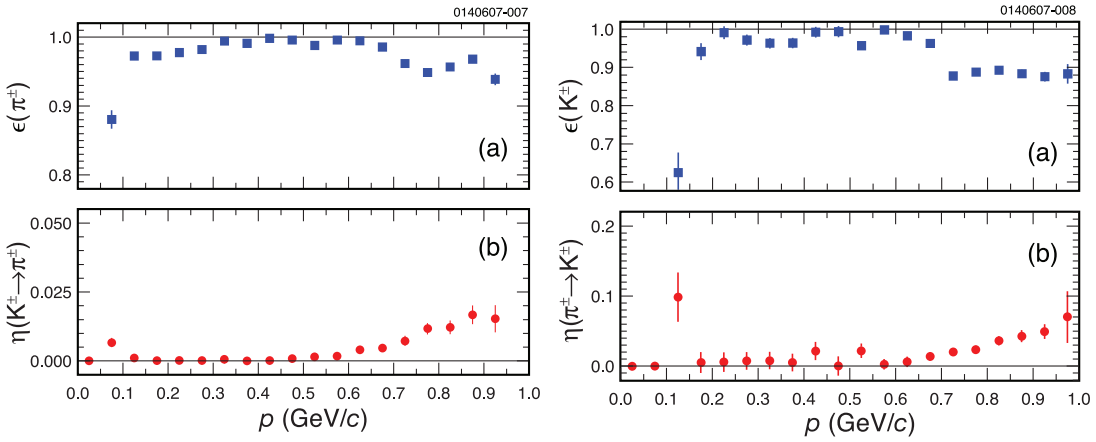

Figure 4.2: Performance of the particle identification system and selection as a function of momentum, averaged over fiducial tracking volume. Top left: efficiency for correct pion identification; bottom left: probability for a kaon to be identified as a pion; top right: efficiency for correct kaon identification; bottom right: probability for a pion to be identified as a kaon. Plots on left and right have different scales.

4.4 Selection of π^0 and η Candidates

Both π^0 and η candidates are detected in their two photon decay mode. This is 99% of all π^0 decays and 39% of η decays [19]. A plot of the $\gamma\gamma$ mass distribution is shown in Figure 4.3.

The showers used come from either the good barrel or good endcap regions, and must have $E \geq 30$ MeV. The showers considered may not include crystals that have been flagged as noisy during that run range. Any shower that is "track-matched" is rejected; a track is matched to a shower if its point of closest approach in 2D to the shower is within a cylinder 8 cm in radius and 15 cm long (with axis pointing at the detector center) around the estimated shower maximum position. The invariant mass of the two photons is then constrained to the appropriate parent mass. The covariance matrix used in this procedure is obtained from predetermined parametrizations of the energy and position

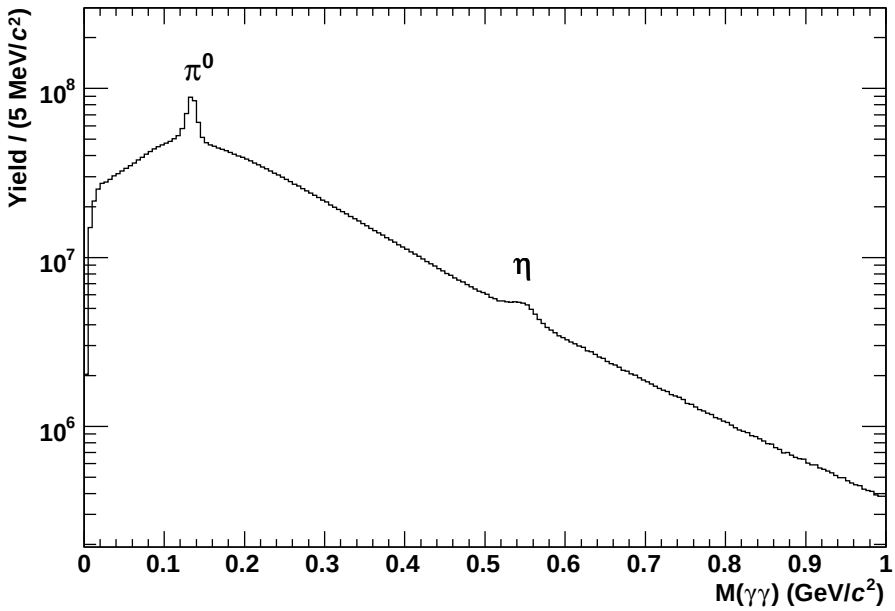

Figure 4.3: Invariant mass of shower pairs in D_s^+ dataset, showing π^0 and η signals

uncertainties. The constraint procedure is required to converge, and the χ^2 of the fit must be less than 10000.

Finally, the covariance matrix of the measured shower four-vectors can be used to determine an uncertainty on the unconstrained mass of the candidate, $\sigma_{M(\gamma\gamma)}$. The "pull mass" Δ can then be defined in terms of the unconstrained mass $M(\gamma\gamma)$ and the nominal mass $M_{(\pi^0,\eta)}$ by

$$\Delta \equiv \frac{M(\gamma\gamma) - M_{(\pi^0,\eta)}}{\sigma_{M(\gamma\gamma)}}.$$

We require $|\Delta| \leq 3$; this has the effect of a $M(\gamma\gamma)$ selection with boundaries that depend on how well it should have been measured. For all further use, the π^0 or η is considered as a single object, with a four-vector determined from the results of the mass constraint.

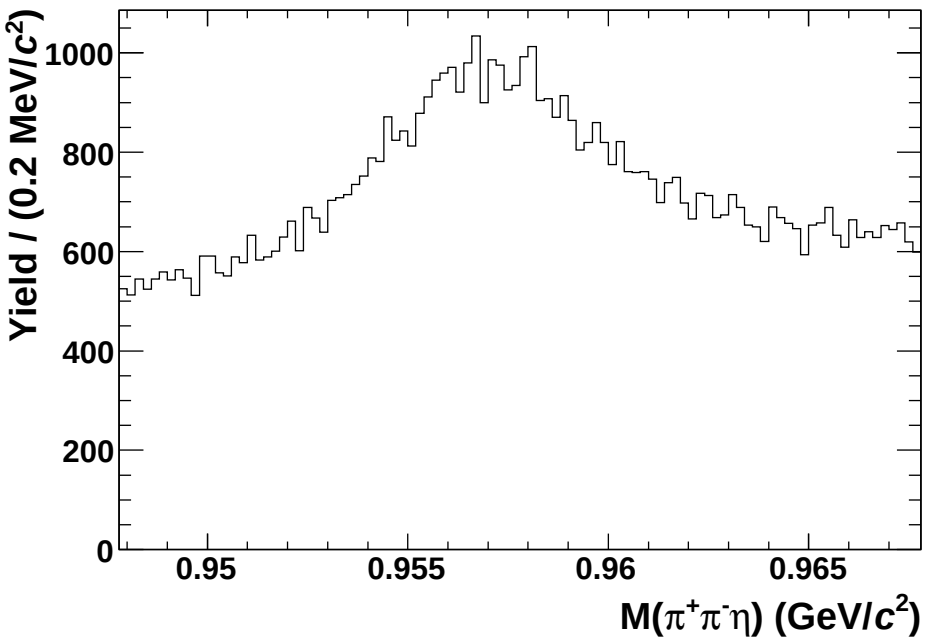

Figure 4.4: Invariant mass of η' candidates in D_s^+ dataset

4.5 Selection of η' Candidates

All η' candidates used in this work were reconstructed in the decay $\eta' \to \pi^+\pi^-\eta \to \pi^+\pi^-\gamma\gamma$. The pions used were required to pass the track quality and particle identification selections listed in section 4.3; the η candidates were those that result from the selections in section 4.4. Since the η is mass-constrained, the resolution in the η' candidate invariant mass is dominated by the pion momentum resolution. Candidate η' mesons must satisfy 947.8 MeV/c^2 < $M(\pi^+\pi^-\eta)$ < 967.8 MeV/c^2; the mass distribution is shown in Figure 4.4.

Other analyses also use the decay mode $\eta' \to \gamma\rho^0$, which suffers from more background. Candidates in this mode have 920 MeV/c^2 < $M(\pi^+\pi^-\gamma)$ < 995 MeV/c^2, 500 MeV/c^2 < $M(\pi^+\pi^-)$ < 1 GeV/c^2, and contain photons from only the good barrel or endcap regions.

4.6 Final D Candidate Selection Criteria

After the set of possible D daughters has been selected using the above criteria, they are combined together to see if they form viable candidates for each one of a long list of possible decay modes. A loose preselection of these D candidates is applied before further analysis; the imposed requirements are listed below.

The momentum and energy of D candidates are measured very differently and probe different aspects of the reconstruction. Momentum is the primary measured quantity for charged particles, and while it is the energy and flight direction of photons that is measured, the photon hypothesis requires $E = |\mathbf{p}|$. The momentum of a D candidate is the sum of the momenta of its daughters (accounting for any intermediate mass constraints that have been applied), and is largely independent of PID hypotheses for the charged daughters. On the other hand, the energy of charged daughters is established using $E = \sqrt{\mathbf{p}^2c^2 + m^2c^4}$; the masses come from PID hypotheses. The resolution on the energy of a D candidate depends on how much kinetic energy the daughters have, since the daughter masses are much better known than the momenta; the resolution in $D^0 \to K^-\pi^+$ is much worse than for $D^0 \to K^0_S\phi \to \pi^+\pi^-K^+K^-$.

We want to use the energy and momentum as two separate tests for the quality of D candidates. Different methods are used in the initial candidate selection for "high"- (beam energy above 1.9 GeV) and "low"-energy running. Low-energy running uses the variables ΔE and $M_{\rm BC}$, defined as

$$\Delta E \equiv E_D - E_{\rm beam}, \quad M_{\rm BC}c^2 \equiv \sqrt{E^2_{\rm beam} - \mathbf{p}^2_D c^2}.$$

These variables manifestly depend separately on E_D or $\mathbf{p}_D$, and for real D candidates are expected to peak at $\Delta E = 0$, $M_{\rm BC} = M_D$. The requirements imposed on all candidates are $|\Delta E| < 100$ MeV, $M_{\rm BC} \geq 1.83$ GeV/c^2.

It is high-energy running that is relevant for this thesis. In this regime ΔE no longer peaks at zero for most D production mechanisms as there are now extra pions and photons in the event. We replace it as a discriminating variable with the invariant mass M_D,

$$M_D c^2 \equiv \sqrt{E_D^2 - \mathbf{p}_D^2 c^2}.$$

It is required that M_D be within 85 MeV/c^2 of the nominal masses (1.8646, 1.8693, and 1.9685 GeV/c^2 for the D^0, D^+, and D_s^+, respectively). The $M_{\rm BC}$ variable is still used for first-stage selection, except that D_s^+ candidates must satisfy $M_{\rm BC} \geq 1.93$ GeV/c^2.

CHAPTER 5

ANALYSIS METHOD

In this chapter we describe the procedure that was used to extract D_s^+ branching fractions.

5.1 Choice of Operating Point

The total hadronic cross-section in the charm threshold region was well-known before CLEO-c, due to precise measurements from the Crystal Ball [25] and BES-II [26] experiments among others [19]. The total charm cross-section could be derived from the difference of the total hadronic and the extrapolated u, d, s quark cross-sections. What was *not* well-known was the cross-sections of exclusive open charm final states. Of particular importance to the CLEO-c program, the optimal energy for D_s^+ production was not known.

To address this issue, CESR performed an energy scan in 2005–6 between 3.97 and 4.26 GeV. The CLEO data taken in this region were used to identify regions of maximum D_s^+ production [27]; the measured cross-sections for various D production mechanisms are shown in Figure 5.1. There are two local maxima, one near 4.01 GeV for $D_s^+ D_s^-$ and the other near 4.17 GeV for $D_s^{*\pm} D_s^{\mp}$. The 4.17 GeV maximum has a D_s^+ cross-section roughly three times that of the 4.01 GeV maximum, and as most D_s^+ analyses were expected to be statistics-starved, 4.17 GeV was chosen at the running point. At this energy the total charm cross-section is ~ 9 nb; only about a tenth of the total charm production produces D_s^+ events, the rest largely resulting in $D^* D^*$ and $D^* D$.

5.2 Outline of the Tagging Method

As mentioned in Section 1.3, this analysis utilizes the pair production of D_s^+ mesons in $D_s^{*\pm}D_s^{\mp}$ events to determine the absolute scale of D_s^+ branching fractions. The method is described in more detail below.

In this analysis, D_s^{*+} mesons are assumed to decay in either of the two modes $D_s^{*+} \to \gamma D_s^+$ or $D_s^{*+} \to \pi^0 D_s^+$. These are the only two allowed strong or electromagnetic transitions; the $\pi^0 D_s^+$ decay is suppressed because it is isospin-violating. In particular any possible weak decays are ignored.

Consider a decay $D_s^+ \to i$, and another decay $D_s^- \to \bar{\jmath}$. If the branching fraction for the i and $\bar{\jmath}$ decays are $\mathcal{B}_i$ and $\mathcal{B}_j$ (= $\mathcal{B}_{\bar{\jmath}}$ if we assume CP violation is negligible), the efficiency for reconstructing just the i decay (single tag, ST) is ϵ_i, the efficiency for reconstructing both i and $\bar{\jmath}$ (double tag, DT) is $\epsilon_{i\bar{\jmath}}$, the yield of $D_s^+ \to i$ is N_i, and the yield of $D_s^+ \to i$, $D_s^- \to \bar{\jmath}$ is $N_{i\bar{\jmath}}$, then we have

$$N_i = \epsilon_i \mathcal{B}_i N_{\text{pairs}},$$

$$N_{i\bar{\jmath}} = \epsilon_{i\bar{\jmath}} \mathcal{B}_i \mathcal{B}_j N_{\text{pairs}}.$$

From this we can obtain

$$\mathcal{B}_j = \frac{N_{i\bar{\jmath}}}{N_i} \frac{\epsilon_i}{\epsilon_{i\bar{\jmath}}}.$$

If we additionally have $N_{\bar{\jmath}}$ and $\epsilon_{\bar{\jmath}}$ ($\epsilon_{\bar{\jmath}} \neq \epsilon_j$ in general because the detector is not C-symmetric), then

$$N_{D_s^* D_s} = \frac{N_i N_{\bar{\jmath}}}{N_{i\bar{\jmath}}} \frac{\epsilon_{i\bar{\jmath}}}{\epsilon_i \epsilon_{\bar{\jmath}}}.$$

In short, given yields and efficiencies for single and double tags, we can obtain the branching fractions and the total number of D_s^+ pairs produced. To increase the statistical power of the measurement we can utilize multiple decay modes. In practice, we express expected yields as a function of branching fraction and fit for them using the observed yields as input.

Figure 5.1: Cross-sections for three D_s^+ production mechanisms (top) and three D^0/D^+ mechanisms (bottom) in the range $E_{\rm cm}$ = 3.97–4.26 GeV [27]. The vertical lines indicate various thresholds. The light lines connecting the points serve to guide the eye.

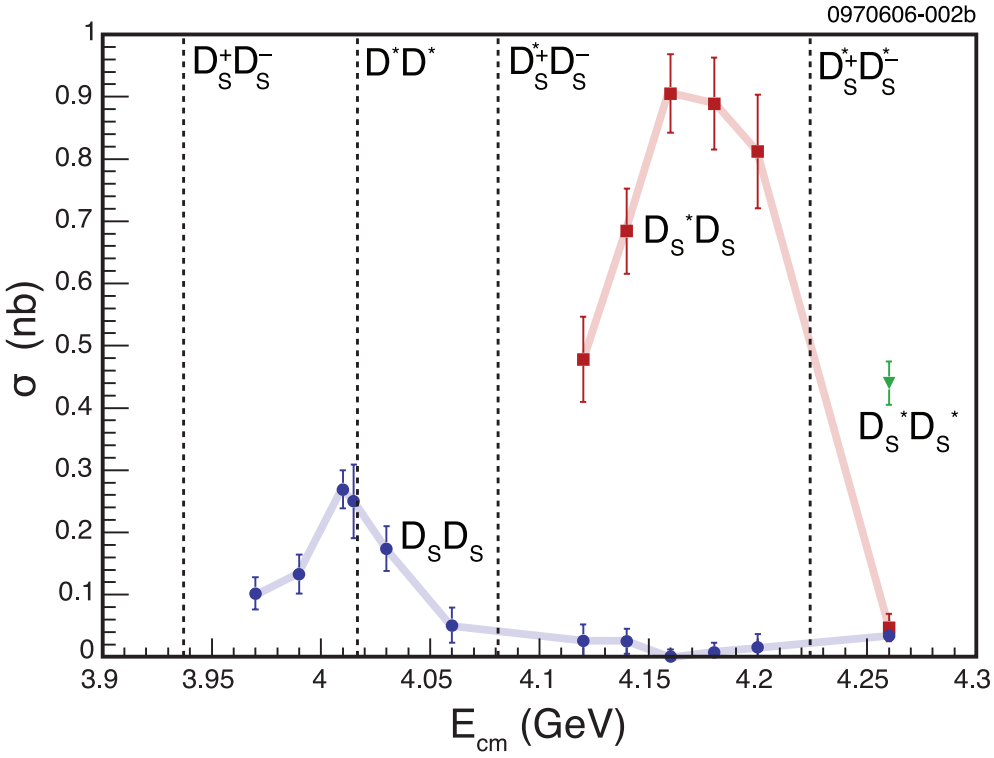
0970606-002b
$D_s^+D_s^-$
D^*D^*
$D_s^{*+}D_s^-$
$D_s^{*+}D_s^{*-}$
$D_s^*D_s$
$D_s^*D_s^*$
D_sD_s
σ (nb)
E_{cm} (GeV)

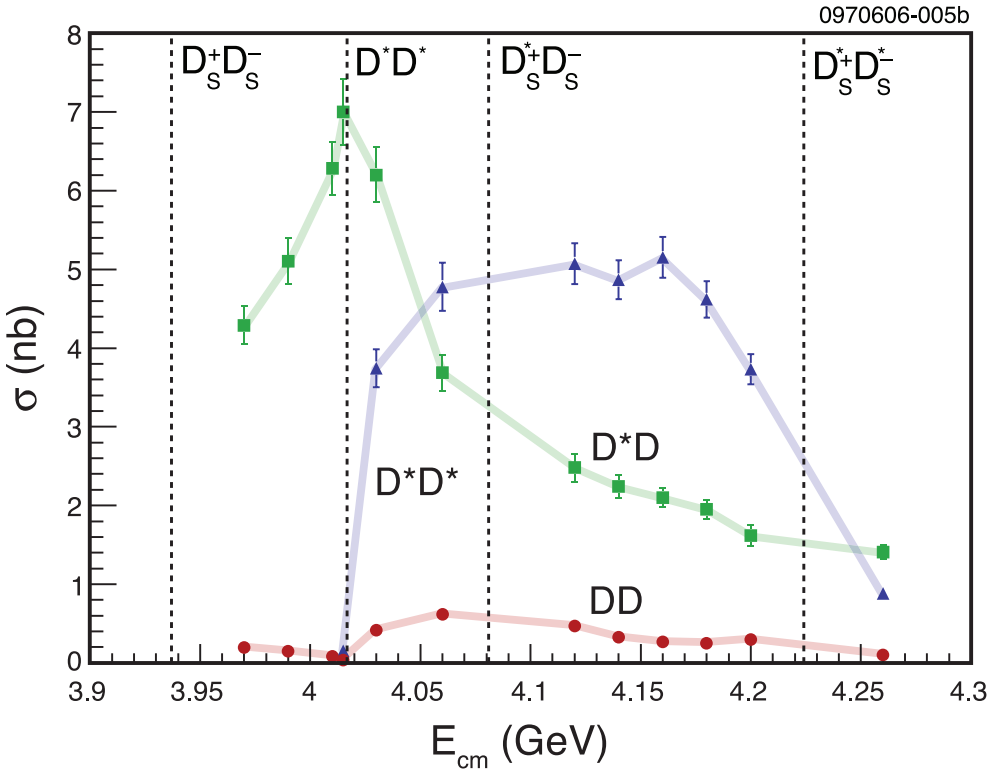
0970606-005b
$D_s^+D_s^-$
D^*D^*
$D_s^{*+}D_s^-$
$D_s^{*+}D_s^{*-}$
D*D
D*D*
DD
σ (nb)
E_{cm} (GeV)

The statistical power of this method is limited by the number of double tag events that are reconstructed, and in general the relative statistical uncertainty on the branching fractions will be dominated by $1/\sqrt{N(\text{total double tags})}$.

An additional feature of this method is that systematics that affect both single and double tag yields of a given mode will *only* affect the determined branching fraction for that mode — as can be seen in the formulas above, such systematics cancel in the ratio of efficiencies. For example, π^0 efficiency systematics will not propagate into the branching fraction for all-charged modes.

Once we have the number of D_s^+ events produced, we can compute the branching fraction for any given subdecay mode: we obtain $\mathcal{B}_X \equiv \mathcal{B}(D_s^+ \to X)$ by taking

$$\mathcal{B}_X = \frac{N_X}{N_{D_s^* D_s} \epsilon_X}.$$

The eight D_s^+ decay modes that were chosen are listed in Table 5.1. All chosen final states have large reconstructible branching fractions ($> 0.6\%$) and reasonable signal-to-background ratios.

5.3 Event and Detector Simulation

This analysis relies on knowing the true efficiencies for reconstructing various tag modes. Because of the many factors that affect the efficiency — mostly detector effects distinct from the underlying physics — analytical computation of the detection probabilities is not possible. Instead we use Monte Carlo simulations for both the e^+e^- interaction and prompt particle decay ("truth" or "generator" level) and the further interactions of the daughter particles with the detector systems. These are discussed below.

Table 5.1: Decay modes used in this analysis. Charge conjugate modes are implied.

$D_s^+ \to K_S^0 K^+$
$D_s^+ \to K^- K^+ \pi^+$
$D_s^+ \to K^- K^+ \pi^+ \pi^0$
$D_s^+ \to K_S^0 K^- \pi^+ \pi^+$
$D_s^+ \to \pi^+ \pi^+ \pi^-$
$D_s^+ \to \pi^+ \eta \; (\eta \to \gamma\gamma)$
$D_s^+ \to \pi^+ \eta' \; (\eta' \to \pi^+\pi^-\eta, \; \eta \to \gamma\gamma)$
$D_s^+ \to K^+ \pi^+ \pi^-$

5.3.1 Event Generators

To model the underlying physics process — the e^+e^- collision, the products of that interaction, and the subsequent prompt decays — we rely on a combination of CLEO-originated code and standard packages.

The CLEO code allows us to separate the accelerator-dependent aspects from the collision-level simulation. This code uses information reported by CESR to simulate the structure of the colliding beams at the bunch level, including the number of bunches in a train, the number of trains, and the relative current in each bunch. Information on the beam energies, energy spreads, and crossing angle at the detector is used to construct center of mass four-vector distributions which are sampled as input for the physics generators.

The primary event generator used in CLEO-c is EvtGen [28]. (Another generator, QQ [29], is used only for producing $e^+e^- \to \tau^+\tau^-$ samples.) The input to EvtGen consists of the initial state virtual photon four-momentum and a set

of tables detailing allowed particle decays. The decays are specified by the resulting daughter particles, the branching fraction, and the "model" that is used for the decay. If the resulting state still has unstable particles, those are decayed according to their respective decay tables, until only stable particles are left. ("Stable" in this context means photons, $\pi^{\pm}$, all kaons, $e^{\pm}$, $\mu^{\pm}$, and neutrinos.)

The different models used by EvtGen allow sophisticated simulation of the dynamics of various decays. When possible, decay chains are modeled with amplitudes for each step, not probabilities. This allows proper modeling of angular correlations simply by chaining together decay models (for example, specifying $D_s^+ \to \phi\pi^+$ as spin 0 $\to$ spin 1 + spin 0 and $\phi \to K^-K^+$ as spin 1 $\to$ spin 0 + spin 0 produces the correct final state angular distributions without additional intervention).

Several specific models are worth mentioning in detail. The models SVS and VSS simulate $0 \to 1 + 0$ and $1 \to 0 + 0$ processes, respectively. The PHSP model distributes the final state products uniformly in phase space; this is used both for $0 \to 0+0$ decays and for multibody decays with unknown angular distributions. There are a number of models, for example SVV_HELAMP, which simulate decays with multiple independent amplitudes depending on polarizations; in general, lacking better information, all the amplitudes are assumed to be equal with zero phase between them.

For high-energy open charm production, the first model encountered in the decay chain is VPHOTOVISRHI, which shapes the process $\gamma^* \to \gamma\psi(4160)$. This is not a physical process; it is instead a shorthand for the production of initial state radiation ("γ") and a $c\bar{c}$ spectral density that fragments to open charm ("$\psi(4160)$"). The initial state radiation distribution at an energy E is dependent on the the cross-section for open charm production at all energies $E' < E$. The

VPHOTOVISRHI model incorporates the cross-section information from [27], convolving it with a radiative kernel [30] keeping only lowest-order terms in the photon energy E_γ. The probability for emission of an ISR photon is given by

$$P(E_\gamma) \propto E_\gamma^{\beta-1}\sigma(E_{\rm cm} - E_\gamma),$$

where

$$\beta \equiv (2\alpha/\pi)(2\ln(E_{\rm cm}/m_e) - 1) \approx 0.08.$$

In our approximation the ISR photon is always emitted along $\pm z$. There is always an ISR photon in this model, although its energy is allowed to range all the way down to zero; an upper cutoff is imposed by the threshold for the open charm state being produced.

The cross-section $\sigma(E_{\rm cm} - E_\gamma)$ is that for production of the relevant process at energy $E_{\rm cm} - E_\gamma$ without initial state radiation. In principle radiative corrections should be applied to the observed production rates (which include ISR) to obtain this "Born-level" cross-section; in practice we use the observed rates from the scan without corrections. The effect on the spectrum shape (the relevant observable) is small, and a systematic uncertainty is assigned later for discrepancies between the model and reality.

Additional processes are studied to understand backgrounds. These were $e^+e^- \to \tau^+\tau^-$, $\gamma\psi(2S)$, and light quarks. The first was generated with the QQ generator; the latter two were produced with EvtGen models (VECTORISR and LUNDAREALAW respectively).

5.3.2 Decay Tables

A comprehensive decay table is maintained for each particle that EvtGen considers unstable. This table gives the branching fraction and model for each possible

decay channel. The specifications for each decay are motivated by physical principles and branching fraction measurements; for example, $0 \rightarrow 1 + 0$ processes are simulated with the SVS model, and the specified branching fractions in the tables used for this analysis were inspired by the 2005 PDG averages. Branching fractions for decays not yet measured must be estimated using inclusive measurements or other constraints. The table used for D_s^+ decays included 72 modes, including all the ones considered for this analysis.

No Dalitz models were implemented for any D_s^+ decay, so resonant substructure in all final states was created by incoherently adding different subchannels. When specific final states were generated, the contributing submodes were simulated in the same ratio that they would in the full "generic" decay table. The per-channel contributions for each D_s^+ final state in this analysis are listed in Table 5.2.

5.3.3 Detector Simulation

After simulating the e^+e^- interaction, we need to model the interactions of the resulting daughter particles with the detector, as well as the response of the active detector components. This is done with a GEANT 3.21 [31] simulation of CLEO, coupled with response-simulation routines. The GEANT model includes information on the geometry and material makeup of the detector components. As the "stable" particles resulting from the collision traverse the model, GEANT subjects them to a list of possible interaction processes at each propagation step, depending on the relevant cross-sections; these include various electromagnetic and hadronic interactions. It is also possible for particles to decay within the detector (e.g. $K^+ \rightarrow \mu^+\nu_\mu$). In particular neutral kaon decays are handled by

Table 5.2: Resonant mode contributions in Monte Carlo to 3- and 4-body final states studied in this analysis. Different modes are added incoherently in the MC.

Final State	Intermediate State	Fraction	Model
$K^-K^+\pi^+$	$\overline{K}^{*0}K^+$	42.6%	SVS
	$\phi\pi^+$	37.7%	SVS
	$\overline{K}_0^{*0}K^+$	8.5%	PHSP
	$K^-K^+\pi^+$	6.6%	PHSP
	$f_0(980)\pi^+$	4.5%	PHSP
	$f_2(1270)\pi^+$	0.1%	PHSP
$K^-K^+\pi^+\pi^0$	$\phi\rho^+$	52.2%	SVV_HELAMP
	$K^{*+}\overline{K}^{*0}$	20.4%	SVV_HELAMP
	$\phi\pi^+\pi^0$	17.9%	PHSP
	$K^+\overline{K}^{*0}\pi^0$	9.5%	PHSP
$K_S^0K^-\pi^+\pi^+$	$K^{*+}\overline{K}^{*0}$	60.2%	SVV_HELAMP
	$K_S^0K^-\pi^+\pi^+$	39.8%	PHSP
$\pi^+\pi^+\pi^-$	$f_0(980)\pi^+$	85.8%	PHSP
	$f_2(1270)\pi^+$	6.3%	PHSP
	$\rho(2S)^0\pi^+$	4.4%	PHSP
	$\rho^0\pi^+$	2.6%	SVS
	$\omega\pi^+$	0.5%	SVS
	$\pi^+\pi^+\pi^-$	0.3%	PHSP
$K^+\pi^+\pi^-$	ρ^0K^+	33.6%	SVS
	$K^{*+}\pi^+$	19.9%	SVS
	$K^*(1410)^0\pi^+$	16.3%	PHSP
	$K^+\pi^+\pi^-$	14.9%	PHSP
	$K^+\rho(2S)^0$	9.0%	PHSP
	$K_0^*(1430)^0\pi^+$	6.2%	PHSP

GEANT to allow for possible interactions and regeneration before the decay point.

The response simulation is done a detector-by-detector basis:

- The calorimeter simulation uses the GEANT simulation of electromagnetic cascades to determine the total energy deposited in a crystal. Parametrized noise is added to this response. There is an energy cutoff below which GEANT no longer simulates the particles of electromagnetic showers; therefore the reported energy and shower profile is not quite correct, and a response function must be used to map the GEANT-reported energy to what would actually be observed.
- The tracking simulation uses resolution and propagation parameters determined from data to produce tracking hits. Because of the time-based nature of drift chamber tracking, this simulation depends on the simulated CESR bunch timing structure.
- The energy loss signal (dE/dx) in the tracking system is simulated by throwing values according to resolutions measured in data for each experimental run. The loss as simulated by GEANT is not used because of the great sensitivity of the dE/dx gain to the atmospheric pressure; the measured sensitivities are updated with < 1 hour granularity.
- Individual Cherenkov photons are radiated and propagated through the RICH by custom code, using parametrizations of photon emission probability and the quantum efficiency of the conversion gas. The code also considers photons radiated in inelastic collisions in the expansion volume gas.

5.4 Dataset

We use 298 ± 3 pb^{-1} of data recorded at E_{cm} = 4.170 GeV. This was divided into three subsets, labeled datasets 39 through 41, of 55 pb^{-1}, 124 pb^{-1}, and 119 pb^{-1} respectively. The luminosity uncertainty is estimated at 1% [32].

5.5 Monte Carlo Samples

We use the following Monte Carlo samples to study different aspects of this analysis:

Signal MC These are samples that feature only one particular single tag or double tag mode. In the single tag case, the non-signal D_s decays generically; for double tag samples both decays are specified. Approximately 80,000 events are generated. A representative sample of 20 runs spread with equal luminosity increments through datasets 39, 40, and 41 was chosen.

Generic This consists of two large samples simulating datasets 39–41: a 20× sample and a 10× sample (≈ 6 and 3 fb^{-1}, respectively). These contain an appropriately-weighted mixture of all open charm production channels at 4.17 GeV.

Continuum This 5× sample corresponds to ≈ 1.5 fb^{-1} at 4.17 GeV generated with the Lund area law generator [33].

5.6 Sample Selection

In all the material that follows except for discussion of double tag reconstruction and *CP* asymmetries, charge conjugation symmetry should be assumed, so references to D_s^+ and D_s^{*+} mesons implicitly also apply to D_s^- and D_s^{*-} mesons. When

discussing double tags, charge correlations between the two tags are explicitly shown.

We decide not to perform a full reconstruction of the event, so we make no attempt to find a D_s^{*+}. We do this to avoid an efficiency loss, and to avoid systematics arising from soft photon detection which would affect single and double tags differently.

The following are notable features of D_s^+ kinematics:

- The initial $D_s^{*\pm}D_s^{\mp}$ pair is produced with momentum determined by $E_{\rm cm}$. The directly-produced $D_s^{\pm}$ thus has tightly constrained momentum. The $D_s^{\mp}$ produced as a daughter of the $D_s^{*\mp}$ acquires a small boost from this decay, and thus has a momentum spread around the value for the direct $D_s^{\pm}$. We use the recoil mass $M_{\rm rec}$,

$$M_{\rm rec}c^2 \equiv \sqrt{\left(E_{\rm cm} - \sqrt{\mathbf{p}_{D_s}^2 c^2 + m_{D_s}^2 c^4}\right)^2 - \left(\mathbf{p}_{\rm cm} - \mathbf{p}_{D_s}\right)^2 c^2}$$

  as a proxy for momentum. (The initial momentum $\mathbf{p}_{\rm cm}$ is not zero due to the crossing angle of the beams; it is known from the CESR beam configuration.) We cut on $M_{\rm rec}$ to select the charm production channel. A comparison of data and MC $M_{\rm rec}$ spectra is shown in Figure 5.2.

- We use the invariant mass of the $D_s^{\pm}$ candidates, $M_{\rm inv}$, as our primary analysis variable. It has very little correlation with $M_{\rm rec}$ in the region of interest; in particular $M_{\rm inv}$ peaks at a constant location regardless of the candidate momentum.

5.6.1 Candidates

We start with the full set of reconstructed D_s^+ candidates obtained via the procedure described in Chapter 4. For better data/MC agreement in dE/dx par-

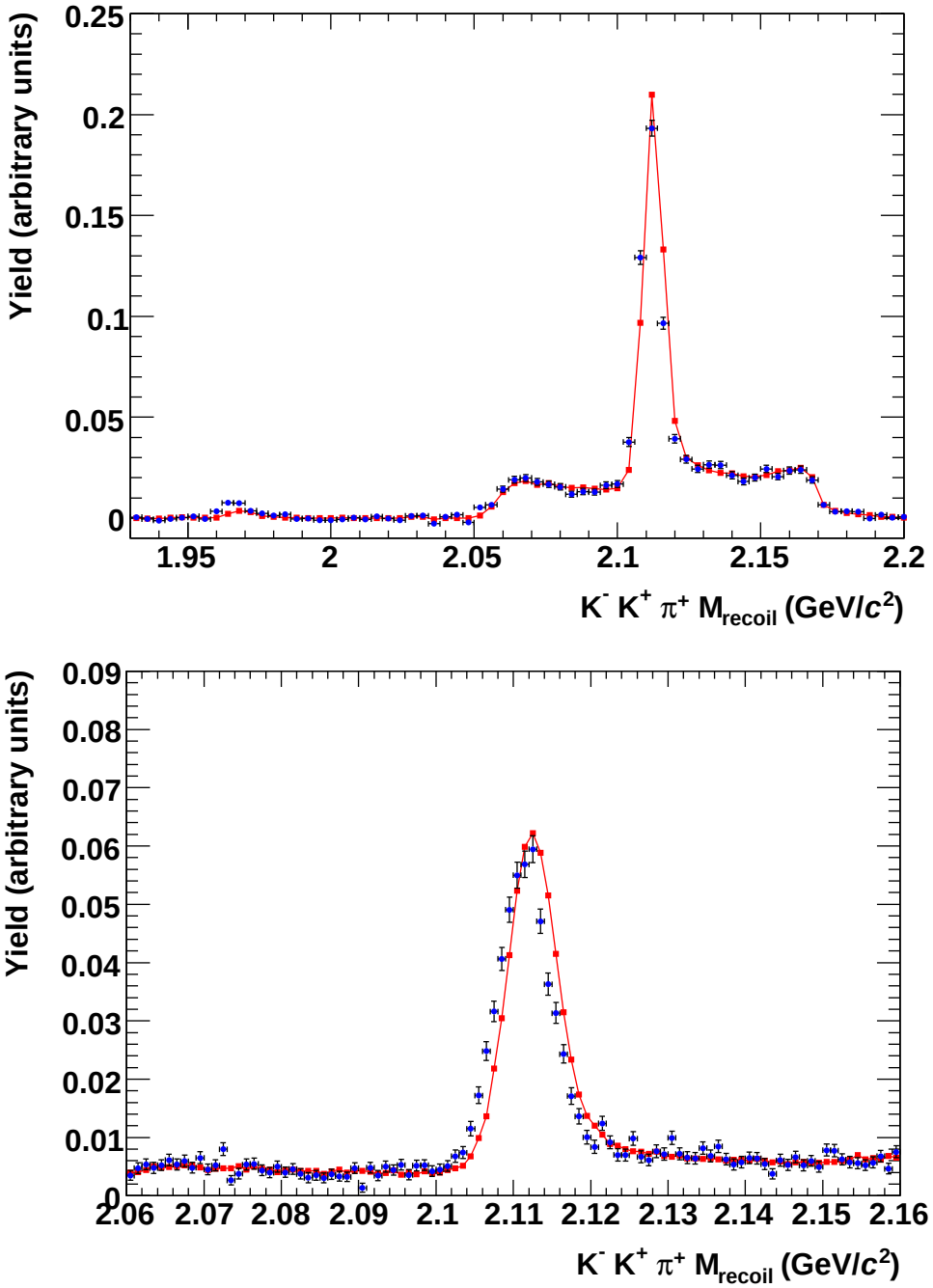

Figure 5.2: Comparison of recoil mass spectra for $D_s^+ \to K^-K^+\pi^+$ candidates in data (blue points) and generic Monte Carlo (red line). The plot on the bottom shows detail in the $D_s^{*\pm}D_s^{\mp}$ region, including a small discrepancy in peak positions.

ticle identification, we raise the minimum kaon momentum requirement to 0.125 GeV/c. To reduce K^0_S combinatoric backgrounds, we require a 3σ cut of $|M(K^0_S) - 497.7\ \mathrm{MeV}/c^2| < 6.3\ \mathrm{MeV}/c^2$ for all candidates.

The inclusive window for D_s^+ candidates in the standard skim is $M_{\mathrm{BC}} > 1.93$ GeV/c^2, $|M_{\mathrm{inv}} - 1.9685\ \mathrm{GeV}/c^2| < 0.085$ GeV/c^2. For this analysis we tighten the requirements, and instead of using M_{BC} we cut in M_{rec}. Because both M_{BC} and M_{rec} are monotonic functions of $\mathbf{p}_{D_s}$, no events are lost by applying the M_{BC} preselection. We use two different kinds of M_{rec} cut: a "loose" cut, set to be $M_{\mathrm{rec}} > 2.051$ GeV/c^2 for all modes, and a "tight" cut, applied only to $D_s^+ \to K^-K^+\pi^+\pi^0$, $D_s^+ \to \pi^+\pi^+\pi^-$, and $D_s^+ \to K^+\pi^+\pi^-$ single tag candidates, requiring $M_{\mathrm{rec}} >$ (2.099 GeV/c^2, 2.101 GeV/c^2, 2.099 GeV/c^2) respectively. The loose cut includes the entire range of M_{rec} of the boosted daughter of the D_s^*, and so allows the maximal efficiency. The tight cut selects the directly-produced D_s^+ and over half of the indirect D_s^+ as well, and reduces the background while reducing the impact of initial-state radiation smearing on the efficiency.

Later we refer to "ϕ" and "$\overline{K}^{*0}$" selections. For the ϕ, we require a pair of kaons with $1.0095\ \mathrm{GeV}/c^2 < m(K^-K^+) < 1.0295\ \mathrm{GeV}/c^2$; for the $\overline{K}^{*0}$ we require a K^- and a π^+ (or conjugate) with $0.85\ \mathrm{GeV}/c^2 < m(K^-\pi^+) < 0.94\ \mathrm{GeV}/c^2$.

We also apply mode-dependent selection criteria on the D_s^+ daughters as follows:

- $D_s^+ \to K^0_S K^+$:
  - Veto if $M(K^+\pi^-) > 1.83\ \mathrm{GeV}/c^2$
- $D_s^+ \to K^-K^+\pi^+$:
  - Veto if $1.845\ \mathrm{GeV}/c^2 < M(K^-K^+) < 1.88\ \mathrm{GeV}/c^2$
- $D_s^+ \to K^-K^+\pi^+\pi^0$:

- $|\mathbf{p}_{\pi^0}| > 100$ MeV/c
- $|\mathbf{p}_{\pi^+}| > 100$ MeV/c
- Veto if 1.86 GeV/c^2 < $M(K^-K^+\pi^+)$ < 1.88 GeV/c^2

- $D_s^+ \to K_S^0 K^-\pi^+\pi^+$:
  - Momentum of all pion tracks (including K_S^0 daughters) > 100 MeV/c
  - Veto if 1.855 GeV/c^2 < $M(K^-\pi^+\pi^+\pi^-_{K_S^0})$ < 1.875 GeV/c^2

- $D_s^+ \to \pi^+\pi^+\pi^-$:
  - Momentum of all pion tracks > 100 MeV/c
  - Veto if either $\pi^+\pi^-$ combination satisfies 475 MeV/c^2 < $M(\pi^+\pi^-)$ < 520 MeV/c^2
  - Veto if either $\pi^+\pi^-$ combination satisfies 1.84 GeV/c^2 < $M(\pi^+\pi^-)$ < 1.885 GeV/c^2
  - Consider the π^- as a K^-. Then veto if either $K^-\pi^+$ combination has 1.845 GeV/c^2 < $M(K^-\pi^+)$ < 1.88 GeV/c^2

- $D_s^+ \to K^+\pi^+\pi^-$:
  - Momentum of all pion tracks > 100 MeV/c
  - Veto if 475 MeV/c^2 < $M(\pi^+\pi^-)$ < 520 MeV/c^2
  - Veto if $M(K^+\pi^-)$ > 1.83 GeV/c^2

The purpose of these selections is to remove feedthrough from K_S^0 decays to $\pi^+\pi^-$ (the $M(\pi^+\pi^-)$ vetoes) and to reduce reflections from D^0 and D^+ decays where those are combined with a soft pion from a D^* decay to fake a D_s^+ decay mode. For example, the decay chain $D^{*+} \to D^0\pi^+ \to K^-K^+\pi^+$ creates a $K^-K^+\pi^+$ candidate

at the D^{*+} mass; we can eliminate this through the $M(K^-K^+)$ veto on $K^-K^+\pi^+$ candidates. The mass vetoes remove specific D^0/D^+ decays that cause problems, while the pion momentum requirements suppress the soft pion background combinatorics. Although these backgrounds peak at the wrong location in $M_{\rm inv}$, they make it harder to understand the dominant smooth background contribution, so the suppression is useful.

Single Tags

We require our single tag candidates to pass the appropriate $M_{\rm rec}$ cut as listed above. We search for a "best" single tag candidate for each mode, separately for each charge, in every event. The chosen candidate is the one with the smallest value of $|M_{\rm rec} - 2.112\ {\rm GeV}/c^2|$.

Double Tags

In a double tag $D_s^{*\pm}D_s^{\mp}$ event, one of the $D_s^{\mp}$ will be direct, and one will be boosted from the $D_s^{*\pm}$ decay. We impose the loose $M_{\rm rec}$ requirement on both the $D_s^{\pm}$ candidates as we do not know a priori which one is which.

The $D_s^{\pm}$ candidates in double tags are required to pass the same vetoes as those in single tags; this improves cancellation of efficiency systematics.

To resolve multiple candidates, we select the $D_s^+D_s^-$ combination with total mass closest to $2 \times 1.9682\ {\rm GeV}/c^2$. This variable is orthogonal to the signal/sideband selection variable (the mass difference between the two tags), discussed further below.

5.7 Yield Fits and Efficiencies

5.7.1 Single Tags

The nominal fit for single tag events is to a linear background (for most modes) or a quadratic background (for $K^-K^+\pi^+\pi^0$ and $\pi^+\pi^+\pi^-$) and a signal lineshape. For the $K^-K^+\pi^+\pi^0$, $\pi^+\pi^+\pi^-$, and $\pi^+\eta$ modes, the signal lineshapes are parametrized as the sum of a narrow Gaussian and a wider Crystal Ball function [34]. For the other five modes, the lineshape is the sum of two Gaussians. The lineshape parameters are fixed separately for each charge from signal MC, where the reconstructed D_s is matched to the generator-level particle.

Fits to the signal Monte Carlo samples are shown in Figures A.9–A.16, to the generic Monte Carlo samples in Figures A.17–A.24, and to data in Figures A.25–A.32. The blue line is the total fit shape, the green line is the wider of the two Gaussians, and the red line is the background. The efficiencies derived from these fits are shown in Table 5.3.

5.7.2 Double Tags

Double tag yields are found using a cut-and-count method, due to the low event yield in most modes. Combinatoric background from D^0/D^+ and continuum events is structured along diagonals from top left to bottom right, i.e. lines of constant total mass (an example mode is shown in Figure 5.3). We therefore take signal and sideband regions running diagonally in this direction. The signal and sideband regions are specified in Table 5.4.

Plots showing the signal and sideband regions in signal Monte Carlo are shown in Figures A.34–A.41; the resulting double tag selection efficiencies are shown in Table 5.5. In the Monte Carlo double tag plots, the red points are

Table 5.3: Single tag efficiencies from signal MC. No systematic corrections have been applied.

Mode	D_s^+ eff (%)	D_s^- eff (%)
$K_S^0K^+$	38.15 ± 0.18	37.52 ± 0.18
$K^-K^+\pi^+$	44.21 ± 0.18	44.44 ± 0.18
$K^-K^+\pi^+\pi^0$	12.35 ± 0.13	12.17 ± 0.14
$K_S^0K^-\pi^+\pi^+$	21.41 ± 0.15	21.42 ± 0.15
$\pi^+\pi^+\pi^-$	50.81 ± 0.18	50.99 ± 0.18
$\pi^+\eta$	20.17 ± 0.15	19.66 ± 0.16
$\pi^+\eta'$	5.57 ± 0.09	5.29 ± 0.08
$K^+\pi^+\pi^-$	43.50 ± 0.18	42.77 ± 0.18

events tagged as double misreconstruction, where neither side tag matches to a real $D_s^\pm$; the blue points are events tagged as single misreconstruction, were one side is good; and the black are correct reconstructions of both sides. Inspection of the single-misreconstructed events by hand shows that the bulk are actually failures of the MC truth tagger in events with final state radiation and decays in flight, and so the peaking in the signal region which can be observed in the blue events is due to actual signal events. The analogous plots for generic Monte Carlo and data are Figures A.42–A.49 and A.50–A.57, respectively. In the D^0/D^+ generic and continuum samples, we see no evidence of the background peaking in the signal region.

We also compute the (small) probabilities for crossfeed between different signal modes. In many cases there are no observed crossfeed events in either the signal or sideband regions; in the vast majority of cases the effective efficiency

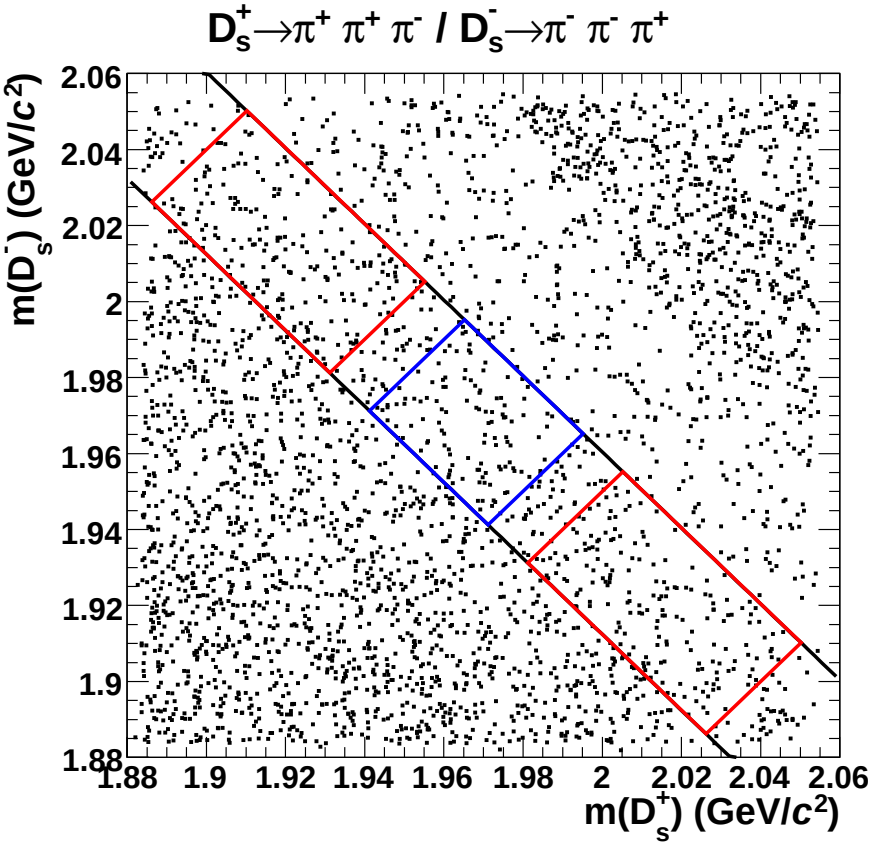

Figure 5.3: Double tags in continuum MC for mode $D_s^+ \to \pi^+\pi^+\pi^-/D_s^- \to \pi^-\pi^-\pi^+$.

is less than 10^{-4}. The largest crossfeeds, $\sim$ 0.1–0.3%, are associated with $K^+\pi^-\pi^+$ faking $K_S^0 K^+$. We have included all these in the branching fraction fit, allowing the crossfeed efficiency to be negative when the signal yield fluctuates below the scaled sideband yield.

5.8 Yields

Yields from the data fits are shown in Tables 5.6 (single tags) and 5.7 (double tags).

Table 5.4: Cuts for signal and sideband regions for double tag yields

Signal	$\lvert m(D_s^+) + m(D_s^-) - 2 \times 1.9682\ \mathrm{GeV}/c^2 \rvert < 0.024\ \mathrm{GeV}/c^2$
	$\lvert m(D_s^+) - m(D_s^-) \rvert < 30\ \mathrm{MeV}/c^2$
Sideband	$\lvert m(D_s^+) + m(D_s^-) - 2 \times 1.9682\ \mathrm{GeV}/c^2 \rvert < 0.024\ \mathrm{GeV}/c^2$
	$50\ \mathrm{MeV} < \lvert m(D_s^+) - m(D_s^-) \rvert < 140\ \mathrm{MeV}/c^2$

5.9 Branching Fraction Fit

We use a maximum-likelihood fit to obtain the branching fractions and number of $D_s^{*\pm}D_s^{\mp}$ pairs produced given the observed yields. The likelihood function $\mathcal{L}$ is the product of the likelihoods for obtaining the yield for each mode in terms of given branching fractions and $N_{D_s^*D_s}$; the overall $-2\ln\mathcal{L}$ is minimized with MINUIT. We use (Pearson) Gaussian statistics for single tag yields and Poisson statistics for double tag yields.

For Gaussian statistics, given a predicted event yield vector $E_i = N_{D_s^*D_s}\mathcal{B}_i\epsilon_i$ and observed yield vector $N_i \pm \sigma_i$, the likelihood is given by

$$\mathcal{L}_{\mathrm{gauss}}(N;E) = \frac{1}{\sqrt{2\pi|\det \mathbf{V}|}} \exp[-(N-E)\mathbf{V}^{-1}(N-E)^T/2],$$

$$\ln\mathcal{L}_{\mathrm{gauss}}(N;E) = -\frac{1}{2}\ln|\det\mathbf{V}| - \frac{1}{2}(N-E)\mathbf{V}^{-1}(N-E)^T + C.$$

where $\mathbf{V}$ is the covariance matrix of the expected yields. Considering only statistical errors, the matrix $\mathbf{V}$ is diagonal, and comprises the statistical uncertainty from fluctuations in E_i (variance E_i), the statistical uncertainty from background (variance fixed as $\sigma_i^2 - N_i$), and the efficiency uncertainties due to Monte Carlo statistics (variance $(\mathcal{B}_i\sigma_{\epsilon_i})^2$).

For Poisson statistics, given an observed signal box yield N, observed sideband yield B, expected signal mean E_N, expected sideband mean E_B, and a

Table 5.5: Double tag efficiencies from signal MC in percent. No systematic corrections have been applied.

	$K^0_S K^-$	$K^+K^-\pi^-$	$K^+K^-\pi^-\pi^0$	$K^0_S K^+\pi^-\pi^-$
$K^0_S K^+$	14.03 ± 0.13	17.14 ± 0.13	6.88 ± 0.09	8.36 ± 0.10
$K^-K^+\pi^+$	16.94 ± 0.13	19.92 ± 0.14	7.85 ± 0.10	9.82 ± 0.11
$K^-K^+\pi^+\pi^0$	6.76 ± 0.09	7.93 ± 0.10	2.36 ± 0.05	3.83 ± 0.07
$K^0_S K^-\pi^+\pi^+$	8.02 ± 0.10	9.79 ± 0.11	3.78 ± 0.07	4.47 ± 0.07
$\pi^+\pi^+\pi^-$	23.09 ± 0.15	28.13 ± 0.16	11.38 ± 0.11	13.78 ± 0.12
$\pi^+\eta$	6.86 ± 0.09	8.48 ± 0.10	3.24 ± 0.06	4.07 ± 0.07
$\pi^+\eta'$	2.10 ± 0.05	2.48 ± 0.06	0.97 ± 0.03	1.13 ± 0.04
$K^+\pi^+\pi^-$	19.85 ± 0.14	23.94 ± 0.15	9.60 ± 0.11	11.33 ± 0.11
	$\pi^-\pi^-\pi^+$	$\pi^-\eta$	$\pi^-\eta'$	$K^-\pi^-\pi^+$
$K^0_S K^+$	23.48 ± 0.15	6.96 ± 0.09	2.03 ± 0.05	20.28 ± 0.14
$K^-K^+\pi^+$	28.27 ± 0.16	8.40 ± 0.10	2.55 ± 0.06	23.59 ± 0.15
$K^-K^+\pi^+\pi^0$	11.46 ± 0.11	3.31 ± 0.06	0.95 ± 0.04	9.31 ± 0.10
$K^0_S K^-\pi^+\pi^+$	13.45 ± 0.12	3.94 ± 0.07	1.07 ± 0.04	11.40 ± 0.11
$\pi^+\pi^+\pi^-$	37.77 ± 0.18	11.61 ± 0.11	3.36 ± 0.06	32.27 ± 0.17
$\pi^+\eta$	11.42 ± 0.11	3.34 ± 0.06	0.97 ± 0.03	9.90 ± 0.11
$\pi^+\eta'$	3.43 ± 0.06	1.00 ± 0.04	0.31 ± 0.02	2.87 ± 0.06
$K^+\pi^+\pi^-$	32.69 ± 0.17	9.88 ± 0.11	2.84 ± 0.06	27.83 ± 0.16

Table 5.6: Single tag yields in data.

	D_s^+	D_s^-
$K_S^0 K^+$	1721.2 ± 50.2	1534.2 ± 47.9
$K^- K^+ \pi^+$	6974.1 ± 112.0	6973.5 ± 112.3
$K^- K^+ \pi^+ \pi^0$	1816.9 ± 114.2	2017.0 ± 115.3
$K_S^0 K^- \pi^+ \pi^+$	996.1 ± 51.3	1010.7 ± 50.7
$\pi^+ \pi^+ \pi^-$	1683.2 ± 107.9	1622.1 ± 107.1
$\pi^+ \eta$	813.8 ± 63.4	935.2 ± 64.4
$\pi^+ \eta'$	533.3 ± 28.7	564.6 ± 29.1
$K^+ \pi^+ \pi^-$	955.6 ± 84.5	750.5 ± 82.9

scaling factor α between sideband and signal regions, we have

$$\mathcal{L}'_{\text{poiss}}(N, B; E_N, E_B) = \left(\frac{1}{N!}\frac{(E_N + \alpha E_B)^N}{\exp(E_N + \alpha E_B)}\right)\left(\frac{1}{B!}\frac{(E_B)^B}{\exp(E_B)}\right).$$

For fixed N, B, and E_N, we can eliminate the parameter E_B by solving $\frac{\partial \ln \mathcal{L}'_{\text{poiss}}}{\partial E_B} = 0$ analytically (the resulting equation is quadratic in E_B). This value can then be plugged back into the likelihood, so

$$\mathcal{L}_{\text{poiss}}(N, B; E_N) = \mathcal{L}'_{\text{poiss}}(N, B; E_N, E_B)\Big|_{\partial \mathcal{L}'_{\text{poiss}}/\partial E_B = 0},$$

$$\ln \mathcal{L}_{\text{poiss}}(N, B; E_N) = (N \ln(E_N + \alpha E_B) - (E_N + \alpha E_B) + B \ln(E_B) - E_B + C)_{\partial \mathcal{L}'_{\text{poiss}}/\partial E_B = 0}.$$

This procedure has advantages over a straightforward background subtraction; in particular it gives sensible answers when the sideband-subtracted yield would be negative.

The fitter has been extensively tested in both the low-statistics and high-statistics regimes. It produces results very close to those of the standard fitter

Table 5.7: Double tag signal (scaled sideband) yields in data. The sideband yields shown here have been scaled by 1/3.

	$K^0_S K^-$	$K^+K^-\pi^-$	$K^+K^-\pi^-\pi^0$	$K^0_S K^+\pi^-\pi^-$
$K^0_S K^+$	12 (0.3)	44 (0.0)	26 (0.3)	7 (0.0)
$K^-K^+\pi^+$	33 (0.3)	173 (2.7)	67 (3.3)	25 (0.3)
$K^-K^+\pi^+\pi^0$	17 (0.0)	68 (4.7)	32 (8.7)	11 (1.0)
$K^0_S K^-\pi^+\pi^+$	3 (0.0)	29 (1.0)	12 (1.0)	3 (0.3)
$\pi^+\pi^+\pi^-$	5 (0.7)	47 (6.0)	31 (12.0)	10 (1.3)
$\pi^+\eta$	1 (0.0)	18 (0.0)	5 (1.3)	1 (0.0)
$\pi^+\eta'$	3 (0.0)	15 (0.0)	3 (0.0)	2 (0.0)
$K^+\pi^+\pi^-$	9 (0.7)	18 (1.3)	11 (4.0)	6 (0.3)
	$\pi^-\pi^-\pi^+$	$\pi^-\eta$	$\pi^-\eta'$	$K^-\pi^-\pi^+$
$K^0_S K^+$	16 (0.7)	5 (0.0)	6 (0.0)	10 (0.3)
$K^-K^+\pi^+$	56 (6.0)	25 (0.0)	11 (0.0)	20 (1.0)
$K^-K^+\pi^+\pi^0$	32 (9.3)	5 (0.0)	6 (0.3)	15 (1.3)
$K^0_S K^-\pi^+\pi^+$	8 (2.0)	3 (0.0)	2 (0.0)	5 (0.3)
$\pi^+\pi^+\pi^-$	33 (17.7)	7 (2.3)	4 (0.0)	10 (2.3)
$\pi^+\eta$	9 (2.0)	3 (0.0)	2 (0.3)	7 (0.0)
$\pi^+\eta'$	6 (0.3)	1 (0.0)	0 (0.0)	3 (0.0)
$K^+\pi^+\pi^-$	9 (2.0)	4 (0.3)	1 (0.0)	18 (12.7)

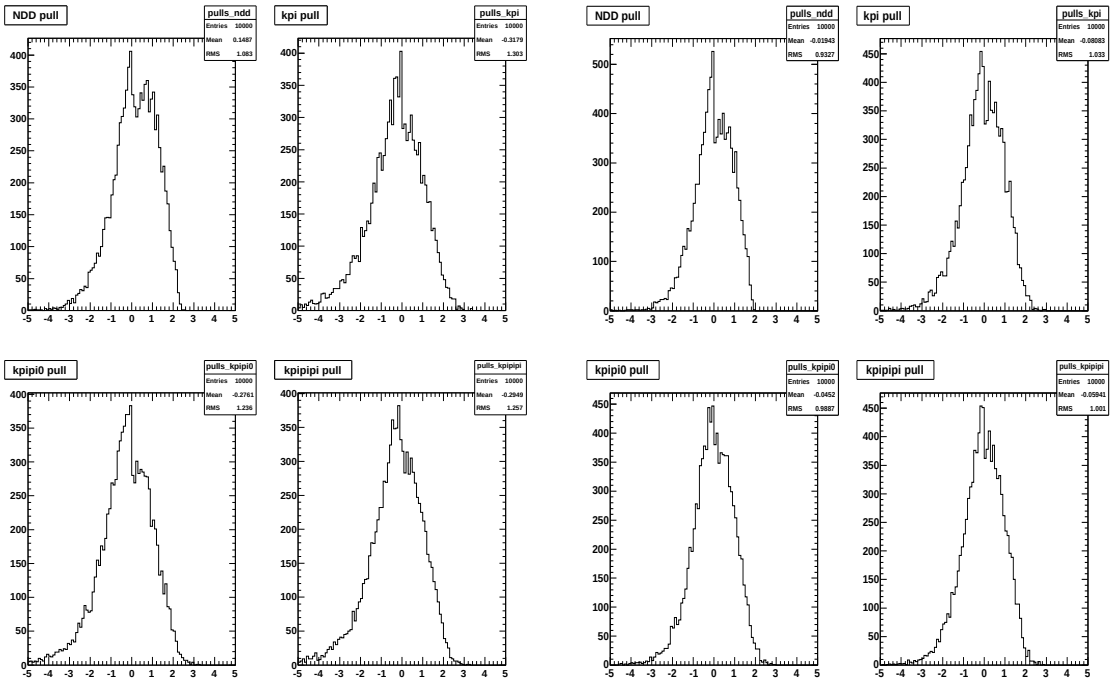

Figure 5.4: Pull distribution in low-statistics toy MC, using asymmetric errors, for Gaussian-only PDFs (left) and Gaussian/Poisson PDFs (right). The Gaussian-only distributions show biases and pull root-mean-square (RMS) values significantly different from 1. The Gaussian/Poisson distributions show less bias and RMS values consistent with 1.

on the D^0/D^+ data, and for toy low-statistics Monte Carlo shows less bias and better uncertainty estimation than a χ^2-fitter. Results of fits to toy Monte Carlo of $D^0\overline{D}^0$ production, with only 1000 pairs produced, are shown in Figures 5.4 and 5.5.

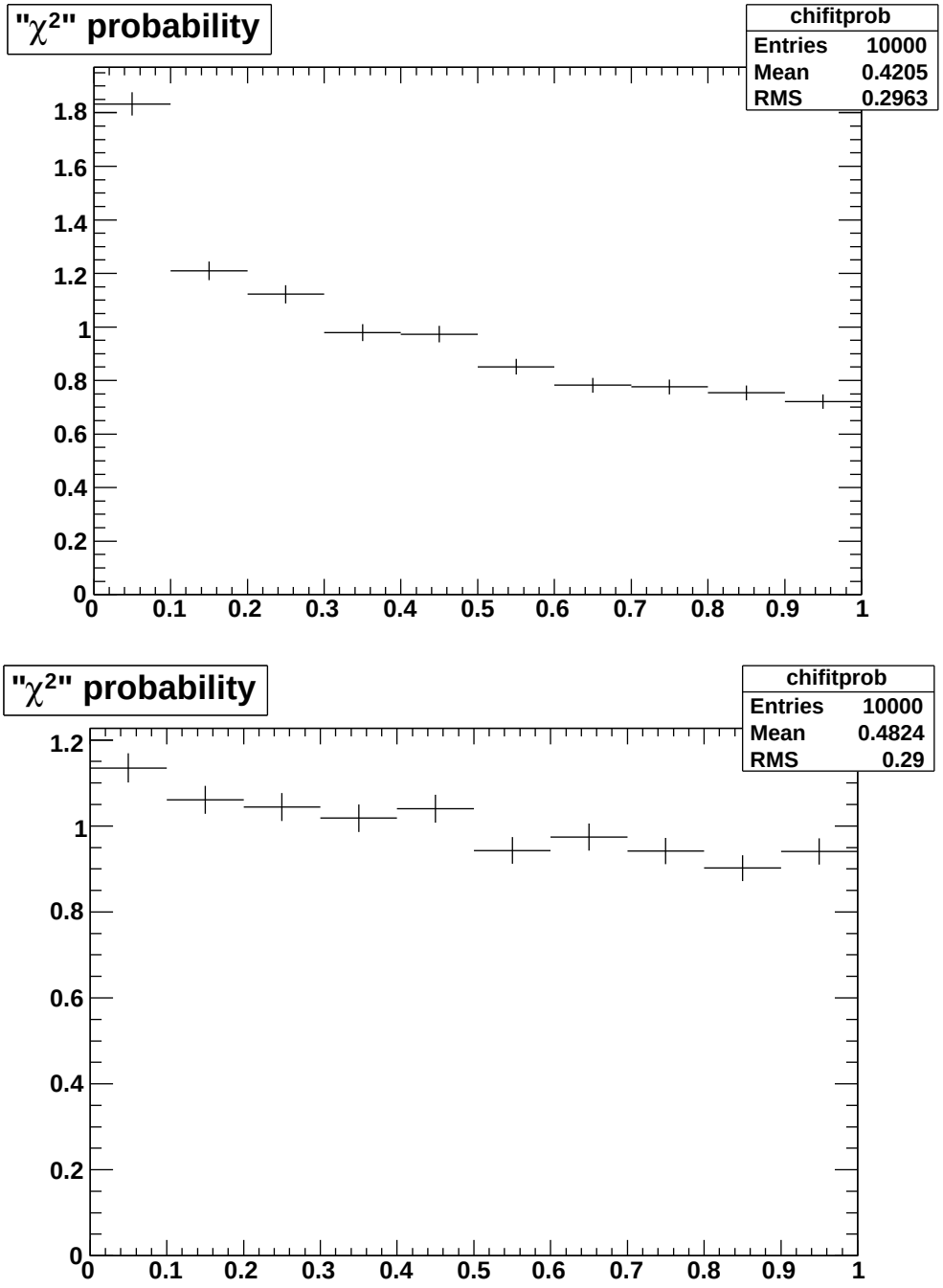

Figure 5.5: Fit probability for low-statistics toy MC, for Gaussian-only PDFs (left) and Gaussian/Poisson PDFs (right). The Gaussian-only plot shows much larger departures from flatness and indicates that the Gaussian-only fits badly model the likelihood landscape near the true value. The Gaussian/Poisson plot shows a much flatter distribution.

5.10 $K^-K^+\pi^+$ Partial Branching Fractions

Figure 5.6 shows the results of fitting for the $K^-K^+\pi^+$ yield in 2.5 MeV/c^2 bins of K^-K^+ invariant mass. A clear $\phi \to K^-K^+$ peak is seen sitting on a broad source of events reaching down to threshold. The kaon helicity angle distribution indicates this structure is predominantly scalar, and so we shall identify it as the $f_0(980)$ since this is seen strongly in $D_s^+ \to \pi^+\pi^+\pi^-$ and no strong $a_0(980)$ signal is observed in $D_s^+ \to \pi^+\pi^0\eta$.

The branching fraction $\mathcal{B}(D_s^+ \to \phi\pi^+)$ is desired for two reasons. One is to provide a precisely-measured, clean normalizing channel for future measurements. The other is to update previous branching ratio measurements that were normalized to this mode.

For future measurements, we believe that the appropriate procedure for normalization will be either to use the inclusive $K^-K^+\pi^+$ decay and our inclusive branching fraction for that mode, or to use experiment-defined cuts in combination with our inclusive measurement and the results of a high-statistics Dalitz analysis (one such study is in progress at BaBar). We will, however, make available partial branching fractions for K^-K^+ masses near the ϕ mass, trying to remain agnostic as to the production mechanism (for example, the $\phi \to K^-K^+$ branching fraction will not be corrected for).

Previous measurements that have used $D_s^+ \to \phi\pi^+$ as a normalizing mode have defined the ϕ signal region using a K^-K^+ mass cut and occasionally a helicity angle requirement. The requirements have been different for each experiment, making comparison difficult. Perusal of the PDG [19] indicates that (considering the recent BaBar $\mathcal{B}(D_s^+ \to \phi\pi^+)$ measurements) all branching ratios to $\phi\pi$ now have uncertainties larger than that of the $\phi\pi^+$ measurement, making reducing

the uncertainty on this ill-defined value less pressing. CLEO-c can contribute to these measurements by remeasuring the modes in question.

We obtain the partial branching fractions for four choices of mass window: 5, 10, 15, and 20 MeV/c^2 on either side of the ϕ mass, taken to be 1019.5 MeV/c^2. We obtain yields in data for these cuts (fitting the $M_{\rm inv}$ spectrum as normal). The efficiencies come from $D_s^+ \to \phi\pi^+$ and $D_s^+ \to f_0\pi^+$ signal Monte Carlo where the K^-K^+ invariant mass at generator level is restricted to the window being measured. For $\phi\pi^+$ events, the reconstructed K^-K^+ mass must also be within that window, to model the effect of resolution. The difference between this efficiency and the efficiency when the reconstructed mass is given an extra 2 MeV/c^2 on both sides is used as the systematic due to resolution. For $f_0\pi^+$ events, since the mass distribution is relatively flat, we assume that as many events will leak in to the window as leak out, and so use the extra 2 MeV/c^2 for the nominal efficiency with no uncertainty. The ratio $\epsilon(f_0\pi^+)/\epsilon(\phi\pi^+) \sim 1.05$ in general. The $\phi\pi^+$ and $f_0\pi^+$ efficiencies are combined using the scalar fractions obtained in Ref. [35]. The efficiency-corrected yields (summed over both charges) are then divided by twice the branching fraction fitter's result for the number of $D_s^{*\pm}D_s^{\mp}$ events produced to obtain the final branching fractions.

For completeness the procedure used in [35] to extract the scalar fractions f_s shown in Table 5.8 will be outlined here. The set of $D_s^+ \to K^-K^+\pi^+$ events were separated into bins 3 MeV/c^2 wide in K^-K^+ invariant mass. The $M_{\rm inv}$ spectrum in each bin is fit with the same functions that are used for the inclusive $K^-K^+\pi^+$ ST fits; this gives a D_s^+ yield in each bin. The resulting yields as a function of K^+K^- invariant mass are then fit to the incoherent sum of a ϕ lineshape and a linear polynomial for the scalar events. The ϕ lineshape is a non-relativistic Breit-Wigner shape convolved with a single Gaussian resolution function. The Breit-

Table 5.8: Scalar fraction f_s from Ref. [35], efficiencies and data yields for various cuts in K^-K^+ invariant mass around $m_\phi \equiv 1.0195\,\mathrm{GeV}/c^2$. Efficiencies include PID correction factor from Table 6.2. Efficiency uncertainties include all systematics.

Window	f_s (%)	$\epsilon(D_s^+)$ (%)	$\epsilon(D_s^-)$ (%)	D_s^+ Yield	D_s^- Yield
5 MeV/c^2	3.63 ± 0.20	41.5 ± 1.7	41.1 ± 1.8	2047 ± 47 ± 12	2054 ± 47 ± 11
10 MeV/c^2	5.98 ± 0.33	43.0 ± 0.9	42.7 ± 0.8	2502 ± 53 ± 11	2492 ± 53 ± 10
15 MeV/c^2	8.32 ± 0.44	43.2 ± 0.8	42.9 ± 0.8	2702 ± 55 ± 13	2698 ± 55 ± 11
20 MeV/c^2	10.55 ± 0.55	43.3 ± 0.8	43.0 ± 0.8	2846 ± 57 ± 16	2807 ± 56 ± 15

Wigner function includes a mass-dependent width for the ϕ which accounts for the p-wave decay (both in phase-space factors and Blatt-Weisskopf penetration factors). The ϕ interaction radius used for the Blatt-Weisskopf form factor was set to 4 GeV^{-1}.

The best-fit lineshape is shown in Figure 5.6. Significant caution should be taken in interpreting the results; in particular no efficiency corrections are applied, the scalar component is treated as a linear polynomial, and interference between the ϕ and scalar is not accounted for. Nevertheless we can establish the scalar fraction as $\lesssim 11\%$ for all the mass windows we use, and therefore the perturbation of the overall efficiency from that for the ϕ component only is small and contributes minimally to the systematic uncertainty.

The applicable systematic uncertainties are those due to tracking, particle ID, and final state radiation, and the yield uncertainties. The methods for determining these are detailed in the next section.

The results for the partial branching fractions are given in Table 7.3.

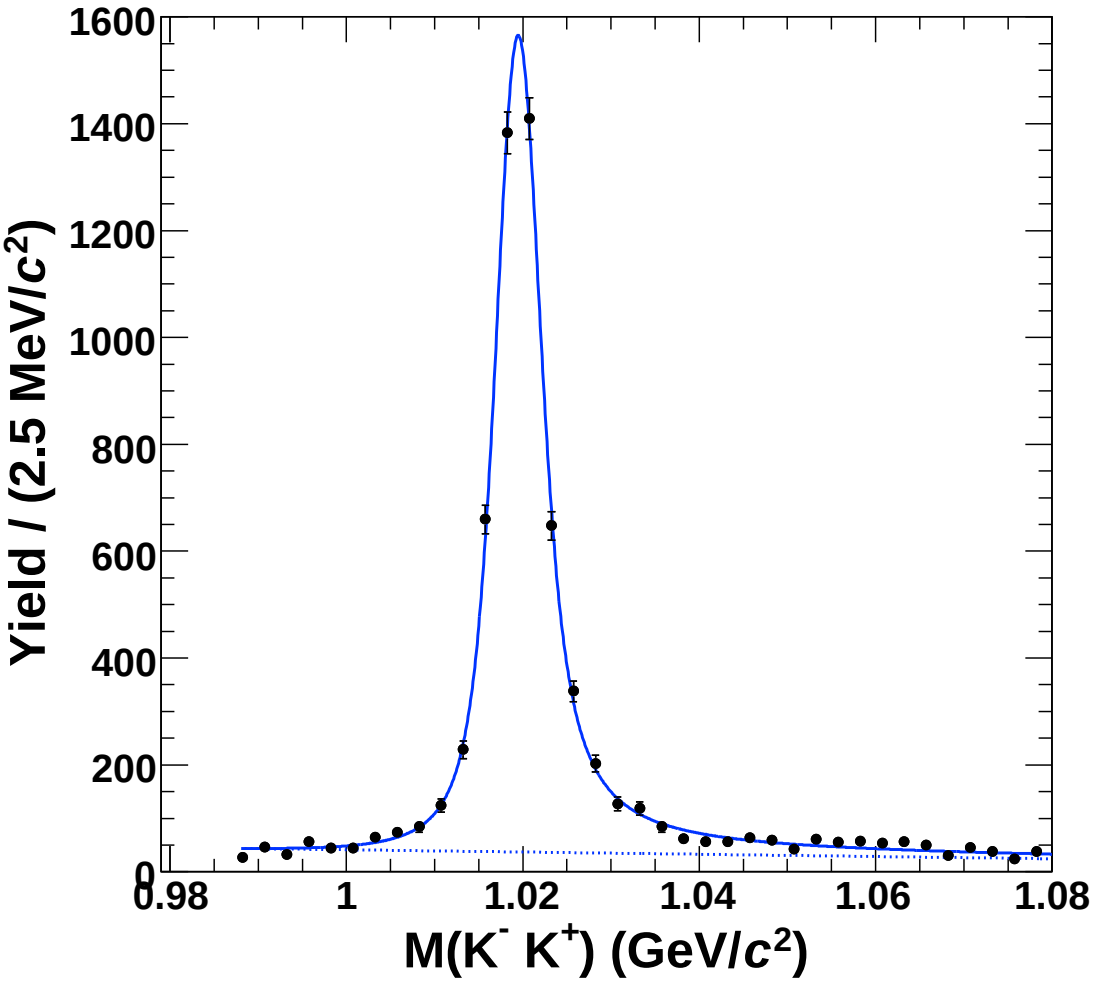

Figure 5.6: K^-K^+ mass spectrum overlaid with fit from [35]. Note that this figure has 2.5 MeV/c^2 mass bins while the fit in [35] is to 3 MeV/c^2 bins. The solid line is the total lineshape, while the dotted line is the scalar contribution.

5.11 *CP* Asymmetries

The branching fraction analysis assumes that D_s^+ and D_s^- have equal decay rates to each final state. Any violation would indicate direct *CP* violation, which is expected to be small in the charm system. Nevertheless we have the information to derive asymmetry measurements for each of our modes, none of which have previous measurements.

We define the asymmetry

$$\mathcal{A}_{CP}(i) = \frac{N_i/\epsilon_i - N_{\bar{\imath}}/\epsilon_{\bar{\imath}}}{N_i/\epsilon_i + N_{\bar{\imath}}/\epsilon_{\bar{\imath}}}$$

where N_i and ϵ_i ($N_{\bar{\imath}}$ and $\epsilon_{\bar{\imath}}$) are the measured yield and expected efficiency for single tag mode i ($\bar{\imath}$). The statistical uncertainties are treated as uncorrelated between the two ST measurements for a mode.

Almost all systematics cancel in this ratio; in particular the large π^0 and η uncertainties do not affect this measurement. We still include the ST efficiency statistical uncertainty and the ST yield fit uncertainties; however the excursions of D_s^+ and D_s^- yields under the fit function changes in the latter are almost completely correlated and so have a much smaller effect on the asymmetries than on the branching fractions. We now include an additional source of systematic uncertainty due to charge dependence in tracking and particle identification. These are taken from the D^0/D^+ analysis [32], and contribute 0.3–0.9%. The combination K^-K^+ is assigned one kaon systematic uncertainty (since the two kaons need not have the same momentum spectrum, full cancellation of systematics should not be expected, but partial cancellation is likely). Similarly, the $\pi^+\pi^+\pi^-$ mode is treated as two pions. We use the higher kaon PID systematic for the $K_S^0K^+$ mode due to the higher momentum kaon (where the RICH is very important). The pions from $K_S^0 \to \pi^+\pi^-$ and $\eta' \to \pi^+\pi^-\eta$ will have the same momentum spectrum, and so cancel.

The results are listed in Table 7.4. No significant asymmetries are observed, as expected. The stability of the asymmetry for $K^0_S K^+$ and $K^- K^+ \pi^+$ is used as a check for detector systematic effects in Section 6.2.

CHAPTER 6

SYSTEMATIC UNCERTAINTIES

Table 6.1: Pulls on the fits to generic Monte Carlo samples, computed using statistical uncertainties only. The 20×† sample is the 20× sample with the $K^-K^+\pi^+/K^+K^-\pi^-$ DT yield excluded from the fit. The χ^2 is relative to the known Monte Carlo parameters, and has 9 degrees of freedom.

Parameter	Sample		
	10×	20×	20×†
$N_{D_s^*D_s}$	-1.0σ	-2.1σ	$+1.2\sigma$
$\mathcal{B}(K_S^0K^+)$	$+1.2\sigma$	$+2.9\sigma$	$+2.1\sigma$
$\mathcal{B}(K^-K^+\pi^+)$	$+1.6\sigma$	$+2.8\sigma$	$+1.6\sigma$
$\mathcal{B}(K^-K^+\pi^+\pi^0)$	$+0.8\sigma$	-0.0σ	-0.5σ
$\mathcal{B}(K_S^0K^-\pi^+\pi^+)$	-0.4σ	$+1.6\sigma$	$+1.0\sigma$
$\mathcal{B}(\pi^+\pi^+\pi^-)$	$+1.6\sigma$	$+2.7\sigma$	$+2.0\sigma$
$\mathcal{B}(\pi^+\eta)$	$+0.3\sigma$	-0.2σ	-0.8σ
$\mathcal{B}(\pi^+\eta')$	$+0.4\sigma$	-0.4σ	-0.6σ
$\mathcal{B}(K^+\pi^+\pi^-)$	-0.5σ	$+0.2\sigma$	-0.2σ
χ^2	10.5	28.7	22.5

6.1 Fitter Cross-Check

To verify the internal consistency of our Monte Carlo and fitter, we fit two generic Monte Carlo samples (a 10× and a 20× sample) with the same procedures as for data. The resulting (statistical-only) pulls, and the overall χ^2 values relative to the true parameters, are shown in Table 6.1. In this table we also show the results for the 20× sample if the $K^-K^+\pi^+/K^+K^-\pi^-$ double tag mode is excluded from the fit; this one mode has a roughly 3σ upwards fluctuation, and the effect it has on the result is clearly visible (excluding it reduces the χ^2 from 28.7 to 22.5).

Although background shape systematic uncertainties are applicable when fitting generic Monte Carlo, they are not included in the pulls shown in the table. These uncertainties are roughly the size of the statistical uncertainties in the 20× sample (about twice as large for $K^-K^+\pi^+\pi^0$). We should not be surprised therefore to see $O(1\sigma)$ biases in the 20× sample for this reason. We decide not to correct for any such biases when fitting the data because it is unclear that the MC would correctly model them.

Extrapolating from the generic MC fits with uncertainties scaling as $1/\sqrt{N}$, there is no evidence for biases exceeding $\sim 0.6\sigma$ in the 298 pb^{-1} dataset. We consider this a confirmation of the integrity of the analysis.

6.2 Stability

To confirm the stability of detector operation and our selection criteria, we subdivide the 298 pb^{-1} sample into the component datasets 39, 40, and 41. The charge-combined (but not efficiency-corrected) single tag yields for $K^0_SK^+$ and $K^-K^+\pi^+$, divided by the luminosity for those runs, are shown in Figure 6.1. We observe consistent behavior in the three datasets.

6.3 Charge Asymmetry

The charge asymmetry by dataset is shown in Figure 6.2. For $K^-K^+\pi^+$ the observed ratio is exactly consistent with MC expectations; for $K^0_SK^+$ the observed ratio is about 2σ high. No significant time-dependent effects are observed.

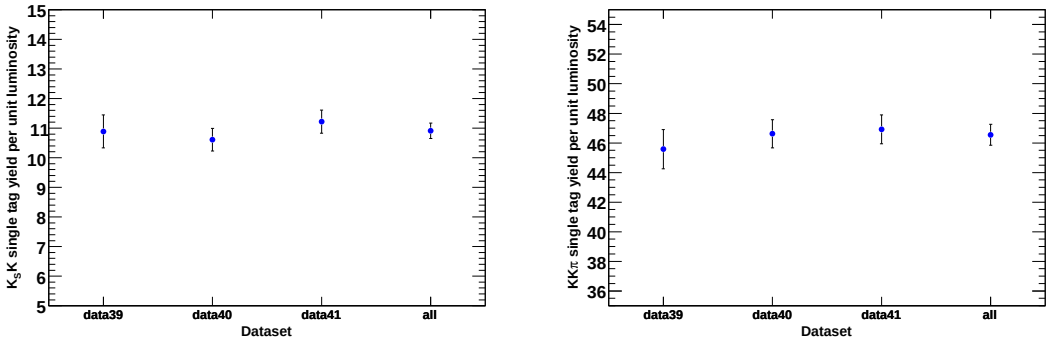

Figure 6.1: Charge-summed single tag yields per pb^{-1} for $K^0_S K^+$ (left) and $K^- K^+ \pi^+$ (right), separated by dataset.

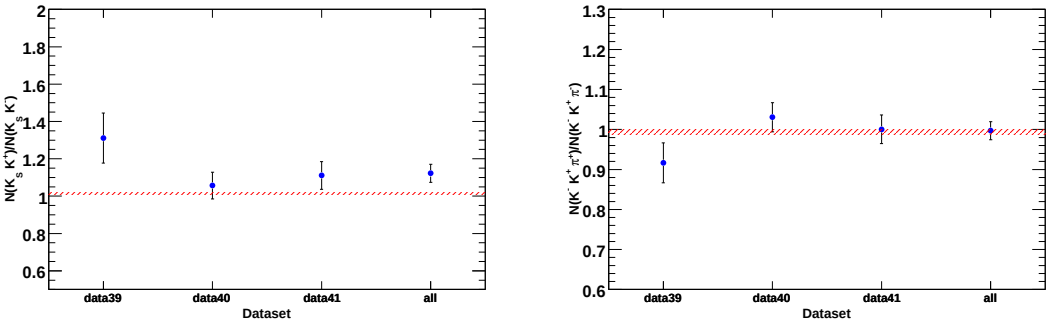

Figure 6.2: Reconstructed D_s^+/D_s^- ratio, without efficiency correction, for $K^0_S K^+$ (left) and $K^- K^+ \pi^+$ (right), separated by dataset. The red slashed band indicates the predicted value of the ratio from Monte Carlo.

6.4 Reconstruction

We can verify the quality of the Monte Carlo simulation of particle reconstruction as follows. Due to the constrained e^+e^- initial state and low multiplicity of most events, many events can be fully reconstructed — the four-momentum vector of every particle can be obtained directly, and the kinematics are overconstrained. If one avoids searching for one of the final state particles, the information from the other particles together with the initial state can be used to determine the

energy and momentum of the extra particle. From this we can compute a "missing mass" $M_{\rm miss}$ (or, usually, $M^2_{\rm miss}$) which peaks at the mass of the missing particle. This partial reconstruction method allows a determination of efficiency using data, which can be compared to MC predictions.

We take the following systematic uncertainties due to particle reconstruction: 0.3% per charged track; 0.6% per charged kaon; 1.9% per K^0_S; 2% per π^0 (with a correction of −3.9%); and 4% per η (with a correction of −5.7%). All except the K^0_S and η systematics are taken from studies done for the 281 pb^{-1} D^0/D^+ hadronic branching fraction analysis [32]. Tracking efficiencies are verified using the pions in $\psi' \to \pi^+\pi^- J/\psi \to \pi^+\pi^-\ell^+\ell^-$ and various D final states in $\psi(3770) \to D\overline{D}$; the larger kaon uncertainty arises because the $\pi^+\pi^- J/\psi$ cross-check cannot be made for these. Neutral pion efficiencies are checked with $\psi' \to \pi^0\pi^0 J/\psi \to \pi^0\pi^0\ell^+\ell^-$.

The eta efficiency has been studied using $\psi' \to \eta J/\psi$ decays (see Appendix B), and is here assigned a large error due to the extrapolation in η momentum from that regime. All η' candidates get the η systematic as well.

We start with the K^0_S systematic uncertainty from the D^0/D^+ analysis, obtained using $D\overline{D}$ events. The K^0_S candidates used here have a significantly tighter mass cut (6.3 MeV/c^2 instead of 12 MeV/c^2), so a difference in mass resolution would create an additional systematic difference. To study this, we compute the ratio between the yield of candidates in the standard 6.3 MeV/c^2 window and those in the window between 6.3 and 12 MeV/c^2 in $D^+_s \to K^0_S K^+$. The fraction of events in the 6.3 MeV/c^2 window is (96.4 ± 0.1)% in signal MC and (96.5 ± 0.7)% in data; we add the 0.7% uncertainty here in quadrature with the 1.8% reconstruction efficiency uncertainty from the D^0/D^+ analysis to get 1.9%.

6.5 Intermediate Resonance Decays

Our Monte Carlo simulation of K^0_S decays uses $\mathcal{B}(K^0_S \to \pi^+\pi^-) = 68.61\%$. The PDG 2007 fit for this branching fraction, driven by a new KLOE result [36], is $(69.20 \pm 0.05)\%$. We correct our efficiencies for this factor (an upward shift of 0.9%) and assign a relative uncertainty of 0.07% for decays with K^0_S daughters.

The PDG gives $\mathcal{B}(\eta \to \gamma\gamma) = (39.38 \pm 0.26)\%$ and $\mathcal{B}(\eta \to \pi^+\pi^-\eta) = (44.5 \pm 1.4)\%$, which have relative uncertainties of 0.7% and 3.1%, respectively. These uncertainties are applied to the $\pi^+\eta$ and $\pi^+\eta'$ decays (both are applied to the latter).

6.6 Charged Particle Identification

For D^0 and D^+ decays, particle identity assignments can often be made by requiring that the total energy be consistent with a D; for example, in $D^0 \to K^-\pi^+$, calling the K^- a π^- or the π^+ a K^+ changes the total D^0 candidate energy by many times the experimental resolution. It is thus possible to compare "partially-reconstructed" single tag events with all but one particle having positive identification and the subset where all daughters have good PID. This determines PID efficiency from data which can be compared with Monte Carlo predictions.

Such a study was performed using the decays $D^0 \to K^-\pi^+\pi^0$, $D^0 \to K^0_S\pi^+\pi^-$, and $D^+ \to K^-\pi^+\pi^+$ [37]. Discrepancies were found between data and Monte Carlo; data efficiencies are lower by roughly 0.5% per $\pi^\pm$ and 1% per $K^\pm$, averaged over all momenta. We apply corrections for this effect to the efficiencies obtained from MC. The corrections depend on the momenta of the daughter particles, so we determine a different correction for each D^+_s decay mode. From the particle spectrum (with PID) in signal Monte Carlo, we compute the following: for every

Table 6.2: Charged particle ID efficiency corrections and systematics.

Mode	Correction	Systematic
$K^0_S K^+$	0.989	0.003
$K^- K^+ \pi^+$	0.972	0.008
$\rightarrow (\phi\pi^+)$	0.973	
$\rightarrow (\overline{K}^{*0} K^+)$	0.968	
$K^- K^+ \pi^+ \pi^0$	0.963	0.014
$\rightarrow (\phi\pi^+\pi^0)$	0.955	
$\rightarrow (\overline{K}^{*0} K^+\pi^0)$	0.975	
$\pi^+\pi^+\pi^-$	0.989	0.006
$\pi^+\eta$	0.998	0.002
$\pi^+\eta'$	0.968	0.006
$K^+\pi^+\pi^-$	0.980	0.007

event

$$\epsilon_{MC,data} = \prod_{X \in particles} \epsilon_{MC,data}(X, |\vec{p}_X|)$$

is the PID efficiency in data or Monte Carlo for that particular set of final state particles and momenta, and

$$\frac{\epsilon_{data}}{\epsilon_{MC}} = \frac{\sum_{E \in events} \epsilon_{data}(E)/\epsilon_{MC}(E)}{N_{events}}$$

is the ratio of the mean data efficiency to the mean MC efficiency for the momentum spectrum in the Monte Carlo.

The corrections and systematics are summarized in Table 6.2. The systematic on the corrections quoted in [37] is 0.2% for pions and 0.3% for kaons. We use these estimates, in quadrature with the variations in the correction observed by

selecting different subprocesses, to set the scale of the systematic uncertainty. The large correction in $\pi^+\eta'$ is due to the two soft pions in the $\eta' \to \pi^+\pi^-\eta$ transition being subjected to the standard particle ID.

We observe significant data/MC discrepancies due to a wider dE/dx distribution in data at low kaon momentum. We are particularly sensitive to this in D_s^+ decays because of the higher kaon multiplicity and the frequent occurrence of ϕ decays which produce low-momentum kaons.

6.7 Resonant Substructure

The resonant substructures of the inclusive multibody modes in this analysis are poorly established, in contrast to the situation for D^0/D^+, where full Dalitz amplitudes are often available for three-body modes. Since the different intermediate resonances produce different final-state momenta and angular distributions, the overall efficiency for the inclusive mode depends on the fraction for each subdecay. Since this systematic is completely correlated within each mode (both single and double tags), no mode is affected by the uncertainty in any other mode. Likewise the number of $D_s^{*\pm}D_s^{\mp}$ pairs is independent of this uncertainty.

We can determine a correction and associated systematic uncertainty by using signal Monte Carlo to determine the efficiencies of various resonant substates, then weighting their contribution by what is reconstructed in the data.

6.7.1 $K_S^0K^+$, $\pi^+\eta$

These two-body modes have no such uncertainty.

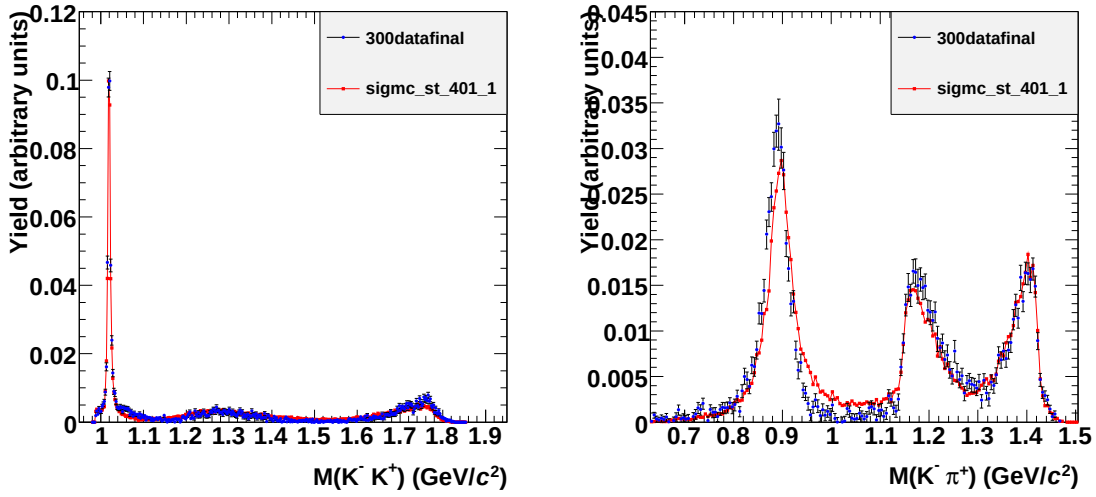

Figure 6.3: Background-subtracted mass distributions for K^-K^+ (left) and $K^-\pi^+$ (right) in $D_s^+ \to K^-K^+\pi^+$. Blue points are data and red points connected by lines are signal MC.

6.7.2 $K^+K^-\pi^+$

The two major resonant contributors to this decay are $\phi\pi^+$ and $\overline{K}^{*0}K^+$. There are also reasonably large fractions of $f_0(980)\pi^+$ and other decays. The $\phi\pi^+$ and $\overline{K}^{*0}K^+$ components turn out to have much the same efficiency, while the "other" components, dominated by phase-space distributed three-body decay in the Monte Carlo, is about 7% relative higher. Data/MC comparisons for mass distributions are shown in Figure 6.3. In data we see roughly 4990 events from $\phi\pi^+$, 4770 from $\overline{K}^{*0}K^+$, and 4180 events from neither of those two sources. Depending whether the excess behaves more like $\phi\pi^+$ (the lowest efficiency) or like the "other" components, the overall efficiency correction can vary from −1.7% to +0.6%. We take no correction, with a ± 1.5% systematic.

6.7.3 $K^+K^-\pi^+\pi^0$

This mode is dominated by the two components $\phi\pi^+\pi^0$ and $\overline{K}^{*0}K^+\pi^0$. These two decays have markedly different efficiency because the ϕ in the first case is very slow (most of the $\pi^+\pi^0$ comes from a ρ^+) and the daughter kaons are correspondingly very soft. We find $\epsilon(\phi X)/\epsilon(\overline{K}^{*0}X) = 0.68$ in MC. Data/MC comparisons for mass distributions are shown in Figure 6.4. In data we see roughly 1400 events in ϕX, 1350 in $\overline{K}^{*0}X$, and 800 from neither. Depending on whether the extra acts more ϕX-like or more $\overline{K}^{*0}X$-like, we can see efficiency corrections from −2.4% to +9.0%. We apply a correction of +3.3 ± 6% on the efficiency in this mode.

6.7.4 $K^0_S K^-\pi^+\pi^+$

This mode is dominated by $K^{*+}\overline{K}^{*0}$. We find $\epsilon(K^0_S K^-\pi^+\pi^+ \text{ PHSP})/\epsilon(K^{*+}\overline{K}^{*0}) = 0.93$, and that changes in the helicity structure for $K^{*+}\overline{K}^{*0}$ change the efficiency by a not-statistically-significant 1.8%. Data/MC comparisons for mass distributions are shown in Figure 6.5. Varying the $K^{*+}\overline{K}^{*0}$ contribution by 50% of itself changes the efficiency by 2.3%, which we take as the systematic uncertainty for this mode.

6.7.5 $\pi^+\pi^+\pi^-$

In Monte Carlo, this mode is dominated by the decay $D_s^+ \to f_0(980)\pi^+$. In data we see additional contributions from $f_0(1370)\pi^+$ and $f_2(1270)\pi^+$. Data/MC comparisons for mass distributions are shown in Figure 6.6. A Dalitz analysis from E791 finds no significant nonresonant component [38]. We find $\epsilon(f_0(1370)\pi^+)/\epsilon(f_0(980)\pi^+) = 1.020$ and $\epsilon(f_2(1270)\pi^+)/\epsilon(f_0(980)\pi^+) = 1.036$. The standard mixture has an efficiency 0.6% higher than $f_0(980)\pi^+$. We also mocked

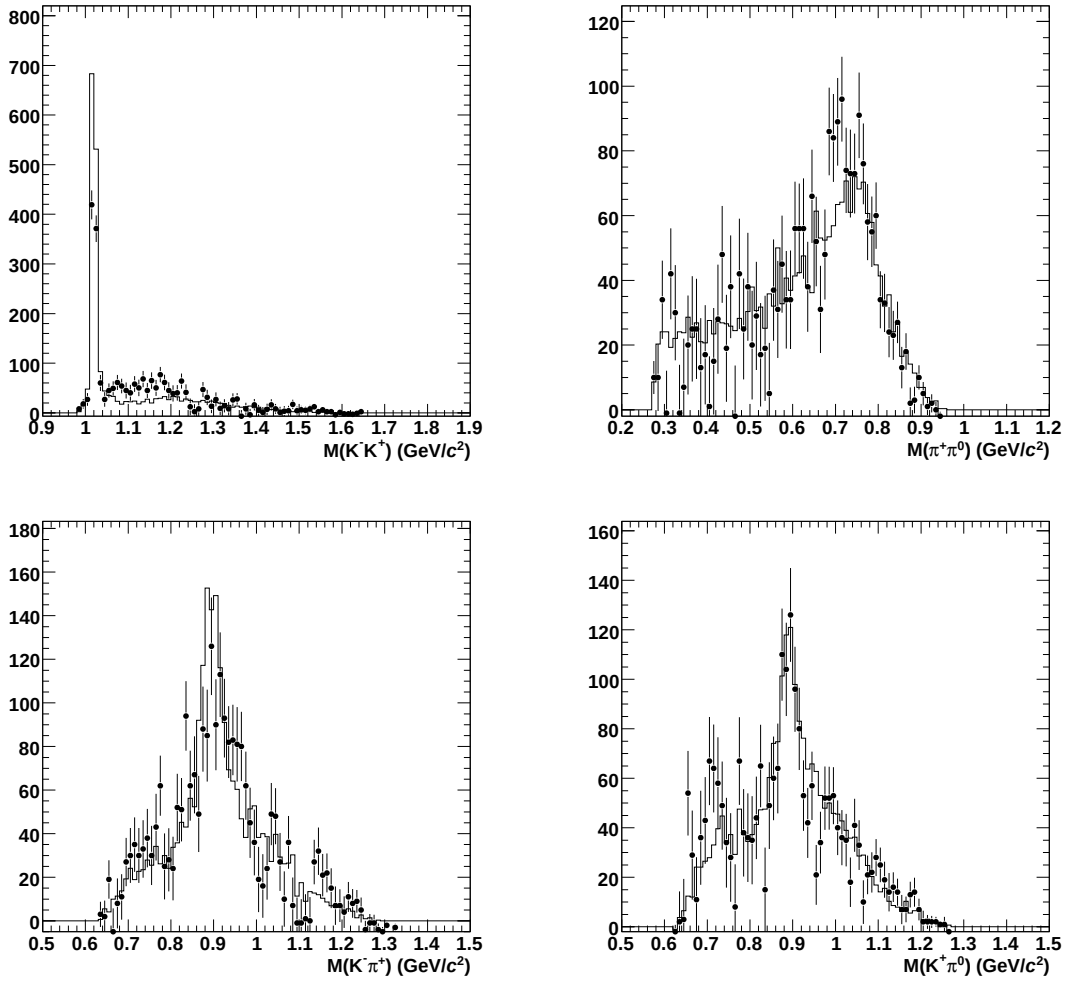

Figure 6.4: Background-subtracted mass distributions for K^-K^+ (top left), $\pi^+\pi^0$ (top right), $K^-\pi^+$ (bottom left), and $K^+\pi^0$ (bottom right) in $D_s^+ \to K^-K^+\pi^+\pi^0$. Points are data and histogram is signal MC. Particularly tight $M_{\rm rec}$ selections were used to prepare these plots, so yields should not be compared with the rest of the text.

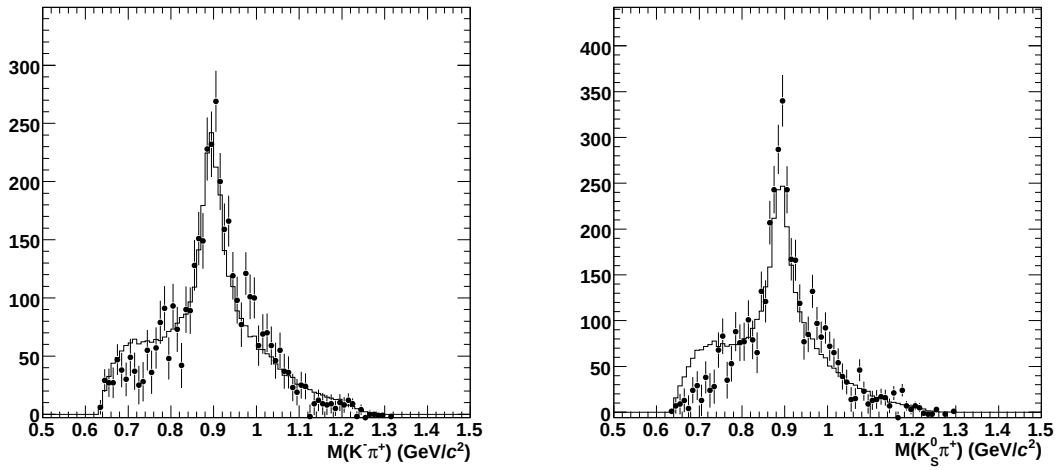

Figure 6.5: Background-subtracted mass distributions for $K^-\pi^+$ (left) and $K^0_S\pi^+$ (right) in $D^+_s \to K^0_S K^-\pi^+\pi^+$. Every event contributes two entries in both plots. Points are data and histogram is signal MC. Peaks for the $K^*(892)$ are visible.

up a full Dalitz amplitude which had proportionally too little $f_0(980)\pi^+$ when compared to data; this had an efficiency 1.2% higher than that for $f_0(980)\pi^+$. For the analysis, we take the MC efficiency with no correction and a 2% systematic uncertainty.

6.7.6 $\pi^+\eta'$

We ignore the slight variations in the matrix element for the $\eta' \to \pi\pi\eta$ decay [39].

6.7.7 $K^+\pi^+\pi^-$

A FOCUS analysis [40] determines the dominant contributions to this decay to be $K^+\rho^0$, $K^{*0}\pi^+$, $K^*(1410)^0\pi^+$, and a non-resonant piece. The vector $K\pi$ resonances produce large concentrations of events at low $\pi\pi$ mass, which leads to a sig-

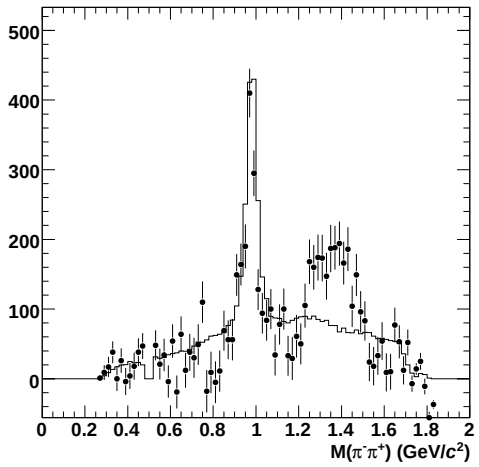

Figure 6.6: Background-subtracted mass distributions for $\pi^+\pi^-$ in $D_s^+ \to \pi^+\pi^+\pi^-$. Every event contributes two entries. Points are data and histogram is signal MC. A discrepancy is clearly seen in the 1.2–1.5 GeV/c^2 region.

nificant efficiency loss due to the K_S^0 veto; for example $\epsilon(K^{*0}\pi^+)/\epsilon(K^+\rho^0) = 0.87$. The statistics in this mode are too poor to do more than observe evidence for the $K^{*0}\pi^+$ channel (see Figure 6.7). If we vary the $K^{*0}\pi^+$ contribution by 50%, the expected efficiency changes by 1.5% relative, which we take as the systematic uncertainty.

6.8 Isospin-violating D_s^{*+} Decays

The small fraction of isospin-suppressed decays $D_s^{*+} \to \pi^0 D_s^+$ result in a different momentum distribution of the daughter D_s^+ than do the dominant $D_s^+ \to \gamma D_s^+$ decays. This could in theory affect the efficiencies of the modes with tight $M_{\rm rec}$ cuts, because they preferentially reject events from $D_s^* \to \gamma D_s$. However since only 20% of events are lost, and the absolute uncertainty on $\mathcal{B}(D_s^{*+} \to D_s^+\pi^0)$ is 0.7%, the possible effect is $O(0.14\%)$, which we ignore.

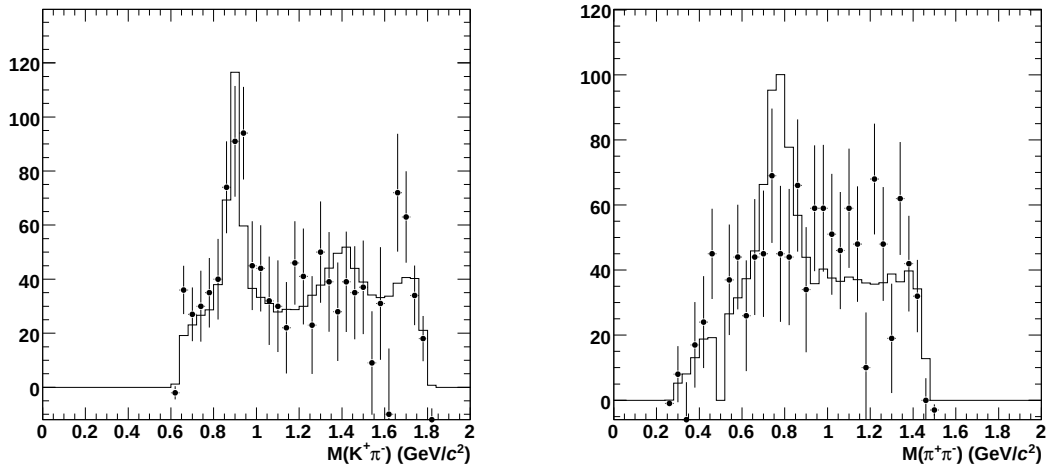

Figure 6.7: Background-subtracted mass distributions for $K^+\pi^-$ (left) and $\pi^+\pi^-$ (right) in $D_s^+ \to K^+\pi^+\pi^-$. Points are data and histogram is signal MC. A $K^*(892)^0$ peak is visible.

6.9 Peaking Backgrounds

Because we use invariant mass as our fit variable, the only peaking contributions we expect are decays that produce the same final state that we are looking for. In practice there are two backgrounds that peak:

- The Cabibbo-suppressed $D_s^+ \to K_S^0\pi^+$ fakes the $\pi^+\pi^+\pi^-$ final state. We explicitly veto events where a $\pi^+\pi^-$ combination is near the K_S^0 mass, so we do not evaluate a background contribution.
- The Cabibbo-suppressed $D_s^+ \to K^+\pi^+\pi^-$ can fake $K_S^0\pi^+$. We use sideband regions 0.472 GeV $< m(\pi^+\pi^-) <$ 0.4783 GeV and 0.5171 GeV $< m(\pi^+\pi^-) <$ 0.5234 GeV to search for such a signal in the data. No signal is seen, and the limit is two events, so we ignore this background as well.

There is also an oddly shaped background in the $\pi^+\pi^+\pi^-$ mode from $D_s^+ \to (\eta, \eta')\pi^+ \to \pi^+\pi^-\pi^+\gamma$, where the photon is very soft. This forms a background that turns on for invariant mass less than the D_s^+ mass. However, from Monte

Carlo simulations, this is expected to contribute on the order of a percent or less (its main effect is to skew the background shape somewhat). Due to the small size of the effect compared to other systematics (and uncertainty over whether it actually biases the signal fit), we ignore it. Notice that, although the plots for the $\pi^+\pi^+\pi^-$ mode (Figure A.29) may appear to show a background discontinuity between low and high invariant mass, we have searched for the photon in this mode (reliably found in Monte Carlo) and do not see any signal from $\pi^+\eta$ or $\pi^+\eta'$.

6.10 Lineshapes

To study possible differences between the Monte Carlo lineshape and what is present in data, we perform two checks. First, we allow the overall width of the D_s^+ signal lineshape to float (keeping the relative normalization and relative width of the Gaussians fixed). Second, we switch the order of the background polynomial: the modes that are ordinarily fit with linear polynomials are now fit with a second-order function, and vice versa. The excursions in each case are used as separate systematic uncertainties. The observed variations are listed in Table 6.3.

Because the signal box in the double tag cut-and-count technique is not always large compared to the resolution, misunderstood widths also translate into errors on the double tag efficiencies, which are correlated with the single tag errors. We determine the size of these variations by assuming that the $M_{\rm inv}$ lineshapes are the same in single and double tag events, then using toy Monte Carlo to determine the efficiency change when the lineshapes are changed to the best fits determined from the data single tags. Most modes show little change;

Table 6.3: Single tag lineshape systematics. Middle two columns are yield excursions for using a different order background; right two columns are the excursions for allowing width and mass to float. All numbers in percent.

Mode	Background (%)		Width (%)	
	D_s^+	D_s^-	D_s^+	D_s^-
$K_S^0K^+$	−1.1	−1.1	+0.1	+0.1
$K^-K^+\pi^+$	−0.2	−0.2	+0.6	+0.6
$K^-K^+\pi^+\pi^0$	−8.9	−8.2	+1.9	+1.7
$K_S^0K^-\pi^+\pi^+$	+0.8	+0.7	+1.0	+0.7
$\pi^+\pi^+\pi^-$	−5.3	−5.3	+0.4	+0.4
$\pi^+\eta$	−6.8	−5.8	+10.3	+10.2
$\pi^+\eta'$	−3.1	−2.7	+6.0	+5.4
$K^+\pi^+\pi^-$	−2.3	−2.9	+4.5	+4.3

the largest variations are in $\pi^+\eta$ and $\pi^+\eta'$ where the data suggest widths $\sim 10\%$ wider than predicted.

6.11 Initial State Radiation

We have investigated the effects of ISR on efficiency. Initial state radiation affects us because when the initial $D_s^{*\pm}D_s^{\mp}$ state has less energy, the momenta of the D_s^+ candidates will be lower, leading to a high-side tail in $M_{\rm rec}$. For the loose $M_{\rm rec}$ cut, we accept all events from the lower kinematic limit to the beam energy, so the cut remains fully efficient regardless of ISR. Because the tight $M_{\rm rec}$ cut

depends on details of the $M_{\rm rec}$ distribution, the smearing due to ISR could affect the efficiencies of the single tags which use this cut.

To check the size of any possible effect, we compare single tag $K^-K^+\pi$ yields for the loose and tight cuts. In data we find $R_{\rm data} \equiv N(\text{loose})/N(\text{tight}) = 0.819 \pm 0.004$, and in the ISR MC $R_{\rm MC} = 0.824 \pm 0.002$. The central values differ by $(0.6 \pm 0.5)\%$.

We take no correction for this effect, with a 0.8% systematic uncertainty, in the three single tag modes ($K^-K^+\pi^+\pi^0$, $\pi^+\pi^+\pi^-$, and $K^+\pi^+\pi^-$) where we apply a tight $M_{\rm rec}$ cut.

6.12 Multiple Candidate Rate

If an event has more than one candidate, and we select one, there is some inefficiency associated with making an incorrect choice. This inefficiency is modelled in Monte Carlo. If the multiple candidate rate is significantly different in data and Monte Carlo, we are likely to see an efficiency difference.

We investigate the multiple candidate rates in generic MC by looking in signal and sideband regions of invariant mass for each of our four modes. The signal and sideband regions are $1.955\ \text{GeV}/c^2 < M_{\rm inv} < 1.98\ \text{GeV}/c^2$ and $1.90/c^2 < M_{\rm inv} < 1.93\ \text{GeV}/c^2$, respectively.

The sideband-subtracted candidate multiplicities are shown in Figures A.1–A.7. We see that the Monte Carlo and data are generally in good agreement.

If there is a difference between the data and MC multiple candidate rate, it means that one one case we must make a choice between different candidates more often. If we assume we do no better than randomly choose candidates (so, for example, the efficiency is down 50% for two candidates, 67% for three), we can limit the effect of this difference on the total efficiency. The fraction of

Table 6.4: Predicted fraction of correctly-chosen events, assuming random candidate choice, in Monte Carlo and data, and fractional difference. The fractional difference is used as the systematic uncertainty.

Mode	MC fraction (%)	Data fraction (%)	Data/MC-1 (%)
$K^0_S K^+$	99.6	99.7	0.1
$K^- K^+ \pi^+$	96.4	96.0	-0.4
$K^- K^+ \pi^+ \pi^0$	77.9	76.7	-1.4
$K^0_S K^- \pi^+ \pi^+$	89.2	89.2	-0.1
$\pi^+ \pi^+ \pi^-$	97.4	97.3	-0.2
$\pi^+ \eta$	96.6	96.7	0.1
$\pi^+ \eta'$	96.9	96.5	-0.5
$K^- \pi^+ \pi^+$	94.5	93.2	-1.4

candidates that would be correctly chosen, and the data/MC difference in this, are summarized in Table 6.4. We use the magnitude of this difference as the systematic uncertainty in each mode.

6.13 Final State Radiation

Final state radiation off the D_s^+ daughters lowers the invariant mass of the detected final state particles, taking the candidates out of the signal peak and reducing the efficiency. This is modeled with the PHOTOS 2.0 package; in particular the interference effects between different charged daughters are not taken into account.

Table 6.5: Relative shift in efficiency $\epsilon_{\text{no FSR}}/\epsilon_{\text{FSR}} - 1$ and assigned systematic uncertainty for each D_s^+ decay mode.

Mode	FSR effect (%)	Systematic Uncertainty (%)
$K_S^0 K^+$	0.68	0.20
$K^- K^+ \pi^+$	1.46	0.44
$K^- K^+ \pi^+ \pi^0$	0.98	0.29
$K_S^0 K^- \pi^+ \pi^+$	1.44	0.43
$\pi^+ \pi^+ \pi^-$	3.83	1.15
$\pi^+ \eta$	2.29	0.69
$\pi^+ \eta'$	2.04	0.31
$K^+ \pi^+ \pi^-$	2.54	0.76

We determine the size of the FSR efficiency shift by fitting signal MC where no descendants of the signal D_s^+ are permitted to radiate a photon. (For K_S^0, η and η' modes we only consider reconstructible decays.) The fit function is the same as that for the standard fit in that mode. We see relative effects ranging from 0.6% ($K_S^0 K^+$) to 3.8% ($\pi^+ \pi^+ \pi^-$).

We assign a systematic uncertainty for the FSR simulation of 30% of the FSR effect in each mode, correlated between D_s^+ and D_s^- efficiencies for the same mode. The total FSR effect and associated systematic uncertainty for each mode is shown in Table 6.5.

6.14 Trigger

We use a MC simulation of the trigger algorithms to determine the expected efficiency for the trigger on our events. In particular we want to determine the efficiency only on events that would otherwise be reconstructed; if daughters were not reconstructed by the offline software, they were most likely not found by the trigger hardware. In all our modes we find 99.9% efficiency or better, so we choose not to correct or assign a systematic uncertainty to the efficiency. Nevertheless it is worth discussing how this high efficiency comes about.

For modes with multiple prompt charged particles, the signal is almost always sufficient to fire the two track trigger. In particular double tags are efficient on this trigger line because all reconstructible DT events have at least two detected prompt charged particles in them. This is also true for all ST modes except $K^0_S K^+$ and $\pi^+\eta$, where in the first case the two K^0_S daughters might be produced far from the IP and so not be found as axial tracks, and in the second where there is in fact only one charged daughter. For single tag $K^0_S K^+$ the two track trigger inefficiency is less than 0.1%. Thanks to the other side likely having a reconstructible charged particle, even for single tag $\pi^+\eta$ the two-track trigger is 95.5% efficient. The eltrack trigger (track+medium barrel shower) is 97.5% efficient, and the combination of the two is 99.9% efficient.

Table 6.6: Summary of systematic uncertainties for inclusive branching fraction measurements. This list excludes systematics from MC statistics and fit function systematics obtained in the data fits.

Source	Uncertainty (%)	Affects
Detector Simulation	0.3	Track reconstruction
	0.6	Kaon track reconstruction
	1.9	K^0_S reconstruction
	2.0	π^0 reconstruction
	4.0	η reconstruction
Intermediate Decays	0.07	K^0_S efficiencies
	0.7	η efficiencies
	3.1	η' efficiencies
Particle ID	0.3–1.4 (See Table 6.2)	All efficiencies
Resonant substructure	1.5	$K^-K^+\pi^+$ efficiencies
	6.0	$K^-K^+\pi^+\pi^0$ efficiencies
	2.3	$K^0_SK^-\pi^+\pi^+$ efficiencies
	2.0	$\pi^+\pi^+\pi^-$ efficiencies
	1.5	$K^+\pi^+\pi^-$ efficiencies
ST fit lineshapes	0.3–11.3 (See Table 6.3)	ST yields
DT lineshapes	0–8	DT efficiencies, correlated with ST yields
ISR	0.8	$K^-K^+\pi^+\pi^0$, $\pi^+\pi^+\pi^-$, $K^+\pi^+\pi^-$ ST efficiencies
Multiple candidate rate	0.1–1.4 (See Table 6.4)	ST efficiencies
FSR	0.2–1.2 (see Table 6.5)	All efficiencies

Table 6.7: Breakdown of sources of final systematic uncertainty. Displayed values are relative to the parameters obtained in the final fit.

	$N_{D_s^* D_s}$	$K_S K^+$	$K^- K^+ \pi^+$	$K^- K^+ \pi^+ \pi^0$	$K_S K^- \pi^+ \pi^+$	$\pi^+ \pi^+ \pi^-$	$\pi^+ \eta$	$\pi^+ \eta'$	$K^+ \pi^+ \pi^-$
Tracking efficiency	0.0	0.9	0.9	0.9	1.5	0.9	0.3	0.9	0.9
Kaon tracking efficiency	0.0	0.6	1.2	1.2	0.6	0.0	0.0	0.0	0.6
KShort efficiency	0.0	1.9	0.0	0.0	1.9	0.0	0.0	0.0	0.0
Pi0 efficiency	0.0	0.0	0.0	2.0	0.0	0.0	0.0	0.0	0.0
Eta efficiency	0.0	0.0	0.0	0.0	0.0	0.0	4.2	4.2	0.0
KS BR	0.0	0.1	0.0	0.0	0.1	0.0	0.0	0.0	0.0
Eta BR	0.0	0.0	0.0	0.0	0.0	0.0	0.7	0.7	0.0
Eta Prime BR	0.0	0.0	0.0	0.0	0.0	0.0	0.0	3.0	0.0
PID Correction uncertainty	0.0	0.3	0.8	1.4	0.7	0.6	0.2	0.6	0.7
ISR modeling	0.4	0.3	0.3	0.2	0.3	0.2	0.3	0.3	0.1
FSR modeling, mode 400	0.0	0.2	0.0	0.0	0.0	0.0	0.0	0.0	0.0
Total (all syst)	2.1	3.0	2.9	7.1	4.0	3.8	11.2	8.0	4.0

Table 6.7 (Continued)

	$N_{D_s^+ D_s^-}$	$K_S K^+$	$K^- K^+ \pi^+$	$K^- K^+ \pi^+ \pi^0$	$K_S K^- \pi^+ \pi^+$	$\pi^+ \pi^+ \pi^-$	$\pi^+ \eta$	$\pi^+ \eta'$	$K^+ \pi^+ \pi^-$
FSR modeling, mode 401	0.0	0.0	0.4	0.0	0.0	0.0	0.0	0.0	0.0
FSR modeling, mode 404	0.0	0.0	0.0	0.3	0.0	0.0	0.0	0.0	0.0
FSR modeling, mode 406	0.0	0.0	0.0	0.0	0.4	0.0	0.0	0.0	0.0
FSR modeling, mode 421	0.0	0.0	0.0	0.0	0.0	1.1	0.0	0.0	0.0
FSR modeling, mode 440	0.0	0.0	0.0	0.0	0.0	0.0	0.7	0.0	0.0
FSR modeling, mode 460	0.0	0.0	0.0	0.0	0.0	0.0	0.0	0.3	0.0
FSR modeling, mode 502	0.0	0.0	0.0	0.0	0.0	0.0	0.0	0.0	0.8
Dalitz Correction, mode 401	0.0	0.0	1.5	0.0	0.0	0.0	0.0	0.0	0.0
Dalitz Correction, mode 404	0.0	0.0	0.0	5.7	0.0	0.0	0.0	0.0	0.0
Dalitz Correction, mode 406	0.0	0.0	0.0	0.0	2.2	0.0	0.0	0.0	0.0
Dalitz Correction, mode 421	0.0	0.0	0.0	0.0	0.0	2.0	0.0	0.0	0.0
Total (all syst)	2.1	3.0	2.9	7.1	4.0	3.8	11.2	8.0	4.0

Table 6.7 (Continued)

	$N_{D_s^{*}D_s}$	$K_S K^+$	$K^- K^+ \pi^+$	$K^- K^+ \pi^+ \pi^0$	$K_S K^- \pi^+ \pi^+$	$\pi^+ \pi^+ \pi^-$	$\pi^+ \eta$	$\pi^+ \eta'$	$K^+ \pi^+ \pi^-$
Dalitz Correction, mode 502	0.0	0.0	0.0	0.0	0.0	0.0	0.0	0.0	1.5
Width correction, mode 400	0.0	0.0	0.0	0.0	0.0	0.0	0.0	0.0	0.0
Width correction, mode 401	0.6	0.5	0.0	0.4	0.5	0.4	0.5	0.5	0.4
Width correction, mode 404	0.2	0.2	0.2	1.0	0.2	0.1	0.1	0.2	0.1
Width correction, mode 406	0.1	0.1	0.1	0.1	0.6	0.1	0.1	0.1	0.1
Width correction, mode 421	0.1	0.0	0.0	0.0	0.0	0.2	0.0	0.0	0.0
Width correction, mode 440	0.2	0.2	0.2	0.1	0.2	0.1	9.6	0.3	1.1
Width correction, mode 460	0.2	0.2	0.2	0.2	0.2	0.2	0.2	5.2	0.3
Width correction, mode 502	0.3	0.3	0.3	0.3	0.3	0.3	0.3	0.3	2.4
ST Bkg Shape uncertainty, mode 400	0.3	0.7	0.2	0.2	0.2	0.2	0.2	0.2	0.2
ST Bkg Shape uncertainty, mode 401	0.2	0.1	0.0	0.1	0.1	0.1	0.1	0.1	0.1
Total (all syst)	2.1	3.0	2.9	7.1	4.0	3.8	11.2	8.0	4.0

Table 6.7 (Continued)

	$N_{D_s^{*}D_s}$	$K_S K^+$	$K^- K^+ \pi^+$	$K^- K^+ \pi^+ \pi^0$	$K_S K^- \pi^+ \pi^+$	$\pi^+ \pi^+ \pi^-$	$\pi^+ \eta$	$\pi^+ \eta'$	$K^+ \pi^+ \pi^-$
ST Bkg Shape uncertainty, mode 404	1.6	1.5	1.5	2.9	1.4	1.2	1.4	1.6	1.2
ST Bkg Shape uncertainty, mode 406	0.1	0.1	0.1	0.1	0.5	0.1	0.1	0.1	0.1
ST Bkg Shape uncertainty, mode 421	0.8	0.7	0.7	0.6	0.7	2.4	0.6	0.7	0.6
ST Bkg Shape uncertainty, mode 440	0.5	0.5	0.5	0.4	0.5	0.4	3.5	0.5	0.4
ST Bkg Shape uncertainty, mode 460	0.2	0.2	0.2	0.2	0.2	0.2	0.2	2.1	0.2
ST Bkg Shape uncertainty, mode 502	0.2	0.2	0.2	0.2	0.2	0.2	0.2	0.2	1.2
Multiple Candidate uncertainty, mode 400	0.0	0.1	0.0	0.0	0.0	0.0	0.0	0.0	0.0
Multiple Candidate uncertainty, mode 401	0.4	0.4	0.0	0.3	0.4	0.3	0.3	0.4	0.3
Multiple Candidate uncertainty, mode 404	0.3	0.3	0.3	0.5	0.3	0.2	0.2	0.3	0.2
Multiple Candidate uncertainty, mode 406	0.0	0.0	0.0	0.0	0.1	0.0	0.0	0.0	0.0
Multiple Candidate uncertainty, mode 421	0.0	0.0	0.0	0.0	0.0	0.1	0.0	0.0	0.0
Total (all syst)	2.1	3.0	2.9	7.1	4.0	3.8	11.2	8.0	4.0

Table 6.7 (Continued)

	$N_{D_s^* D_s}$	$K_S K^+$	$K^- K^+ \pi^+$	$K^- K^+ \pi^+ \pi^0$	$K_S K^- \pi^+ \pi^+$	$\pi^+ \pi^+ \pi^-$	$\pi^+ \eta$	$\pi^+ \eta'$	$K^+ \pi^+ \pi^-$
Multiple Candidate uncertainty, mode 440	0.0	0.0	0.0	0.0	0.0	0.0	0.1	0.0	0.0
Multiple Candidate uncertainty, mode 460	0.0	0.0	0.0	0.0	0.0	0.0	0.0	0.4	0.0
Multiple Candidate uncertainty, mode 502	0.1	0.1	0.1	0.1	0.1	0.1	0.1	0.1	0.6
Total (all syst)	2.1	3.0	2.9	7.1	4.0	3.8	11.2	8.0	4.0

6.15 Summary

The accounted-for sources of systematic uncertainty are listed in Table 6.6. It is not always obvious how a particular systematic uncertainty affects the final result, so the source-by-source contributions to the final branching fraction result uncertainties are listed in Table 6.7.

CHAPTER 7

RESULTS AND CONCLUSION

The results are summarized in Tables 7.1– 7.4 and Figure 7.1. In addition we obtain

$$N_{D_s^* D_s} = (2.93 \pm 0.14(\text{stat}) \pm 0.06(\text{syst})) \times 10^5;$$

this gives

$$\sigma_{D_s^* D_s}(4.170\ \text{GeV}) = 0.983 \pm 0.046(\text{stat}) \pm 0.021(\text{syst}) \pm 0.010(\text{lum})\ \text{nb}.$$

The most precise branching fraction measured in this analysis is $\mathcal{B}(K^-K^+\pi^+)$, with a relative uncertainty of 5.1% (adding statistical and systematic uncertainties in quadrature). By comparison, the world average of that value had an uncertainty of 15%; the value $\mathcal{B}(\phi\pi^+)$ had a 9% uncertainty (and as we have pointed out that value is subject to the systematics of how it is defined). This is represents the most precise value available for any D_s^+ decay branching fraction by nearly a factor of two. In addition the measurements for all other modes are improvement on the world averages; for $\mathcal{B}(K^-K^+\pi^+\pi^0)$ it is a first measurement.

The CLEO-c experiment has since taken more data with $E_{\text{cm}} = 4.17$ GeV, increasing the total recorded luminosity to approximately 590 pb^{-1}. With no other changes in the analysis, the statistical precision on $\mathcal{B}(K^-K^+\pi^+)$ can be brought to $\approx 3.0\%$, roughly equal to the systematic uncertainty. Both of these can be improved from this straight projection. To improve statistical precision, the only real method is to add more modes; as earlier discussed, increasing the total number of reconstructed double tags improves all branching fraction measurements. The systematic uncertainties will hopefully benefit from improved background simulation enabled by the improved branching fraction scale set by the current measurement, as well as improved statistical precision for data-Monte Carlo comparisons.

In conclusion, we have described a precision measurement of eight branching fractions of the D_s^+ meson, performed with the CLEO-c detector using a double

Table 7.1: Results of the branching fraction fit for this analysis and comparison to the PDG 2007 fit result. For our results uncertainties are statistical and systematic, respectively.

Mode	This Result (%)	PDG 2007 fit (%)
$\mathcal{B}(K_S^0K^+)$	$1.49 \pm 0.07 \pm 0.05$	2.2 ± 0.4
$\mathcal{B}(K^-K^+\pi^+)$	$5.50 \pm 0.23 \pm 0.16$	5.3 ± 0.8
$\mathcal{B}(K^-K^+\pi^+\pi^0)$	$5.65 \pm 0.29 \pm 0.40$	—
$\mathcal{B}(K_S^0K^-\pi^+\pi^+)$	$1.64 \pm 0.10 \pm 0.07$	2.7 ± 0.7
$\mathcal{B}(\pi^+\pi^+\pi^-)$	$1.11 \pm 0.07 \pm 0.04$	1.24 ± 0.20
$\mathcal{B}(\pi^+\eta)$	$1.58 \pm 0.11 \pm 0.18$	2.16 ± 0.30
$\mathcal{B}(\pi^+\eta')$	$3.77 \pm 0.25 \pm 0.30$	4.8 ± 0.6
$\mathcal{B}(K^+\pi^+\pi^-)$	$0.69 \pm 0.05 \pm 0.03$	0.67 ± 0.13

Table 7.2: Ratios to the value $\mathcal{B}_{\rm ref} = \mathcal{B}(D_s^+ \to K^-K^+\pi^+)$.

Mode	$\mathcal{B}/\mathcal{B}_{\rm ref}$
$K_S^0K^+$	$0.270 \pm 0.009 \pm 0.008$
$K^-K^+\pi^+$	1
$K^-K^+\pi^+\pi^0$	$1.03 \pm 0.05 \pm 0.08$
$K_S^0K^-\pi^+\pi^+$	$0.298 \pm 0.014 \pm 0.011$
$\pi^+\pi^+\pi^-$	$0.202 \pm 0.011 \pm 0.009$
$\pi^+\eta$	$0.288 \pm 0.018 \pm 0.033$
$\pi^+\eta'$	$0.69 \pm 0.04 \pm 0.06$
$K^+\pi^+\pi^-$	$0.125 \pm 0.009 \pm 0.005$

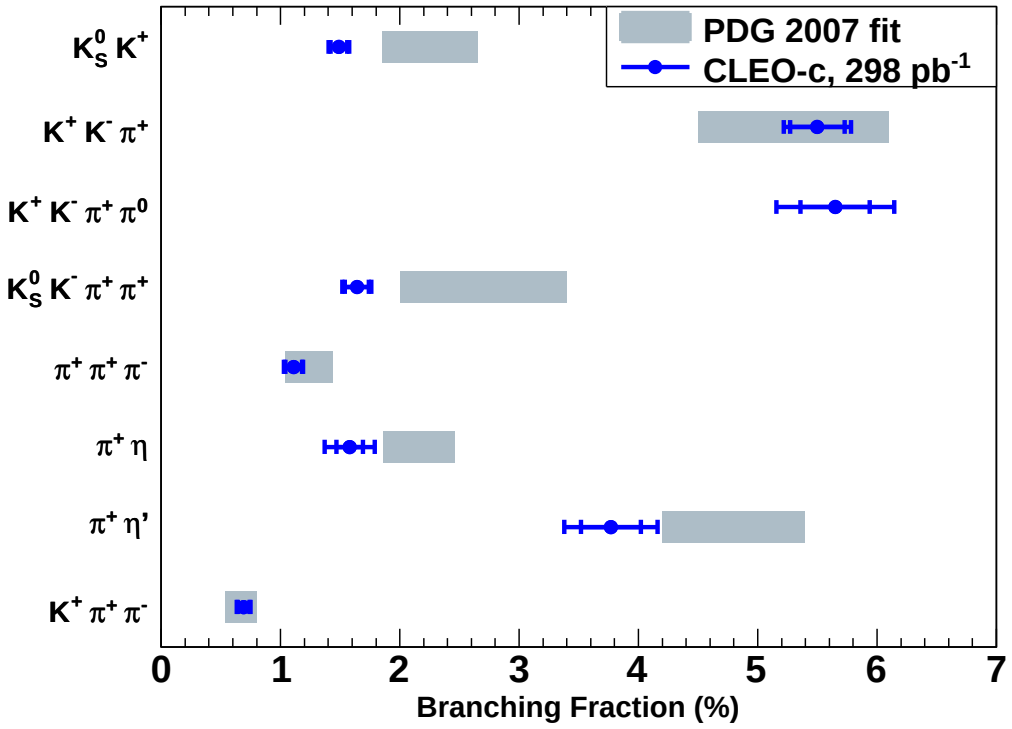

Figure 7.1: Comparison of branching fraction results from this analysis and world averages from the 2007 PDG [19].

Table 7.3: Partial branching fraction of $D_s^+ \to K^-K^+\pi^+$ in four K^-K^+ mass windows. Uncertainties are statistical and systematic, respectively.

K^-K^+ mass window	Partial BF (%)
5 MeV/c^2 ([1.0145 GeV/c^2, 1.0245 GeV/c^2])	1.69 ± 0.08 ± 0.06
10 MeV/c^2 ([1.0095 GeV/c^2, 1.0295 GeV/c^2])	1.99 ± 0.10 ± 0.05
15 MeV/c^2 ([1.0045 GeV/c^2, 1.0345 GeV/c^2])	2.14 ± 0.10 ± 0.05
20 MeV/c^2 ([0.9995 GeV/c^2, 1.0395 GeV/c^2])	2.24 ± 0.11 ± 0.06

Table 7.4: *CP* asymmetries $\mathcal{A}_{CP}$ for the eight modes in this analysis. Uncertainties are statistical and systematic.

Mode	$\mathcal{A}_{CP}$
$K^0_S K^+$	$+0.049 \pm 0.021 \pm 0.009$
$K^- K^+ \pi^+$	$+0.003 \pm 0.011 \pm 0.008$
$K^- K^+ \pi^+ \pi^0$	$-0.059 \pm 0.042 \pm 0.012$
$K^0_S K^- \pi^+ \pi^+$	$-0.007 \pm 0.036 \pm 0.011$
$\pi^+ \pi^+ \pi^-$	$+0.020 \pm 0.046 \pm 0.007$
$\pi^+ \eta$	$-0.082 \pm 0.052 \pm 0.008$
$\pi^+ \eta'$	$-0.055 \pm 0.037 \pm 0.012$
$K^+ \pi^+ \pi^-$	$+0.112 \pm 0.070 \pm 0.009$

tag technique. The result for the reference decay $D_s^+ \to K^- K^+ \pi^+$ is a factor of two more precise than previous world averages. These results will serve to reduce systematic uncertainties in many analyses in charm and bottom physics and beyond.

APPENDIX A

FIGURES

A.1 Multiple Candidate Selection

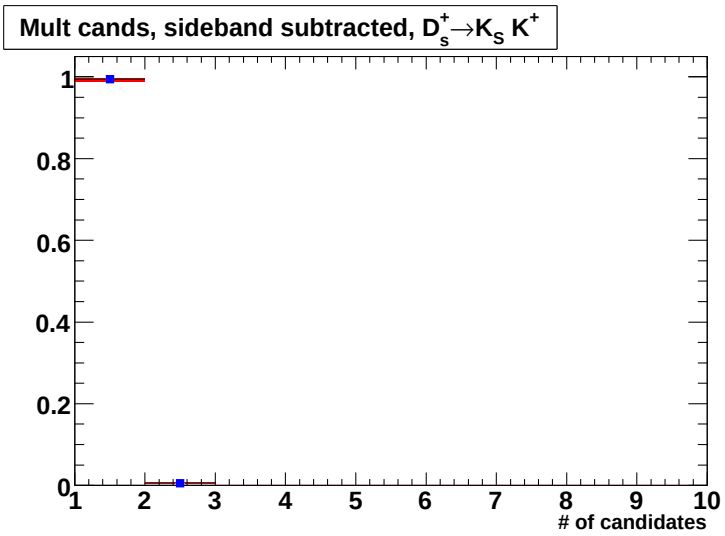

Figure A.1: Background-subtracted multiple candidate rate for $K_S^0 K^+$ mode in MC (red bars) and data (blue points).

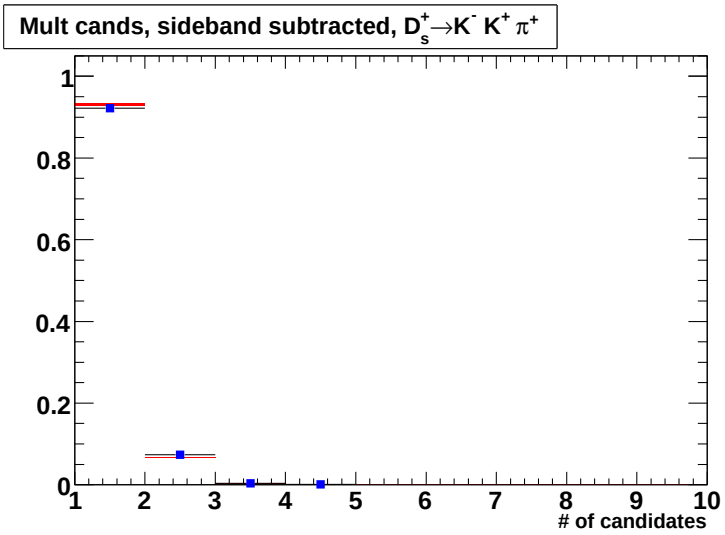

Figure A.2: Background-subtracted multiple candidate rate for $K^-K^+\pi^+$ mode in MC (red bars) and data (blue points).

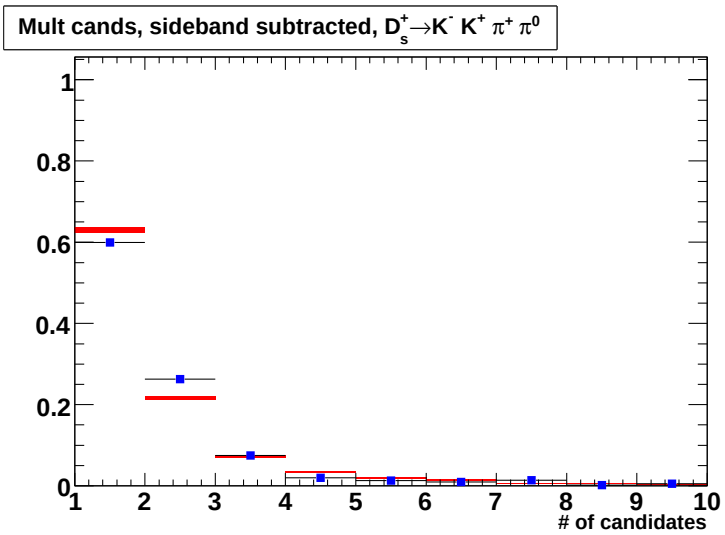

Figure A.3: Background-subtracted multiple candidate rate for $K^-K^+\pi^+\pi^0$ mode in MC (red bars) and data (blue points).

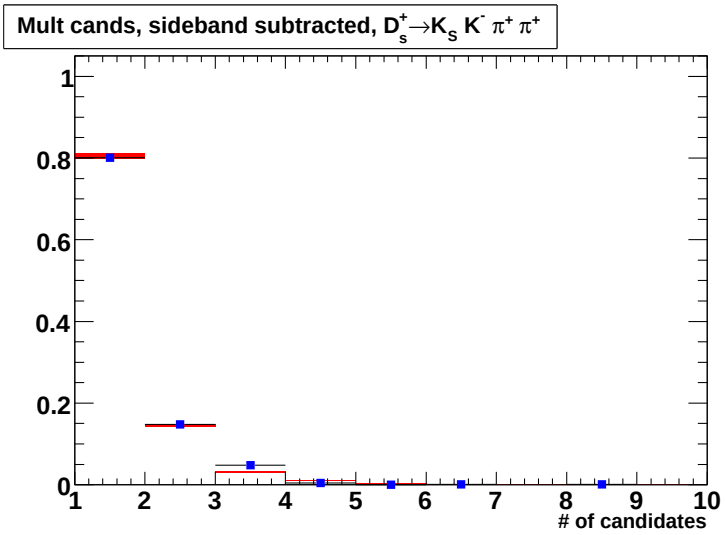

Figure A.4: Background-subtracted multiple candidate rate for $K_S^0 K^- \pi^+ \pi^+$ mode in MC (red bars) and data (blue points).

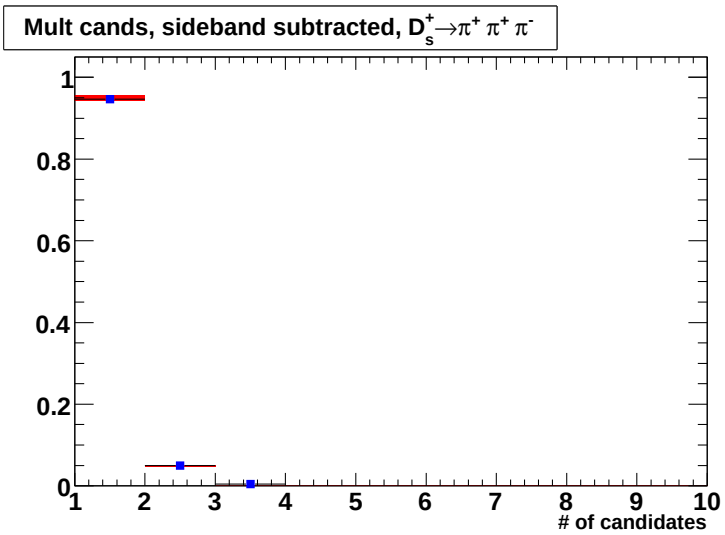

Figure A.5: Background-subtracted multiple candidate rate for the $\pi\pi\pi$ mode in MC (red bars) and data (blue points).

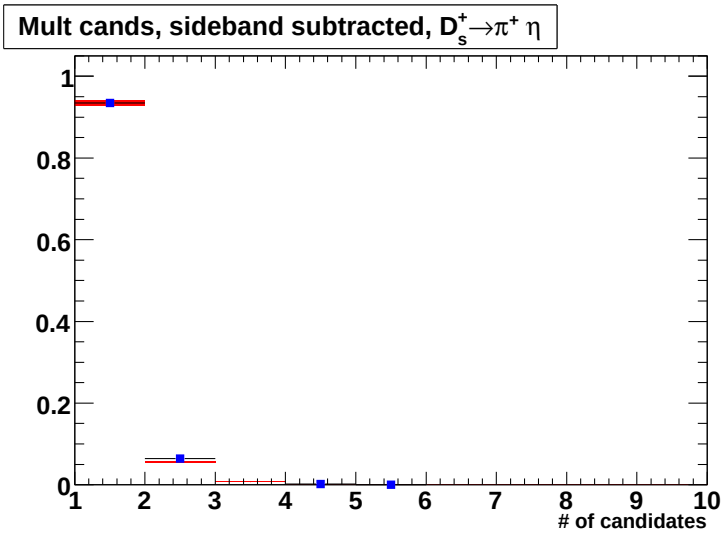

Figure A.6: Background-subtracted multiple candidate rate for the $\pi\eta$ mode in MC (red bars) and data (blue points).

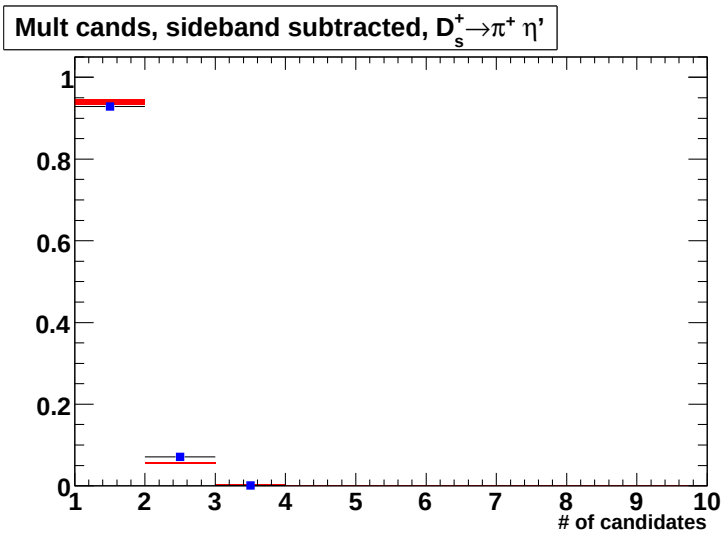

Figure A.7: Background-subtracted multiple candidate rate for the $\pi\eta'$ mode in MC (red bars) and data (blue points).

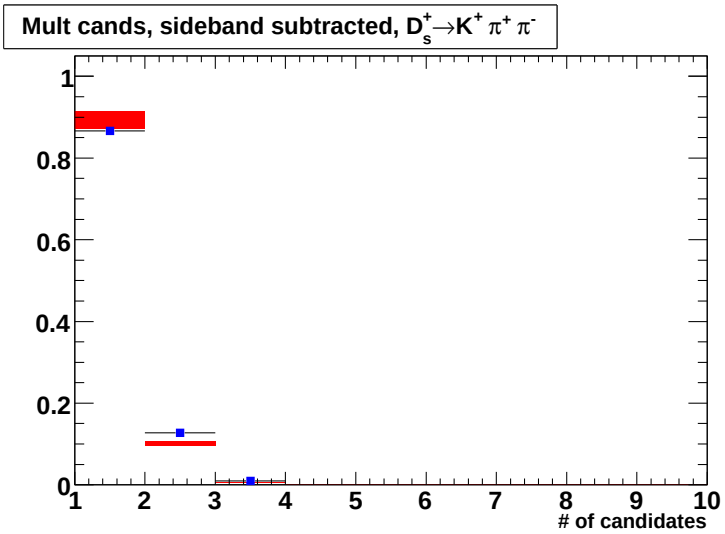

Figure A.8: Background-subtracted multiple candidate rate for the $K^+\pi^+\pi^-$ mode in MC (red bars) and data (blue points).

A.2 Single Tag Efficiency Fits in Signal MC

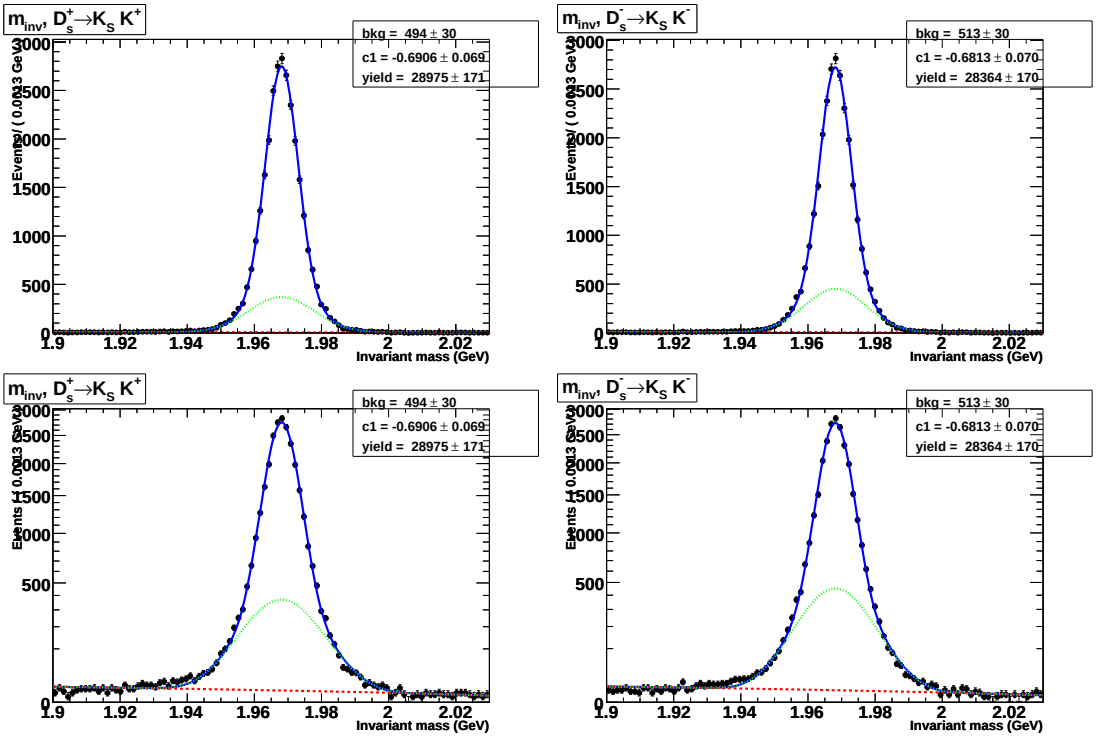

Figure A.9: Signal MC single tag fits for mode $D_s^+ \to K_S^0 K^+$. The blue line is the sum of the background and signal components. The green dotted line is the sum of the background and the wide component of the signal lineshape.

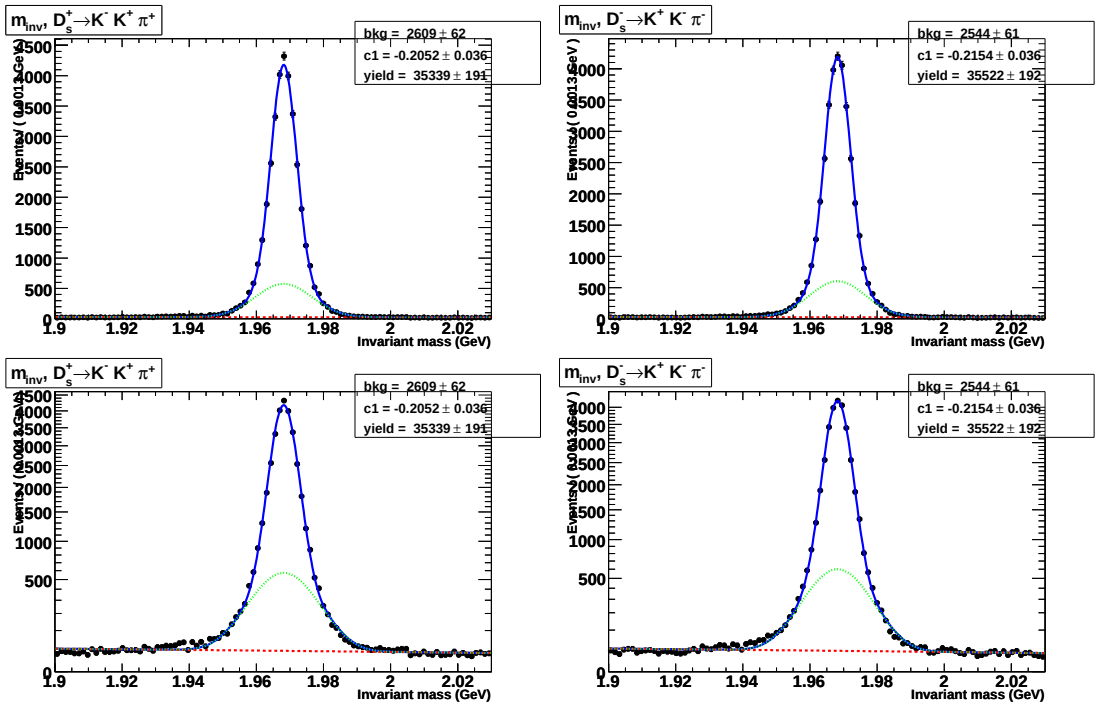

Figure A.10: Signal MC single tag fits for mode $D_s^+ \to K^-K^+\pi^+$. The blue line is the sum of the background and signal components. The green dotted line is the sum of the background and the wide component of the signal lineshape.

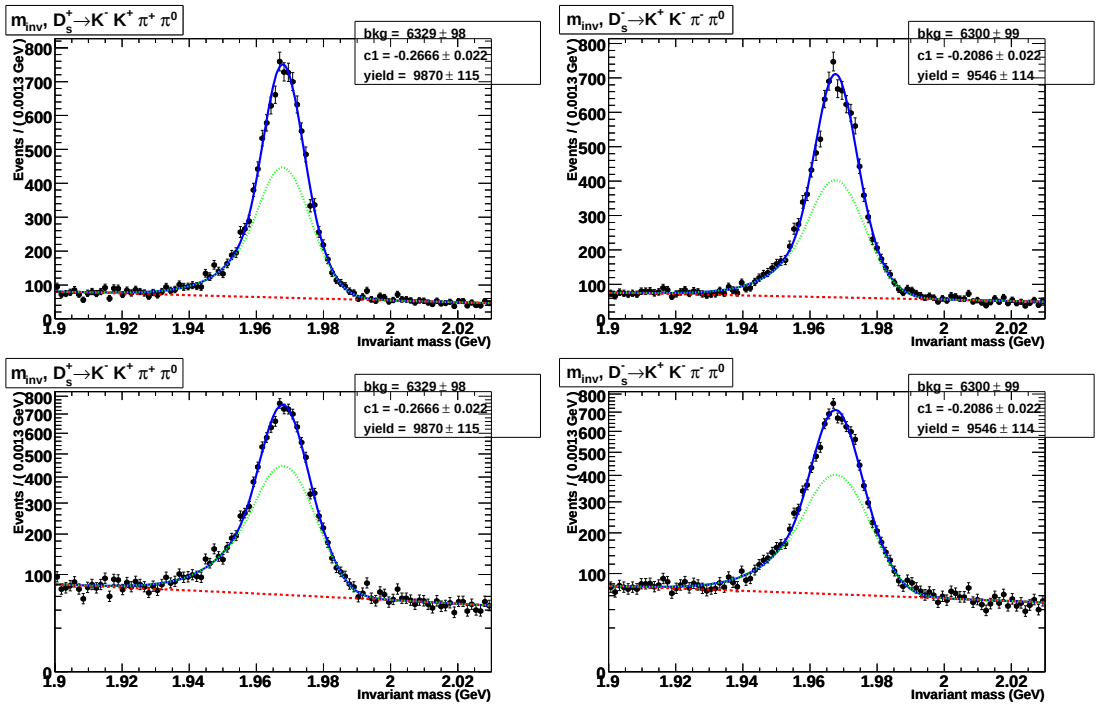

Figure A.11: Signal MC single tag fits for mode $D_s^+ \to K^-K^+\pi^+\pi^0$. The blue line is the sum of the background and signal components. The green dotted line is the sum of the background and the wide component of the signal lineshape.

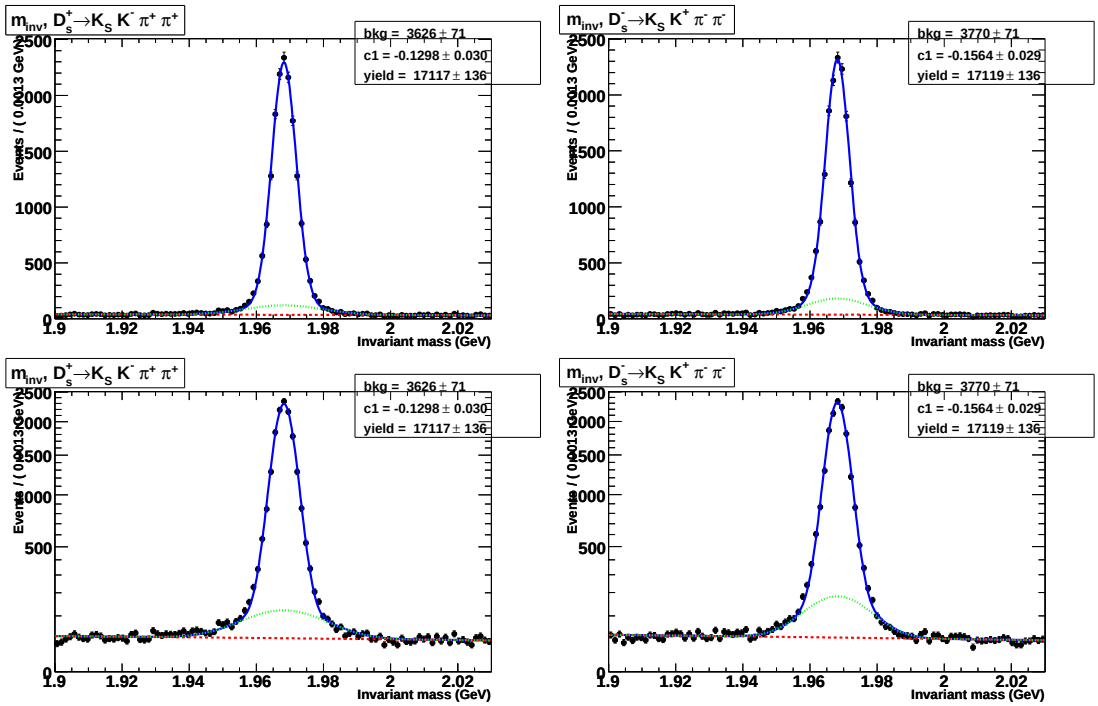

Figure A.12: Signal MC single tag fits for mode $D_s^+ \to K_S^0 K^- \pi^+ \pi^+$. The blue line is the sum of the background and signal components. The green dotted line is the sum of the background and the wide component of the signal lineshape.

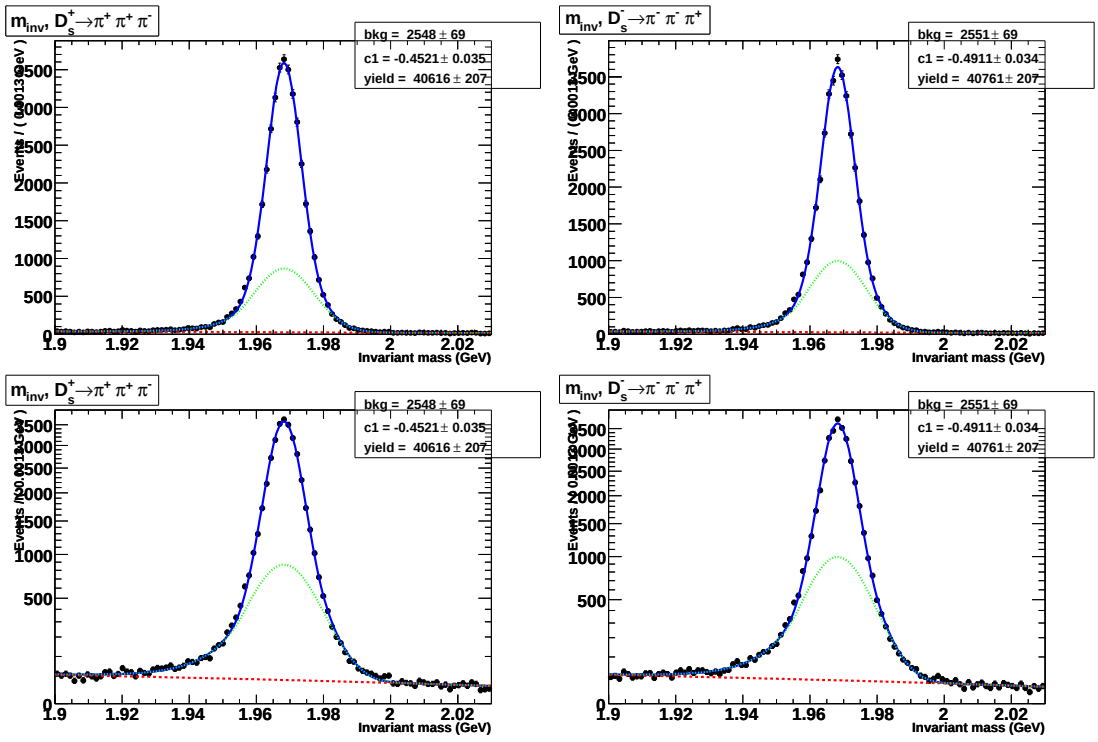

Figure A.13: Signal MC single tag fits for mode $D_s^+ \to \pi^+\pi^+\pi^-$. The blue line is the sum of the background and signal components. The green dotted line is the sum of the background and the wide component of the signal lineshape.

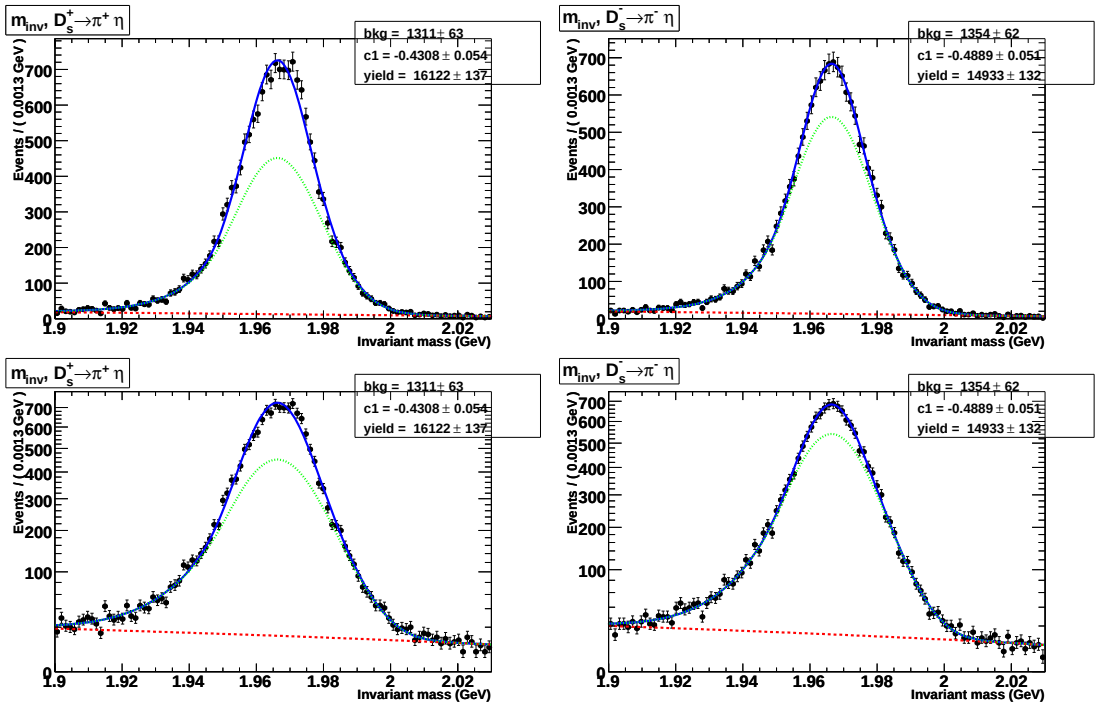

Figure A.14: Signal MC single tag fits for mode $D_s^+ \to \pi^+\eta$. The blue line is the sum of the background and signal components. The green dotted line is the sum of the background and the wide component of the signal lineshape.

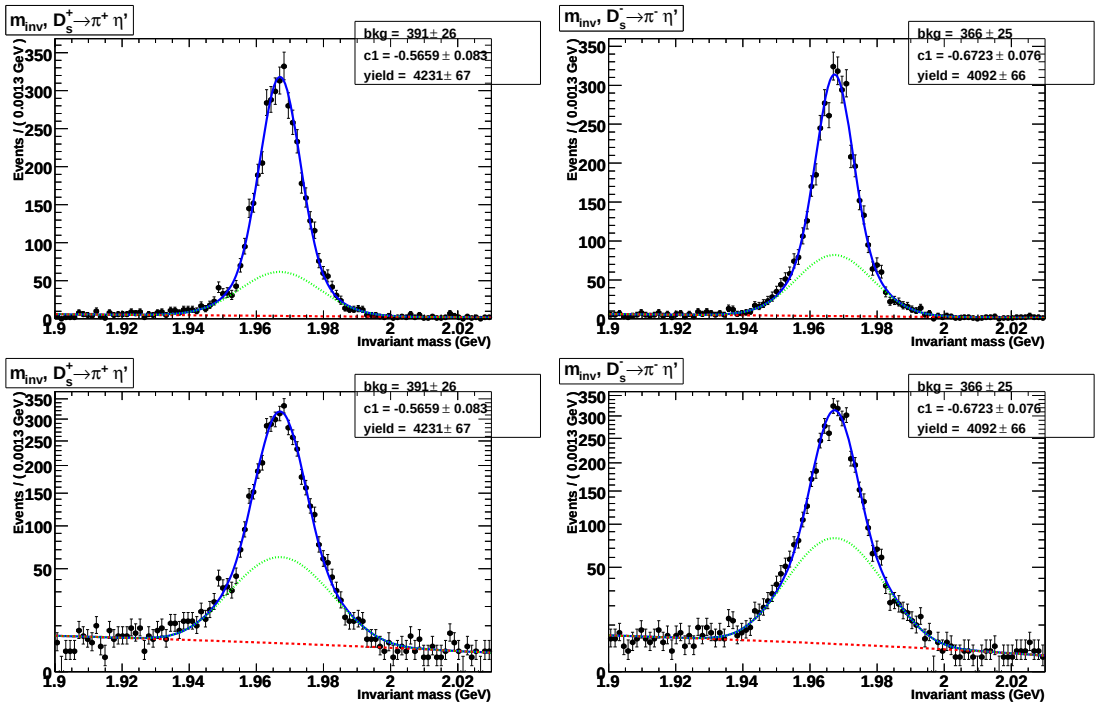

Figure A.15: Signal MC single tag fits for mode $D_s^+ \to \pi^+\eta'$. The blue line is the sum of the background and signal components. The green dotted line is the sum of the background and the wide component of the signal lineshape.

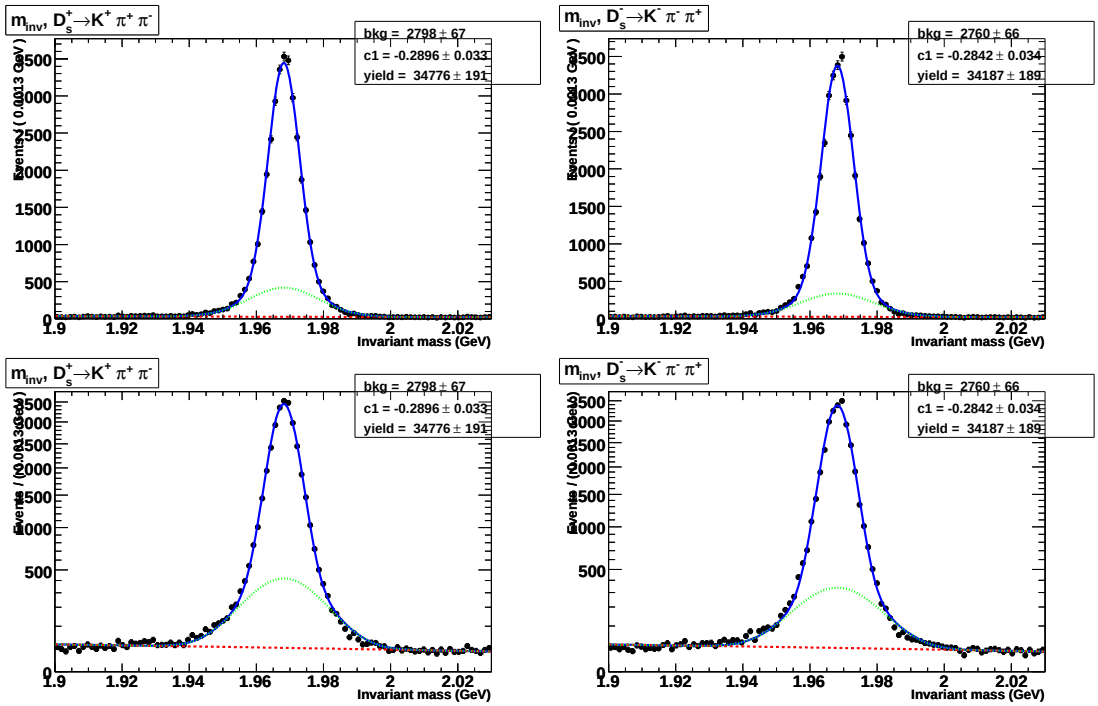

Figure A.16: Signal MC single tag fits for mode $D_s^+ \to K^+\pi^+\pi^-$. The blue line is the sum of the background and signal components. The green dotted line is the sum of the background and the wide component of the signal lineshape.

A.3 Single Tag Yield Fits in Generic MC

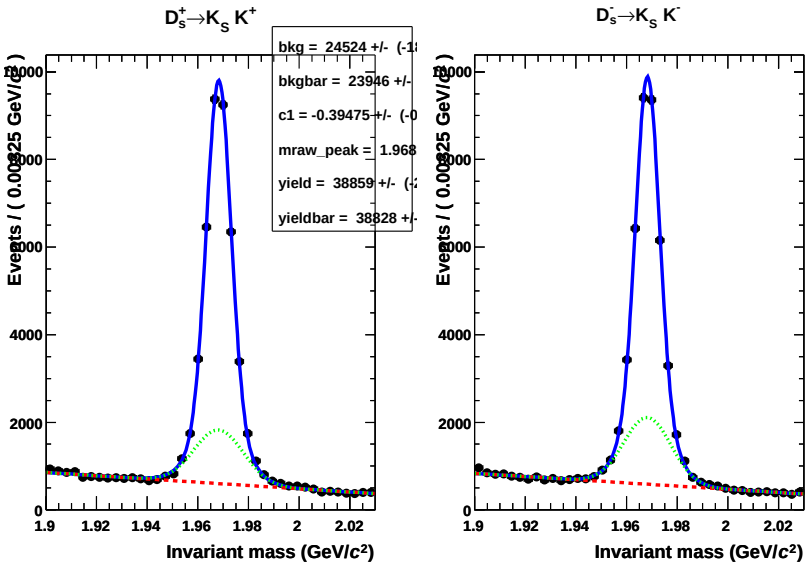

Figure A.17: Generic MC single tag fits for mode $D_s^+ \to K_S^0 K^+$. The blue line is the sum of the background and signal components. The green dotted line is the sum of the background and the wide component of the signal lineshape.

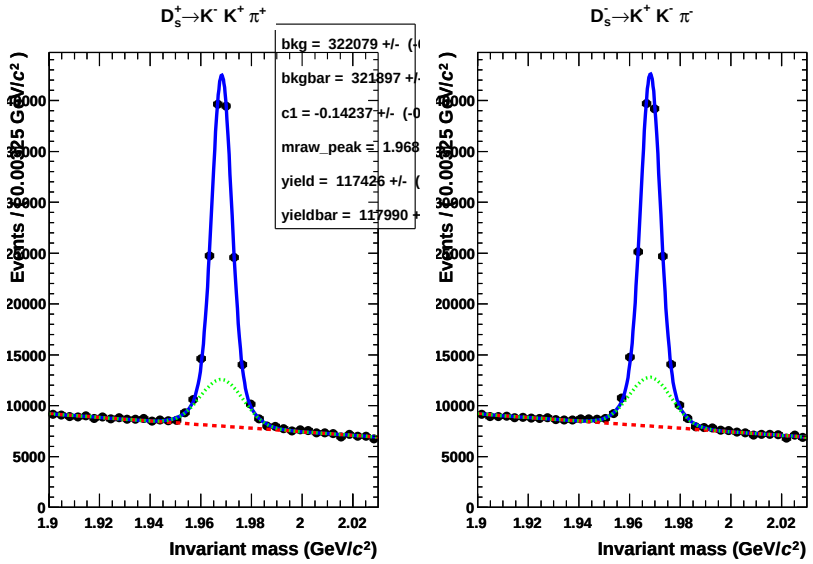

Figure A.18: Generic MC single tag fits for mode $D_s^+ \to K^- K^+ \pi^+$. The blue line is the sum of the background and signal components. The green dotted line is the sum of the background and the wide component of the signal lineshape.

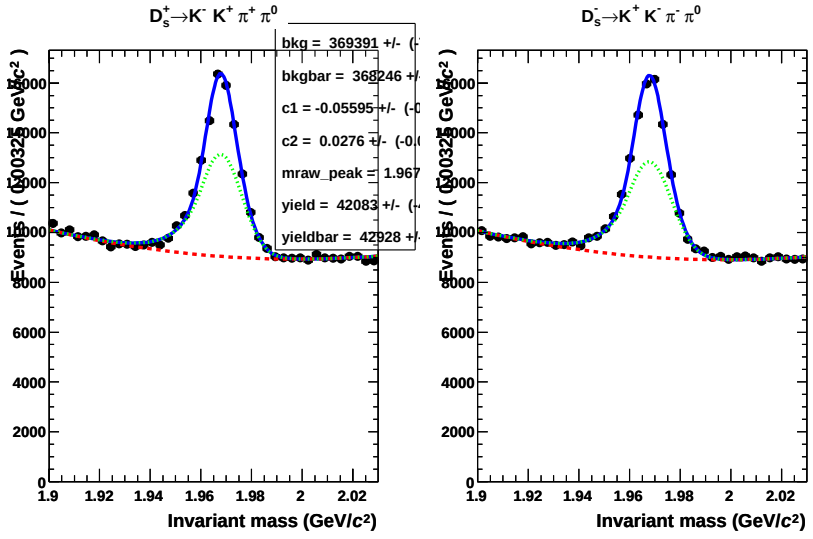

Figure A.19: Generic MC single tag fits for mode $D_s^+ \to K^- K^+ \pi^+ \pi^0$. The blue line is the sum of the background and signal components. The green dotted line is the sum of the background and the wide component of the signal lineshape.

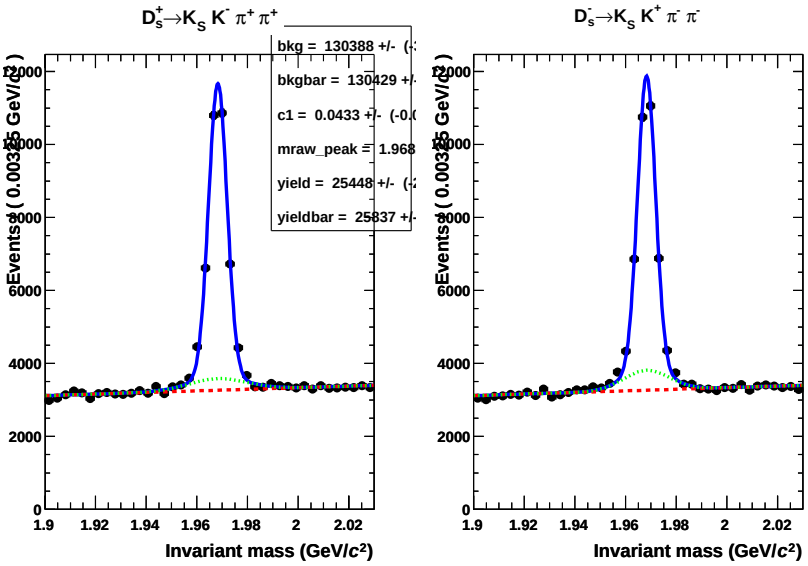

Figure A.20: Generic MC single tag fits for mode $D_s^+ \to K_S^0 K^- \pi^+ \pi^+$. The blue line is the sum of the background and signal components. The green dotted line is the sum of the background and the wide component of the signal lineshape.

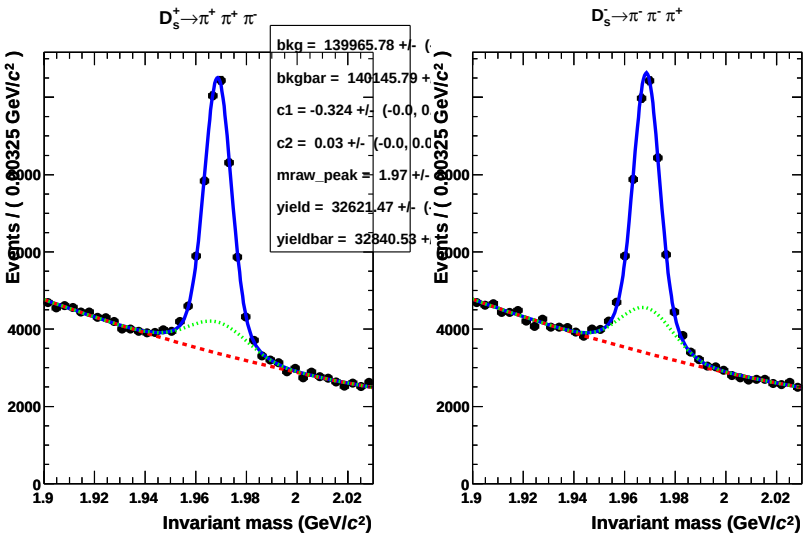

Figure A.21: Generic MC single tag fits for mode $D_s^+ \to \pi^+ \pi^+ \pi^-$. The blue line is the sum of the background and signal components. The green dotted line is the sum of the background and the wide component of the signal lineshape.

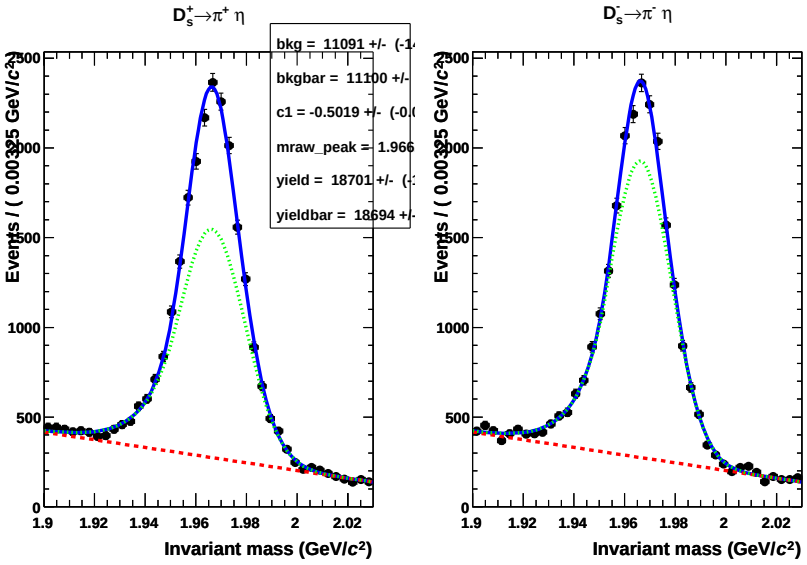

Figure A.22: Generic MC single tag fits for mode $D_s^+ \to \pi^+\eta$. The blue line is the sum of the background and signal components. The green dotted line is the sum of the background and the wide component of the signal lineshape.

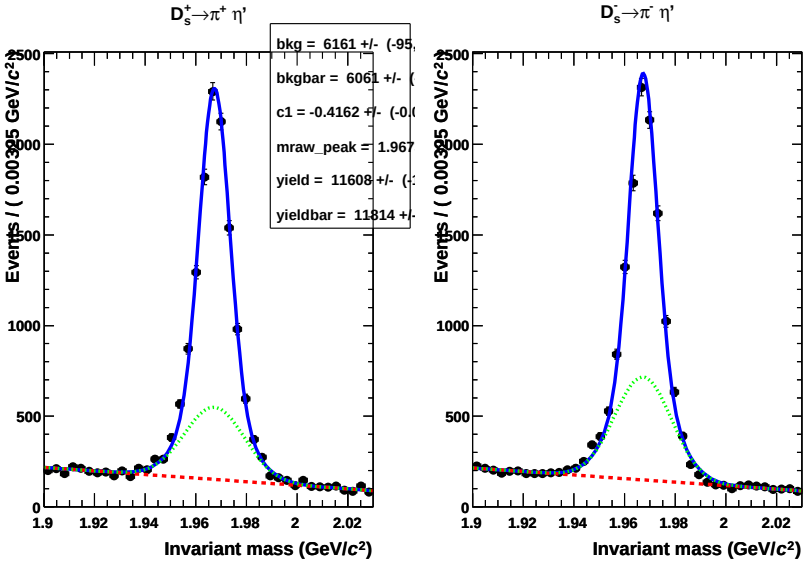

Figure A.23: Generic MC single tag fits for mode $D_s^+ \to \pi^+\eta'$. The blue line is the sum of the background and signal components. The green dotted line is the sum of the background and the wide component of the signal lineshape.

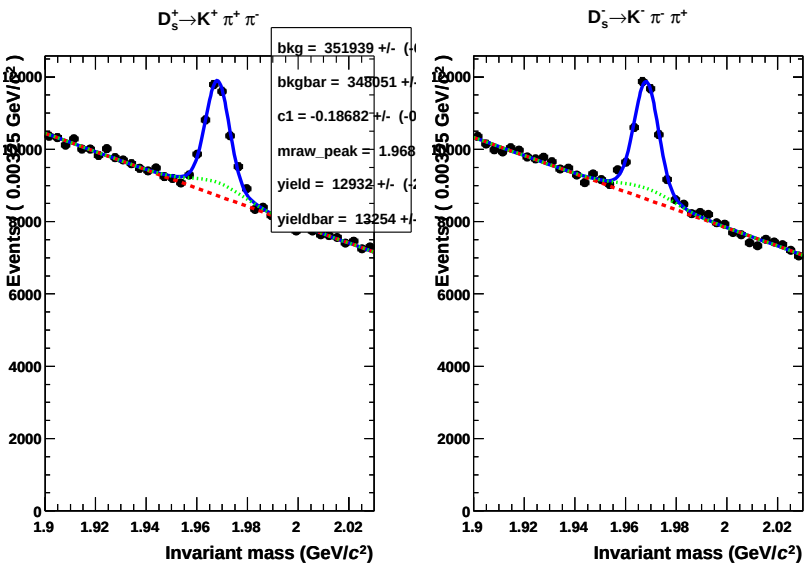

Figure A.24: Generic MC single tag fits for mode $D_s^+ \to K^+\pi^+\pi^-$. The blue line is the sum of the background and signal components. The green dotted line is the sum of the background and the wide component of the signal lineshape.

A.4 Single Tag Yield Fits in Data

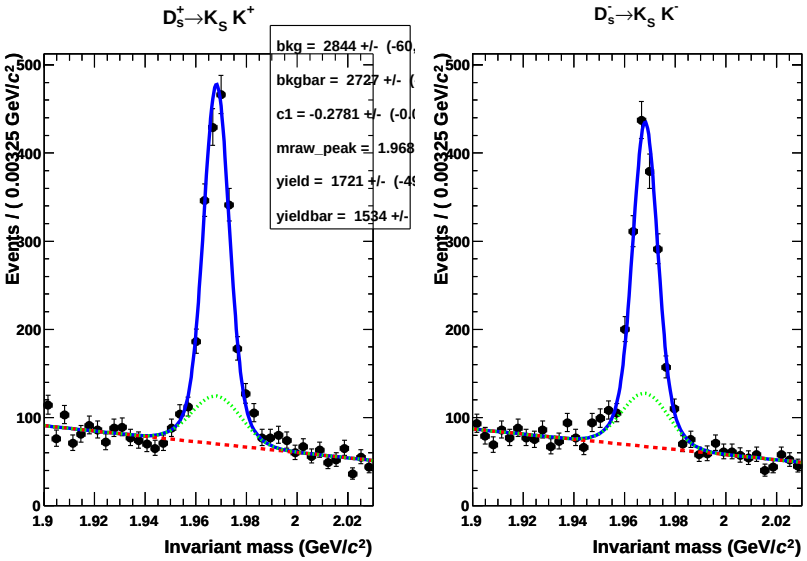

Figure A.25: Data single tag fits for mode $D_s^+ \to K_S^0 K^+$. The blue line is the sum of the background and signal components. The green dotted line is the sum of the background and the wide component of the signal lineshape.

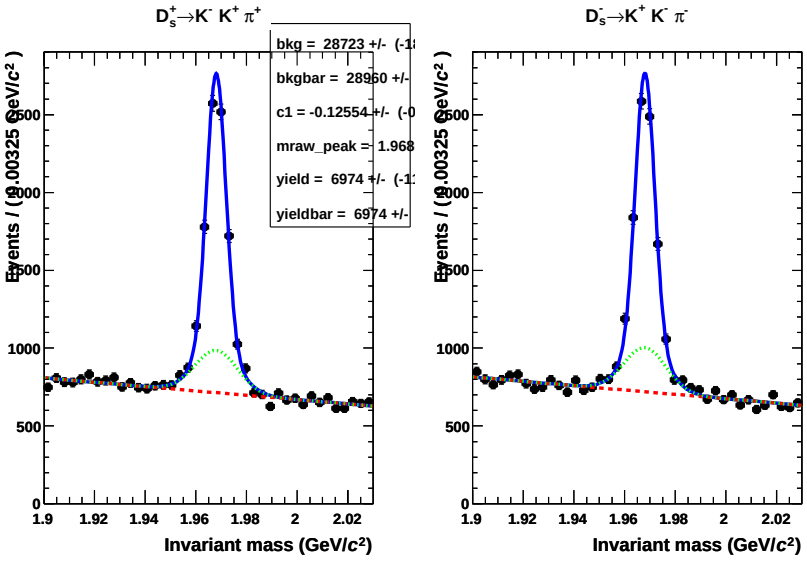

Figure A.26: Data single tag fits for mode $D_s^+ \to K^- K^+ \pi^+$. The blue line is the sum of the background and signal components. The green dotted line is the sum of the background and the wide component of the signal lineshape.

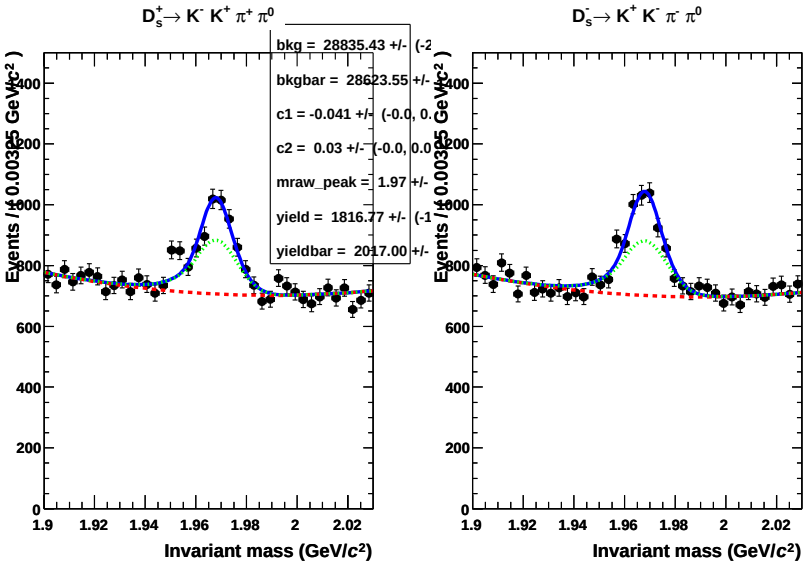

Figure A.27: Data single tag fits for mode $D_s^+ \to K^- K^+ \pi^+ \pi^0$. The blue line is the sum of the background and signal components. The green dotted line is the sum of the background and the wide component of the signal lineshape.

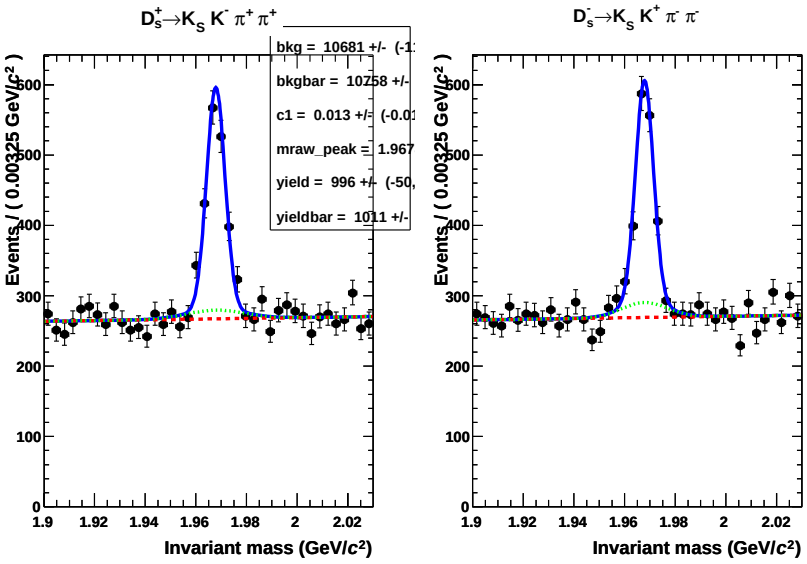

Figure A.28: Data single tag fits for mode $D_s^+ \to K_S^0 K^- \pi^+ \pi^+$. The blue line is the sum of the background and signal components. The green dotted line is the sum of the background and the wide component of the signal lineshape.

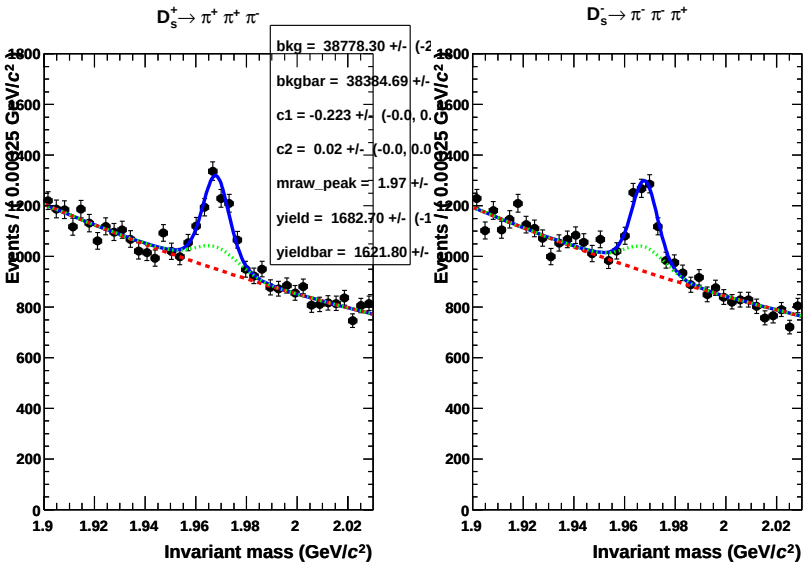

Figure A.29: Data single tag fits for mode $D_s^+ \to \pi^+ \pi^+ \pi^-$. The blue line is the sum of the background and signal components. The green dotted line is the sum of the background and the wide component of the signal lineshape.

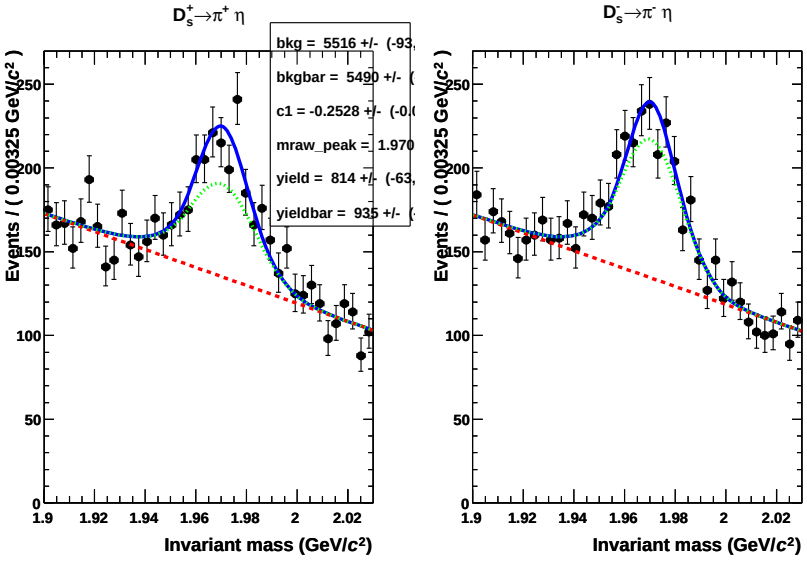

Figure A.30: Data single tag fits for mode $D_s^+ \to \pi^+\eta$. The blue line is the sum of the background and signal components. The green dotted line is the sum of the background and the wide component of the signal lineshape.

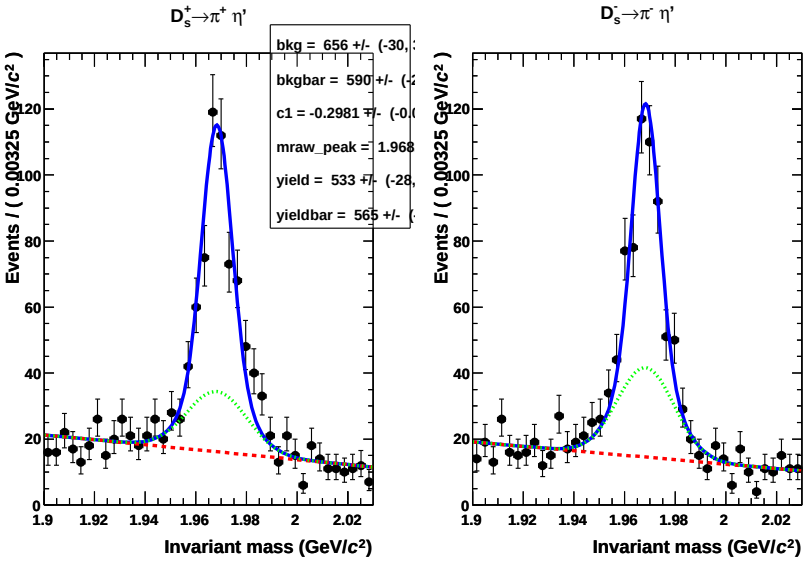

Figure A.31: Data single tag fits for mode $D_s^+ \to \pi^+\eta'$. The blue line is the sum of the background and signal components. The green dotted line is the sum of the background and the wide component of the signal lineshape.

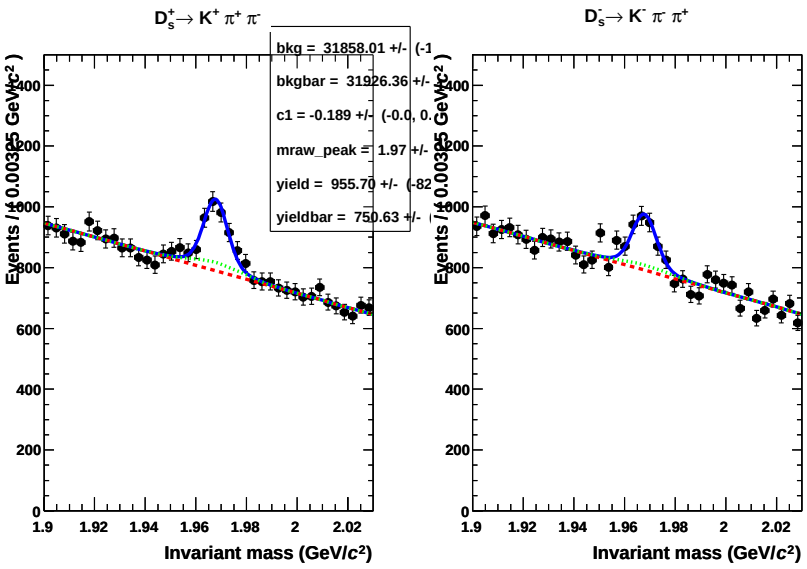

Figure A.32: Data single tag fits for mode $D_s^+ \to K^+\pi^+\pi^-$. The blue line is the sum of the background and signal components. The green dotted line is the sum of the background and the wide component of the signal lineshape.

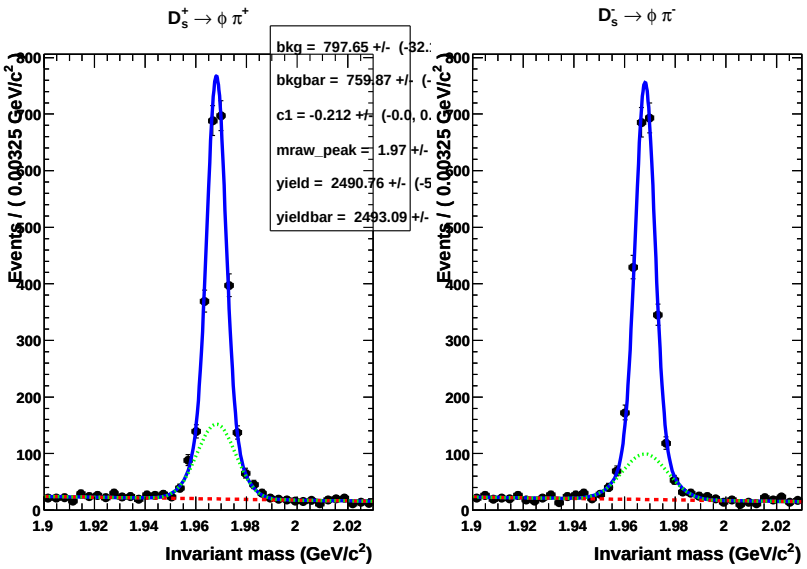

Figure A.33: Data single tag fits for mode $D_s^+ \to \phi\pi^+ \to K^-K^+\pi^+$ (10 MeV KK mass cut). The blue line is the sum of the background and signal components. The green dotted line is the sum of the background and the wide component of the signal lineshape.

A.5 Double Tag Efficiency in Signal MC

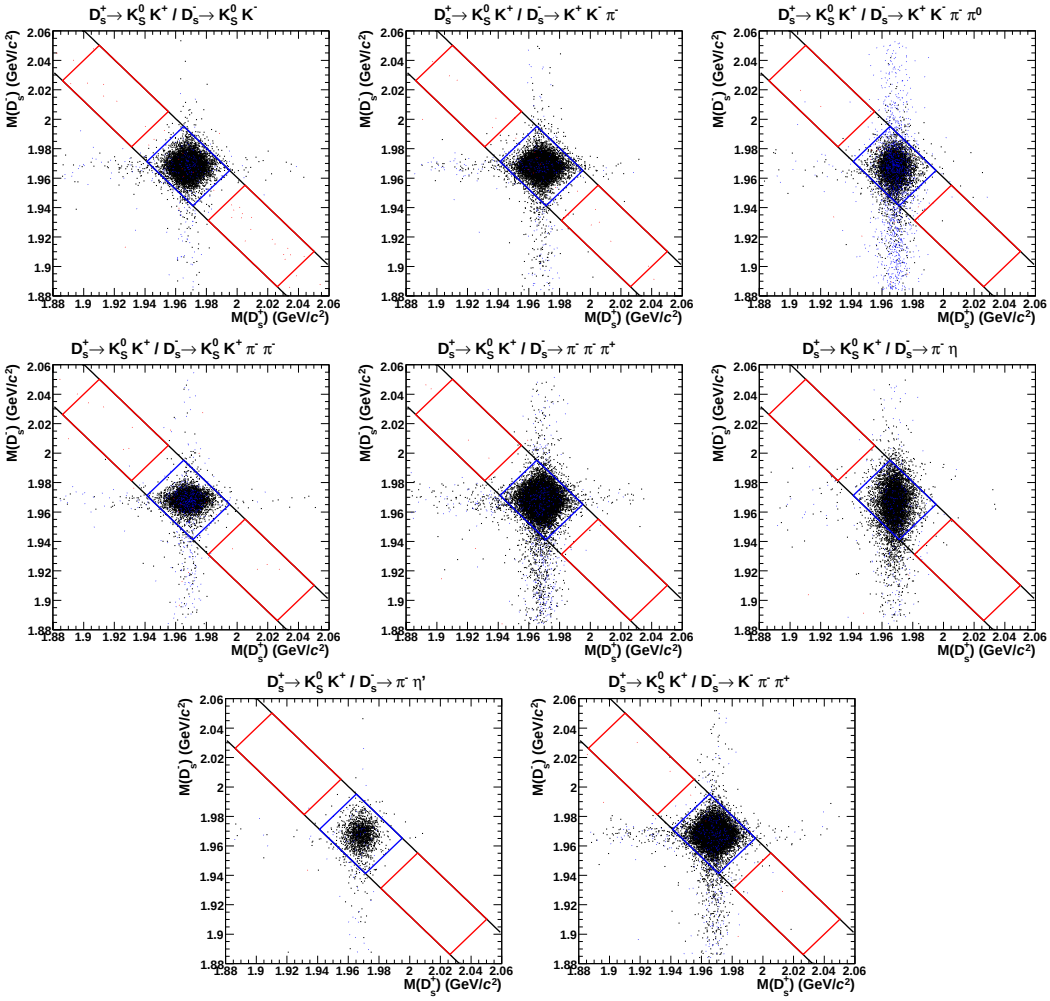

Figure A.34: Signal MC plots of $M_{\rm inv}(D_s^+)$ vs. $M_{\rm inv}(D_s^-)$ in double tag candidates for: (top left) $D_s^+ \to K_S^0 K^+ / D_s^- \to K_S^0 K^-$; (top center) $D_s^+ \to K_S^0 K^+ / D_s^- \to K^+ K^- \pi^-$; (top right) $D_s^+ \to K_S^0 K^+ / D_s^- \to K^+ K^- \pi^- \pi^0$; (middle left) $D_s^- \to K_S^0 K^- \pi^+ \pi^+$; (middle center) $D_s^+ \to K_S^0 K^+ / D_s^- \to \pi^- \pi^- \pi^+$; (middle right) $D_s^+ \to K_S^0 K^+ / D_s^- \to \pi^- \eta$; (bottom left) $D_s^+ \to K_S^0 K^+ / D_s^- \to \pi^- \eta'$; (bottom right) $D_s^+ \to K_S^0 K^+ / D_s^- \to K^+ \pi^+ \pi^-$. Black, blue, and red points correspond to two, one, or zero MC matched D_s candidates, respectively.

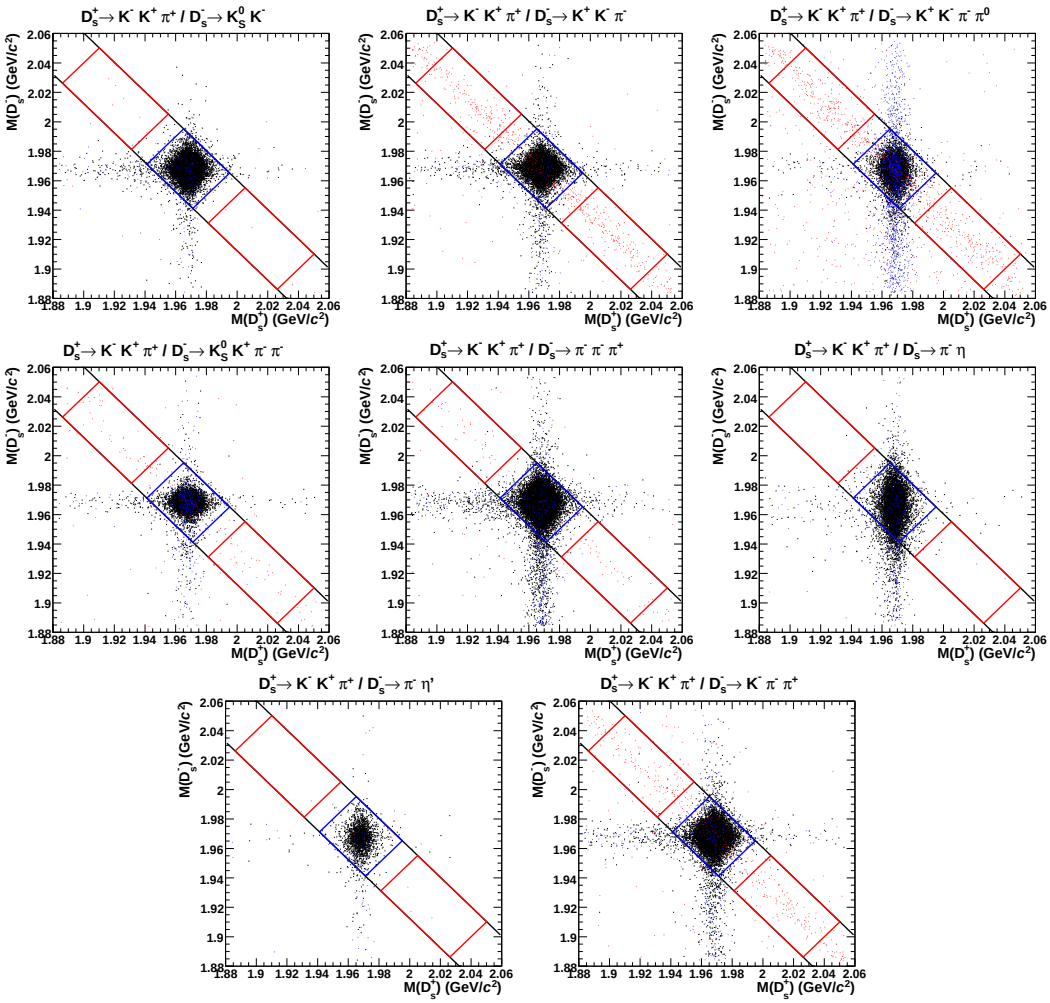

Figure A.35: Signal MC plots of $M_{\text{inv}}(D_s^+)$ vs. $M_{\text{inv}}(D_s^-)$ in double tag candidates for: (top left) $D_s^+ \to K^-K^+\pi^+/D_s^- \to K_S^0K^-$; (top center) $D_s^+ \to K^-K^+\pi^+ /D_s^- \to K^+K^-\pi^-$; (top right) $D_s^+ \to K^-K^+\pi^+/D_s^- \to K^+K^-\pi^-\pi^0$; (middle left) $D_s^- \to K_S^0K^-\pi^+\pi^+$; (middle center) $D_s^+ \to K^-K^+\pi^+/D_s^- \to \pi^-\pi^-\pi^+$; (middle right) $D_s^+ \to K^-K^+\pi^+/D_s^- \to \pi^-\eta$; (bottom left) $D_s^+ \to K^-K^+\pi^+/D_s^- \to \pi^-\eta'$; (bottom right) $D_s^+ \to K^-K^+\pi^+/D_s^- \to K^+\pi^+\pi^-$. Black, blue, and red points correspond to two, one, or zero MC matched D_s candidates, respectively.

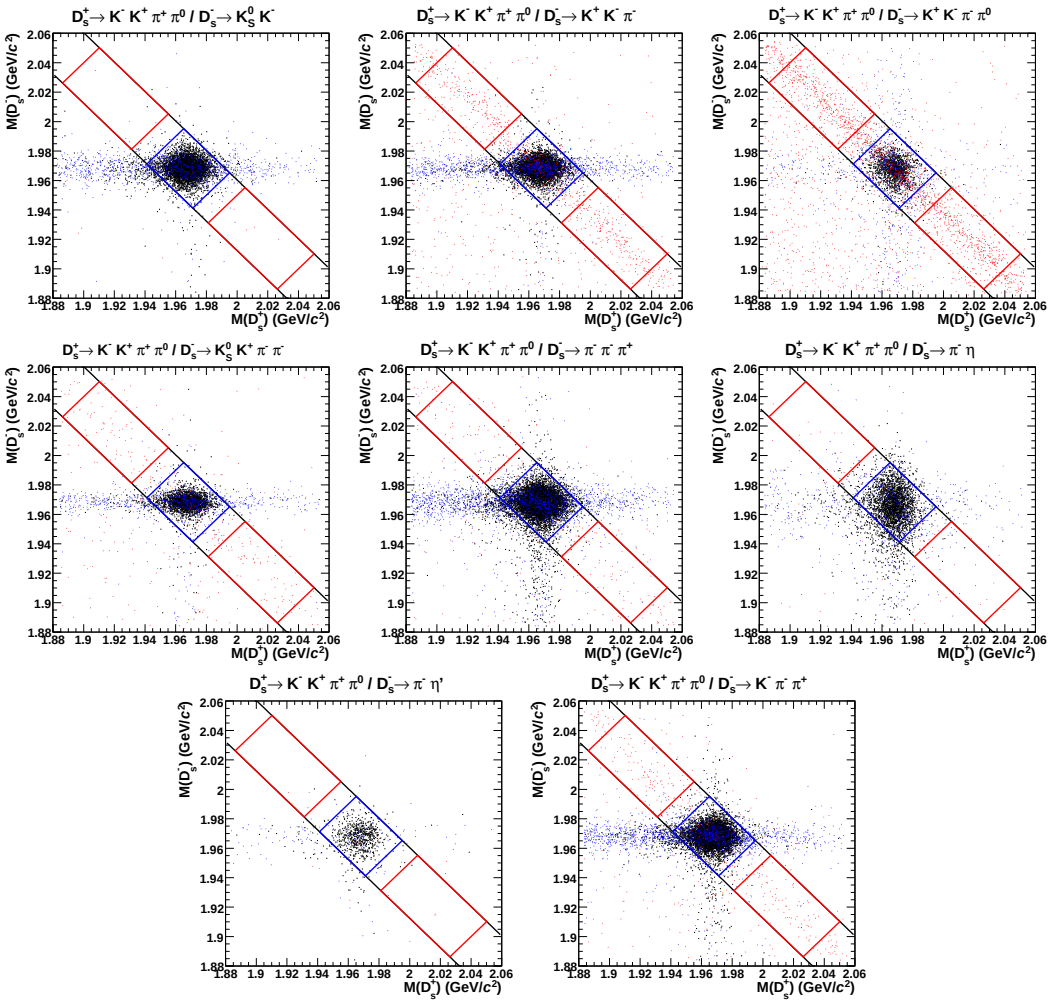

Figure A.36: Signal MC plots of $M_{\rm inv}(D_s^+)$ vs. $M_{\rm inv}(D_s^-)$ in double tag candidates for: (top left) $D_s^+ \to K^-K^+\pi^+\pi^0/D_s^- \to K_S^0K^-$; (top center) $D_s^+ \to K^-K^+\pi^+\pi^0\ /D_s^- \to K^+K^-\pi^-$; (top right) $D_s^+ \to K^-K^+\pi^+\pi^0/D_s^- \to K^+K^-\pi^-\pi^0$; (middle left) $D_s^- \to K_S^0K^-\pi^+\pi^+$; (middle center) $D_s^+ \to K^-K^+\pi^+\pi^0/D_s^- \to \pi^-\pi^-\pi^+$; (middle right) $D_s^+ \to K^-K^+\pi^+\pi^0/D_s^- \to \pi^-\eta$; (bottom left) $D_s^+ \to K^-K^+\pi^+\pi^0/D_s^- \to \pi^-\eta'$; (bottom right) $D_s^+ \to K^-K^+\pi^+\pi^0/D_s^- \to K^+\pi^+\pi^-$. Black, blue, and red points correspond to two, one, or zero MC matched D_s candidates, respectively.

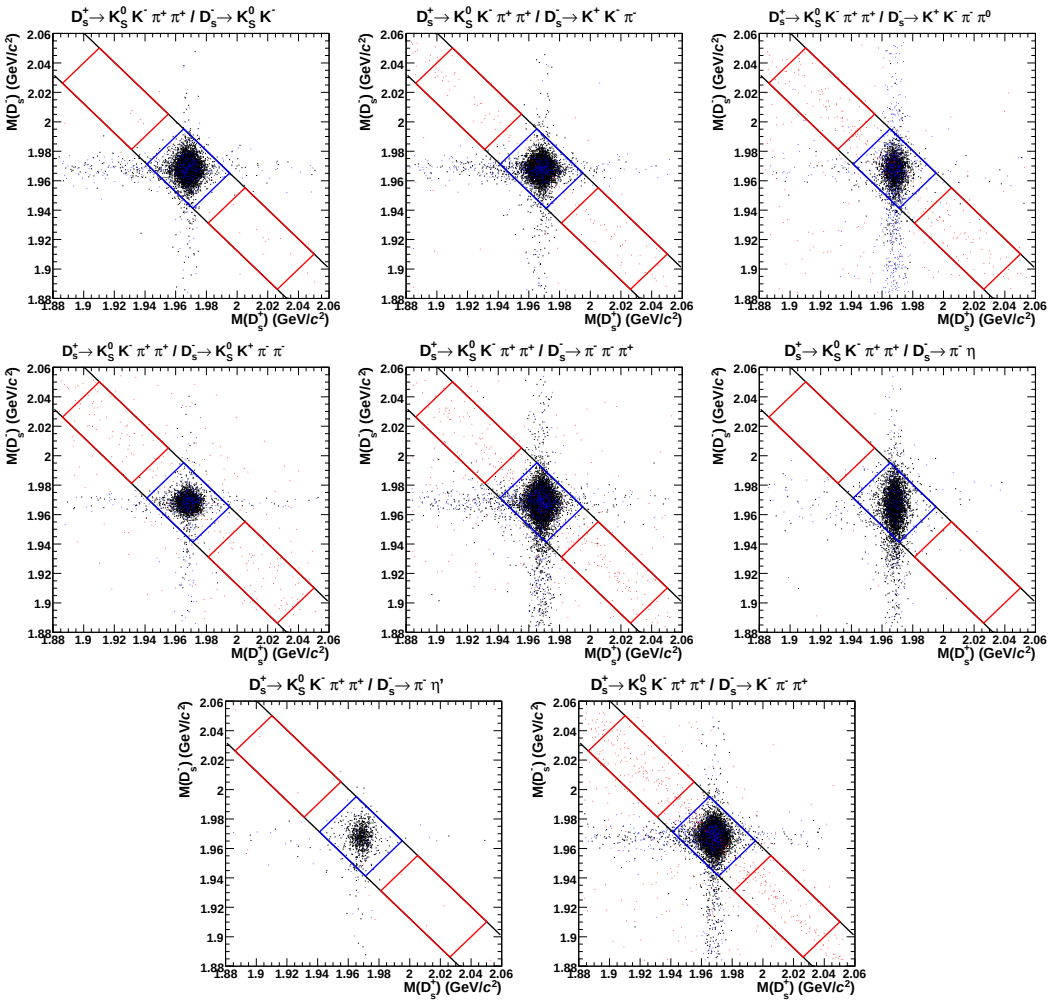

Figure A.37: Signal MC plots of $M_{\text{inv}}(D_s^+)$ vs. $M_{\text{inv}}(D_s^-)$ in double tag candidates for: (top left) $D_s^+ \to K_S^0 K^- \pi^+ \pi^+ / D_s^- \to K_S^0 K^-$; (top center) $D_s^+ \to K_S^0 K^- \pi^+ \pi^+ / D_s^- \to K^+ K^- \pi^-$; (top right) $D_s^+ \to K_S^0 K^- \pi^+ \pi^+ / D_s^- \to K^+ K^- \pi^- \pi^0$; (middle left) $D_s^- \to K_S^0 K^- \pi^+ \pi^+$; (middle center) $D_s^+ \to K_S^0 K^- \pi^+ \pi^+ / D_s^- \to \pi^- \pi^- \pi^+$; (middle right) $D_s^+ \to K_S^0 K^- \pi^+ \pi^+ / D_s^- \to \pi^- \eta$; (bottom left) $D_s^+ \to K_S^0 K^- \pi^+ \pi^+ / D_s^- \to \pi^- \eta'$; (bottom right) $D_s^+ \to K_S^0 K^- \pi^+ \pi^+ / D_s^- \to K^+ \pi^+ \pi^-$. Black, blue, and red points correspond to two, one, or zero MC matched D_s candidates, respectively.

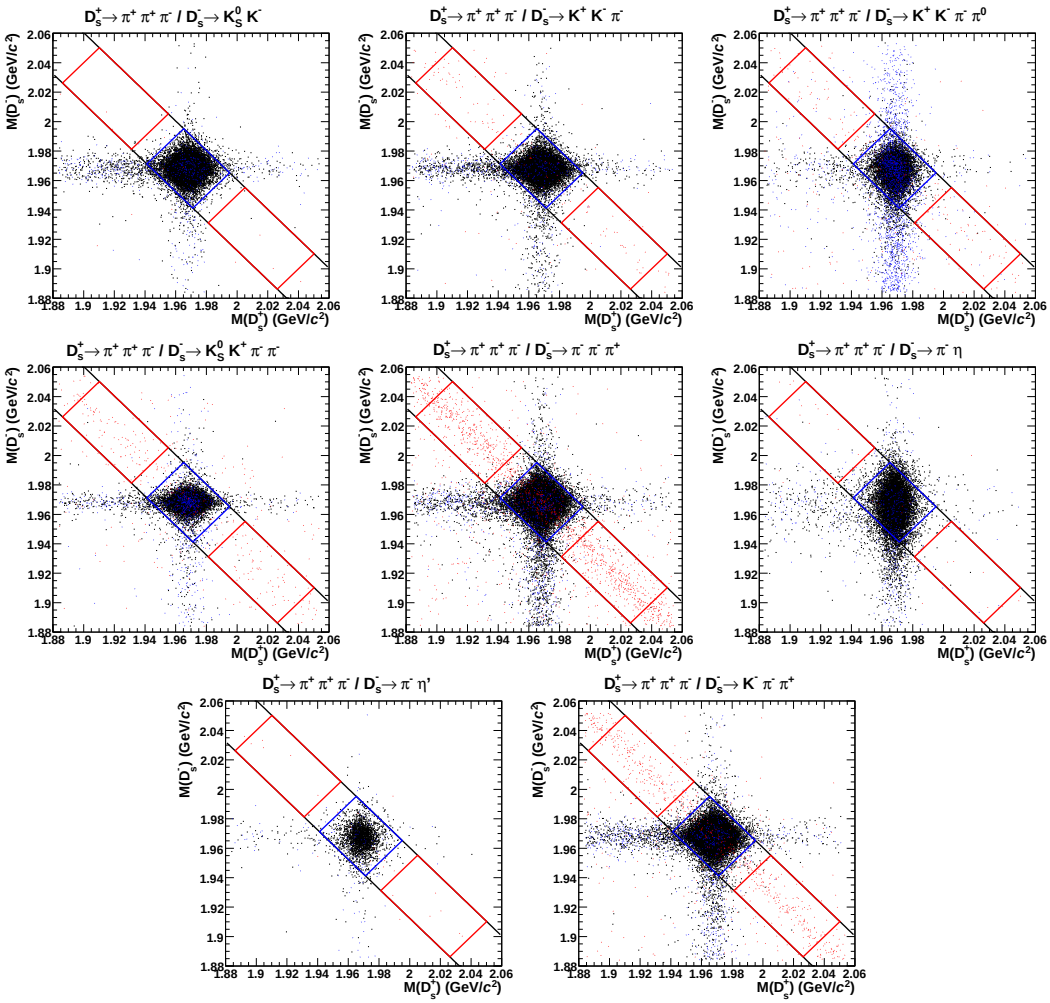

Figure A.38: Signal MC plots of $M_{\rm inv}(D_s^+)$ vs. $M_{\rm inv}(D_s^-)$ in double tag candidates for: (top left) $D_s^+ \to \pi^+\pi^+\pi^-/D_s^- \to K_S^0 K^-$; (top center) $D_s^+ \to \pi^+\pi^+\pi^- /D_s^- \to K^+K^-\pi^-$; (top right) $D_s^+ \to \pi^+\pi^+\pi^-/D_s^- \to K^+K^-\pi^-\pi^0$; (middle left) $D_s^- \to K_S^0 K^-\pi^+\pi^+$; (middle center) $D_s^+ \to \pi^+\pi^+\pi^-/D_s^- \to \pi^-\pi^-\pi^+$; (middle right) $D_s^+ \to \pi^+\pi^+\pi^-/D_s^- \to \pi^-\eta$; (bottom left) $D_s^+ \to \pi^+\pi^+\pi^-/D_s^- \to \pi^-\eta'$; (bottom right) $D_s^+ \to \pi^+\pi^+\pi^-/D_s^- \to K^+\pi^+\pi^-$. Black, blue, and red points correspond to two, one, or zero MC matched D_s candidates, respectively.

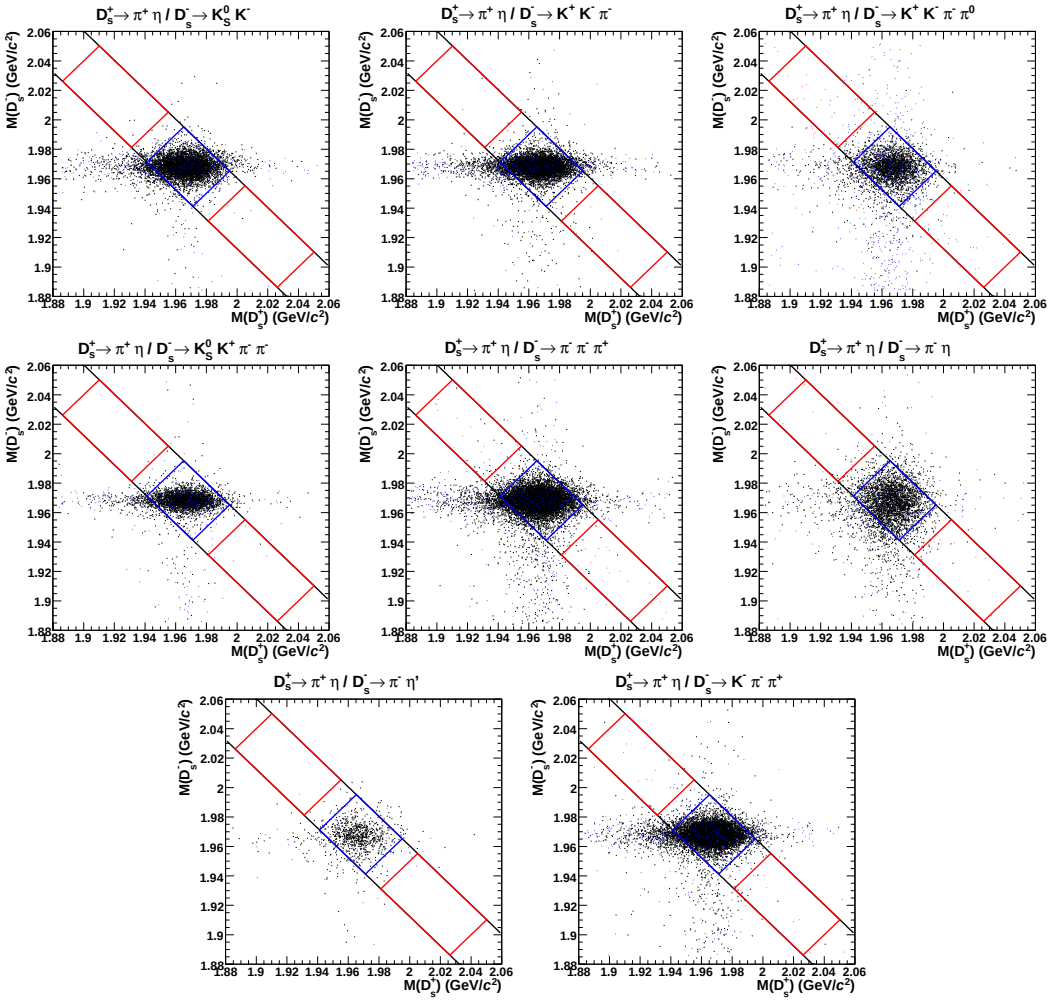

Figure A.39: Signal MC plots of $M_{\text{inv}}(D_s^+)$ vs. $M_{\text{inv}}(D_s^-)$ in double tag candidates for: (top left) $D_s^+ \to \pi^+\eta / D_s^- \to K_S^0 K^-$; (top center) $D_s^+ \to \pi^+\eta$ $/D_s^- \to K^+K^-\pi^-$; (top right) $D_s^+ \to \pi^+\eta / D_s^- \to K^+K^-\pi^-\pi^0$; (middle left) $D_s^- \to K_S^0 K^-\pi^+\pi^+$; (middle center) $D_s^+ \to \pi^+\eta / D_s^- \to \pi^-\pi^-\pi^+$; (middle right) $D_s^+ \to \pi^+\eta / D_s^- \to \pi^-\eta$; (bottom left) $D_s^+ \to \pi^+\eta / D_s^- \to \pi^-\eta'$; (bottom right) $D_s^+ \to \pi^+\eta / D_s^- \to K^+\pi^+\pi^-$. Black, blue, and red points correspond to two, one, or zero MC matched D_s candidates, respectively.

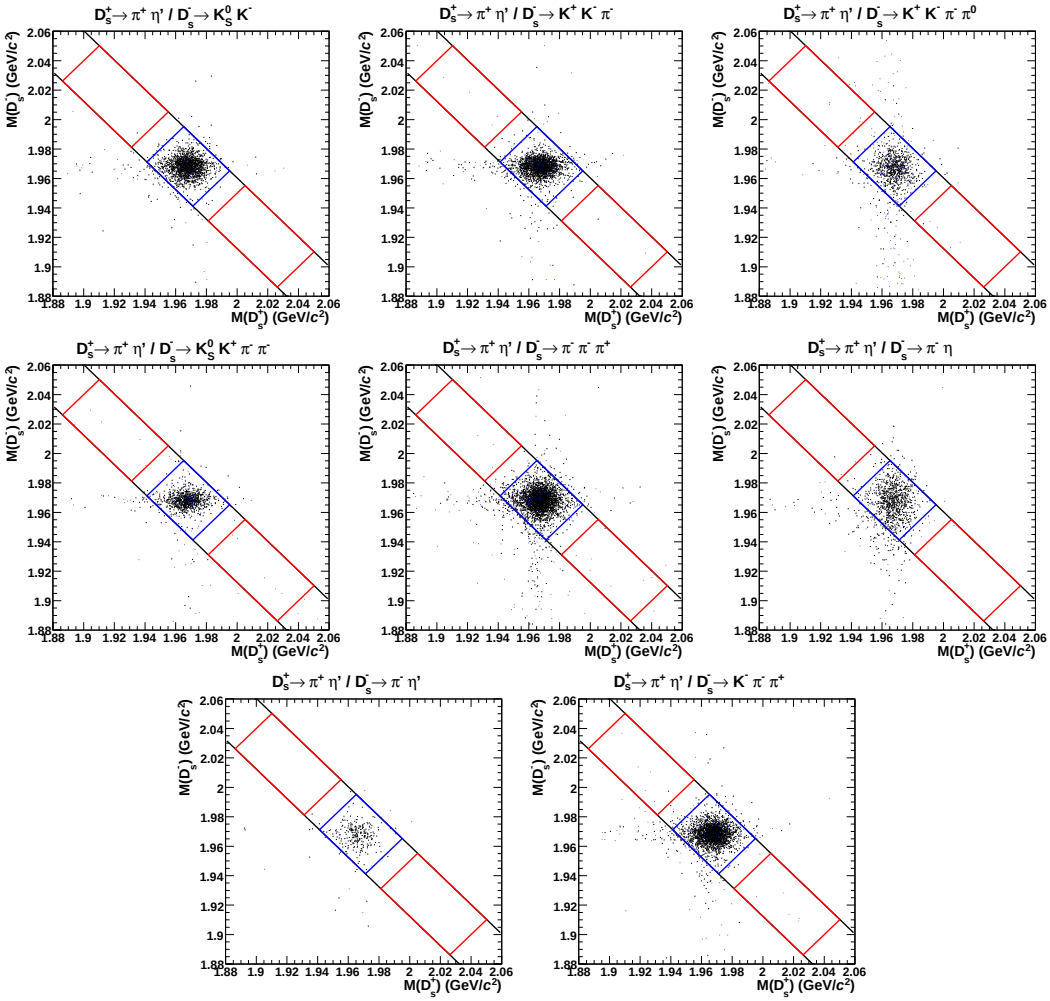

Figure A.40: Signal MC plots of $M_{\rm inv}(D_s^+)$ vs. $M_{\rm inv}(D_s^-)$ in double tag candidates for: (top left) $D_s^+ \to \pi^+\eta'/D_s^- \to K_S^0 K^-$; (top center) $D_s^+ \to \pi^+\eta' /D_s^- \to K^+K^-\pi^-$; (top right) $D_s^+ \to \pi^+\eta'/D_s^- \to K^+K^-\pi^-\pi^0$; (middle left) $D_s^- \to K_S^0 K^-\pi^+\pi^+$; (middle center) $D_s^+ \to \pi^+\eta'/D_s^- \to \pi^-\pi^-\pi^+$; (middle right) $D_s^+ \to \pi^+\eta'/D_s^- \to \pi^-\eta$; (bottom left) $D_s^+ \to \pi^+\eta'/D_s^- \to \pi^-\eta'$; (bottom right) $D_s^+ \to \pi^+\eta'/D_s^- \to K^+\pi^+\pi^-$. Black, blue, and red points correspond to two, one, or zero MC matched D_s candidates, respectively.

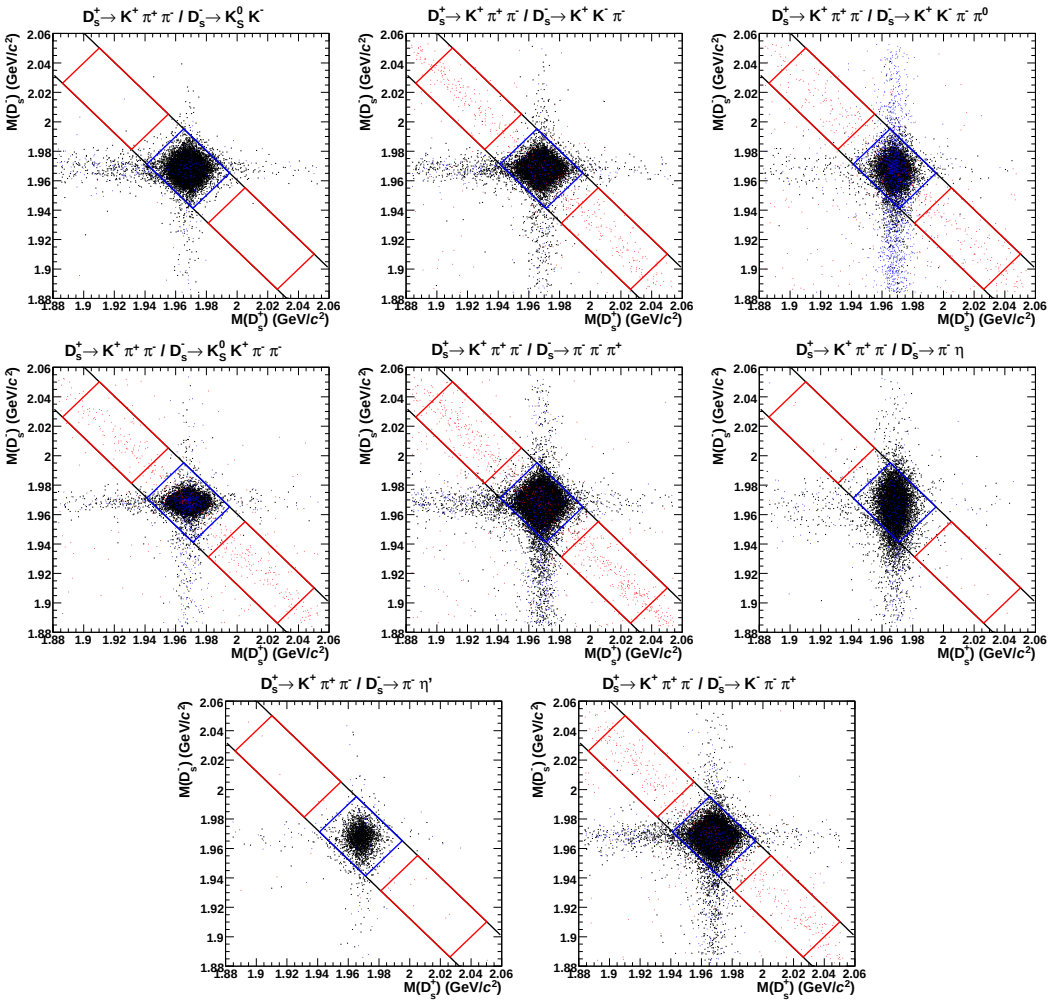

Figure A.41: Signal MC plots of $M_{\text{inv}}(D_s^+)$ vs. $M_{\text{inv}}(D_s^-)$ in double tag candidates for: (top left) $D_s^+ \to K^+\pi^+\pi^-/D_s^- \to K_S^0 K^-$; (top center) $D_s^+ \to K^+\pi^+\pi^- /D_s^- \to K^+K^-\pi^-$; (top right) $D_s^+ \to K^+\pi^+\pi^-/D_s^- \to K^+K^-\pi^-\pi^0$; (middle left) $D_s^- \to K_S^0 K^-\pi^+\pi^+$; (middle center) $D_s^+ \to K^+\pi^+\pi^-/D_s^- \to \pi^-\pi^-\pi^+$; (middle right) $D_s^+ \to K^+\pi^+\pi^-/D_s^- \to \pi^-\eta$; (bottom left) $D_s^+ \to K^+\pi^+\pi^-/D_s^- \to \pi^-\eta'$; (bottom right) $D_s^+ \to K^+\pi^+\pi^-/D_s^- \to K^+\pi^+\pi^-$. Black, blue, and red points correspond to two, one, or zero MC matched D_s candidates, respectively.

A.6 Generic MC Double Tag Yields

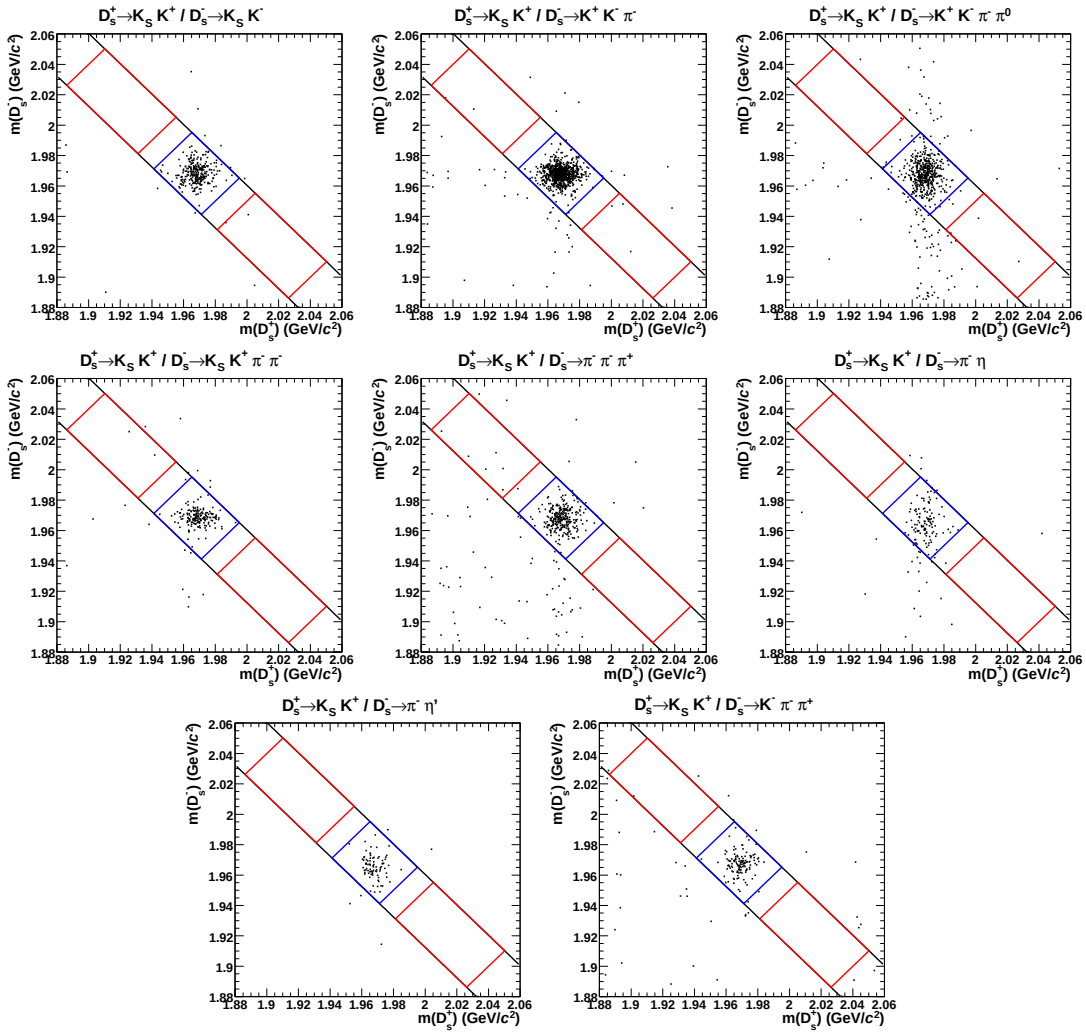

Figure A.42: Generic MC plots of $M_{\rm inv}(D_s^+)$ vs. $M_{\rm inv}(D_s^-)$ in double tag candidates for: (top left) $D_s^+ \to K_S^0 K^+ / D_s^- \to K_S^0 K^-$; (top center) $D_s^+ \to K_S^0 K^+ / D_s^- \to K^+ K^- \pi^-$; (top right) $D_s^+ \to K_S^0 K^+ / D_s^- \to K^+ K^- \pi^- \pi^0$; (middle left) $D_s^- \to K_S^0 K^- \pi^+ \pi^+$; (middle center) $D_s^+ \to K_S^0 K^+ / D_s^- \to \pi^- \pi^- \pi^+$; (middle right) $D_s^+ \to K_S^0 K^+ / D_s^- \to \pi^- \eta$; (bottom left) $D_s^+ \to K_S^0 K^+ / D_s^- \to \pi^- \eta'$; (bottom right) $D_s^+ \to K_S^0 K^+ / D_s^- \to K^+ \pi^+ \pi^-$.

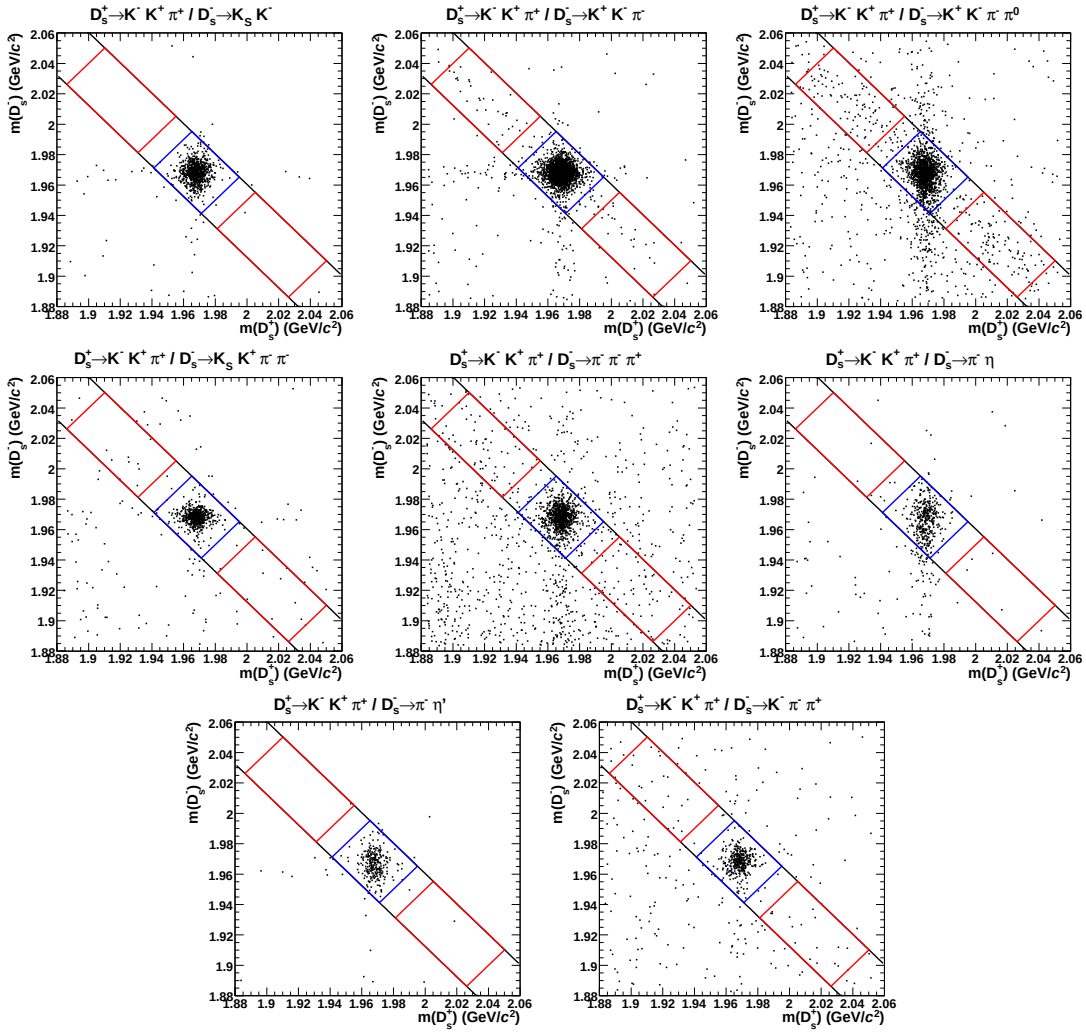

Figure A.43: Generic MC plots of $M_{\rm inv}(D_s^+)$ vs. $M_{\rm inv}(D_s^-)$ in double tag candidates for: (top left) $D_s^+ \to K^-K^+\pi^+/D_s^- \to K_S^0K^-$; (top center) $D_s^+ \to K^-K^+\pi^+ /D_s^- \to K^+K^-\pi^-$; (top right) $D_s^+ \to K^-K^+\pi^+/D_s^- \to K^+K^-\pi^-\pi^0$; (middle left) $D_s^- \to K_S^0K^-\pi^+\pi^+$; (middle center) $D_s^+ \to K^-K^+\pi^+/D_s^- \to \pi^-\pi^-\pi^+$; (middle right) $D_s^+ \to K^-K^+\pi^+/D_s^- \to \pi^-\eta$; (bottom left) $D_s^+ \to K^-K^+\pi^+/D_s^- \to \pi^-\eta'$; (bottom right) $D_s^+ \to K^-K^+\pi^+/D_s^- \to K^+\pi^+\pi^-$.

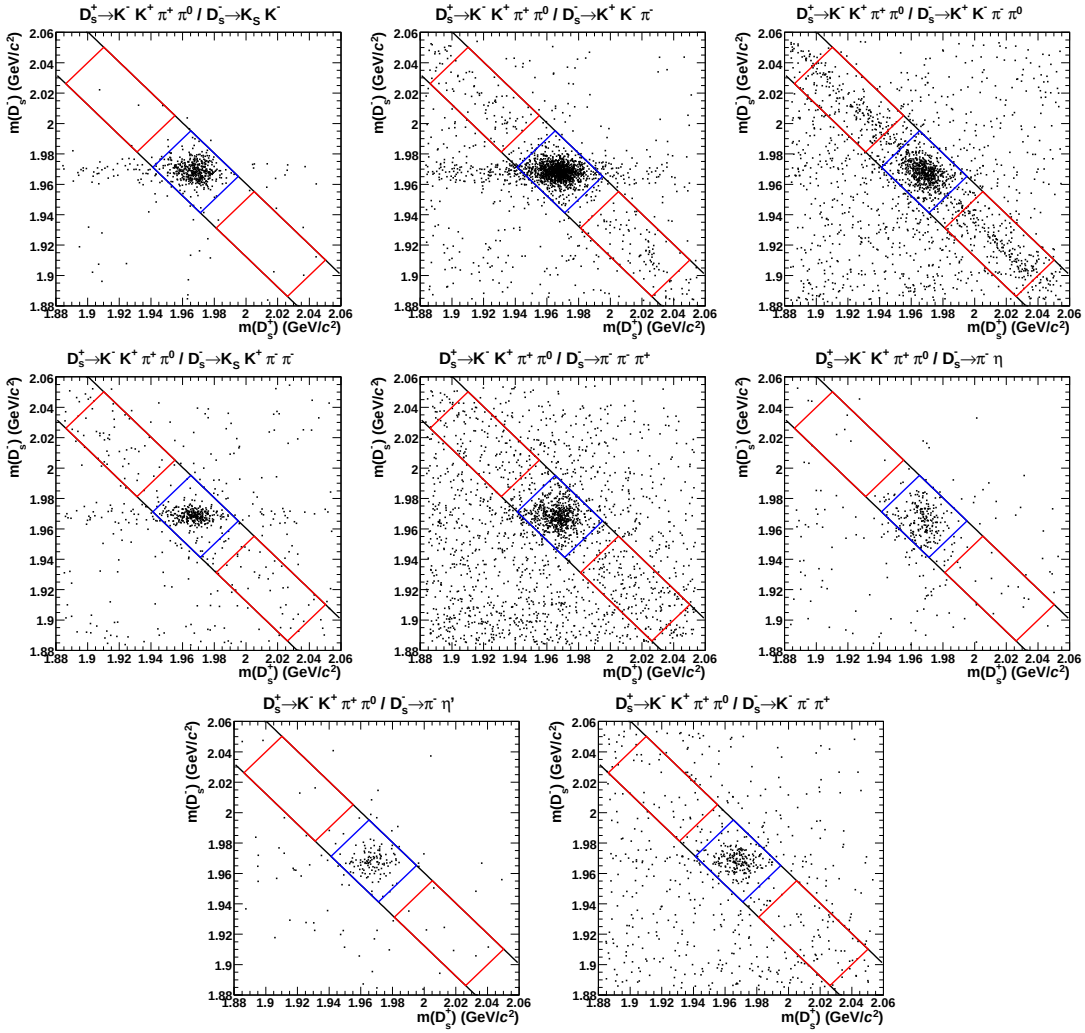

Figure A.44: Generic MC plots of $M_{\rm inv}(D_s^+)$ vs. $M_{\rm inv}(D_s^-)$ in double tag candidates for: (top left) $D_s^+ \to K^-K^+\pi^+\pi^0/D_s^- \to K_S^0K^-$; (top center) $D_s^+ \to K^-K^+\pi^+\pi^0$ /$D_s^- \to K^+K^-\pi^-$; (top right) $D_s^+ \to K^-K^+\pi^+\pi^0/D_s^- \to K^+K^-\pi^-\pi^0$; (middle left) $D_s^- \to K_S^0K^-\pi^+\pi^+$; (middle center) $D_s^+ \to K^-K^+\pi^+\pi^0/D_s^- \to \pi^-\pi^-\pi^+$; (middle right) $D_s^+ \to K^-K^+\pi^+\pi^0/D_s^- \to \pi^-\eta$; (bottom left) $D_s^+ \to K^-K^+\pi^+\pi^0/D_s^- \to \pi^-\eta'$; (bottom right) $D_s^+ \to K^-K^+\pi^+\pi^0/D_s^- \to K^+\pi^+\pi^-$.

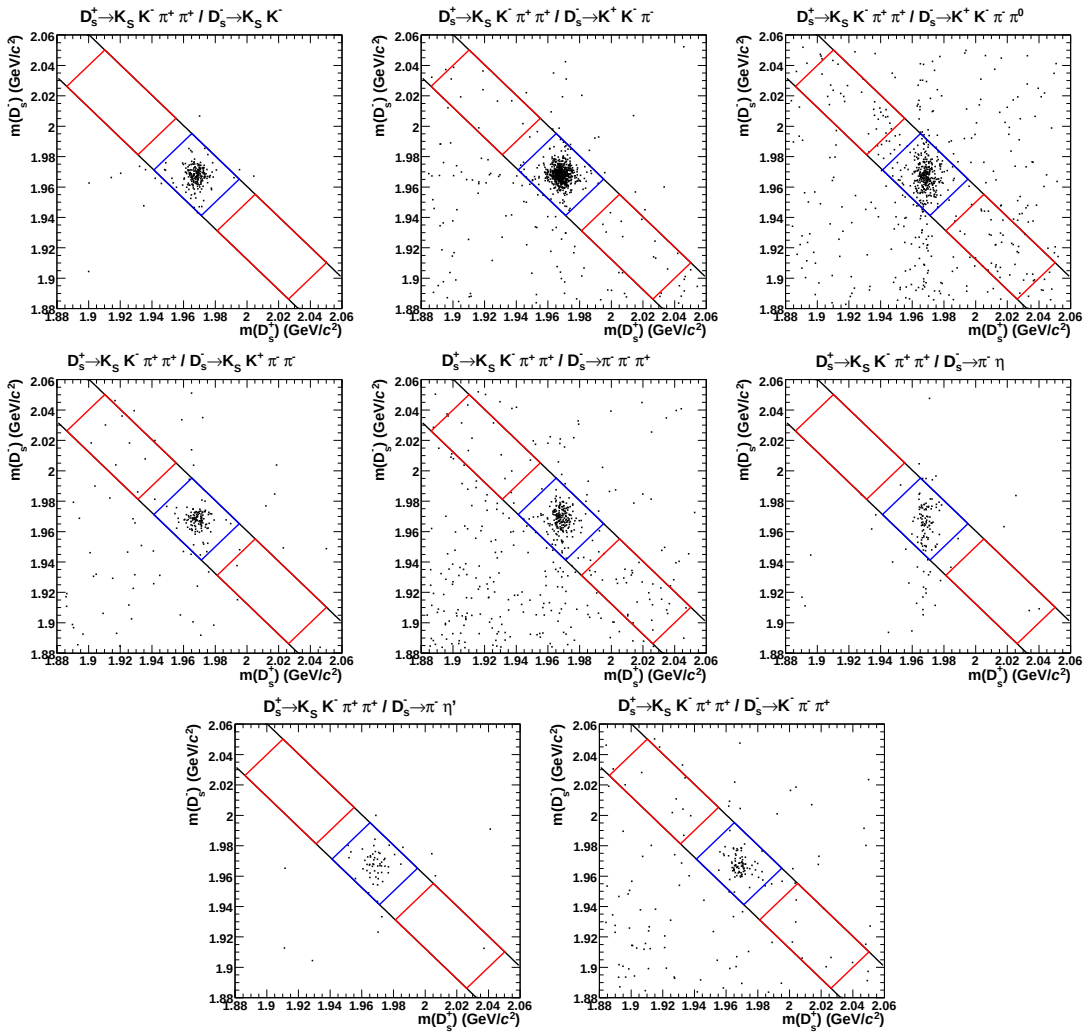

Figure A.45: Generic MC plots of $M_{\text{inv}}(D_s^+)$ vs. $M_{\text{inv}}(D_s^-)$ in double tag candidates for: (top left) $D_s^+ \to K_S^0 K^- \pi^+ \pi^+ / D_s^- \to K_S^0 K^-$; (top center) $D_s^+ \to K_S^0 K^- \pi^+ \pi^+ / D_s^- \to K^+ K^- \pi^-$; (top right) $D_s^+ \to K_S^0 K^- \pi^+ \pi^+ / D_s^- \to K^+ K^- \pi^- \pi^0$; (middle left) $D_s^- \to K_S^0 K^- \pi^+ \pi^+$; (middle center) $D_s^+ \to K_S^0 K^- \pi^+ \pi^+ / D_s^- \to \pi^- \pi^- \pi^+$; (middle right) $D_s^+ \to K_S^0 K^- \pi^+ \pi^+ / D_s^- \to \pi^- \eta$; (bottom left) $D_s^+ \to K_S^0 K^- \pi^+ \pi^+ / D_s^- \to \pi^- \eta'$; (bottom right) $D_s^+ \to K_S^0 K^- \pi^+ \pi^+ / D_s^- \to K^+ \pi^+ \pi^-$.

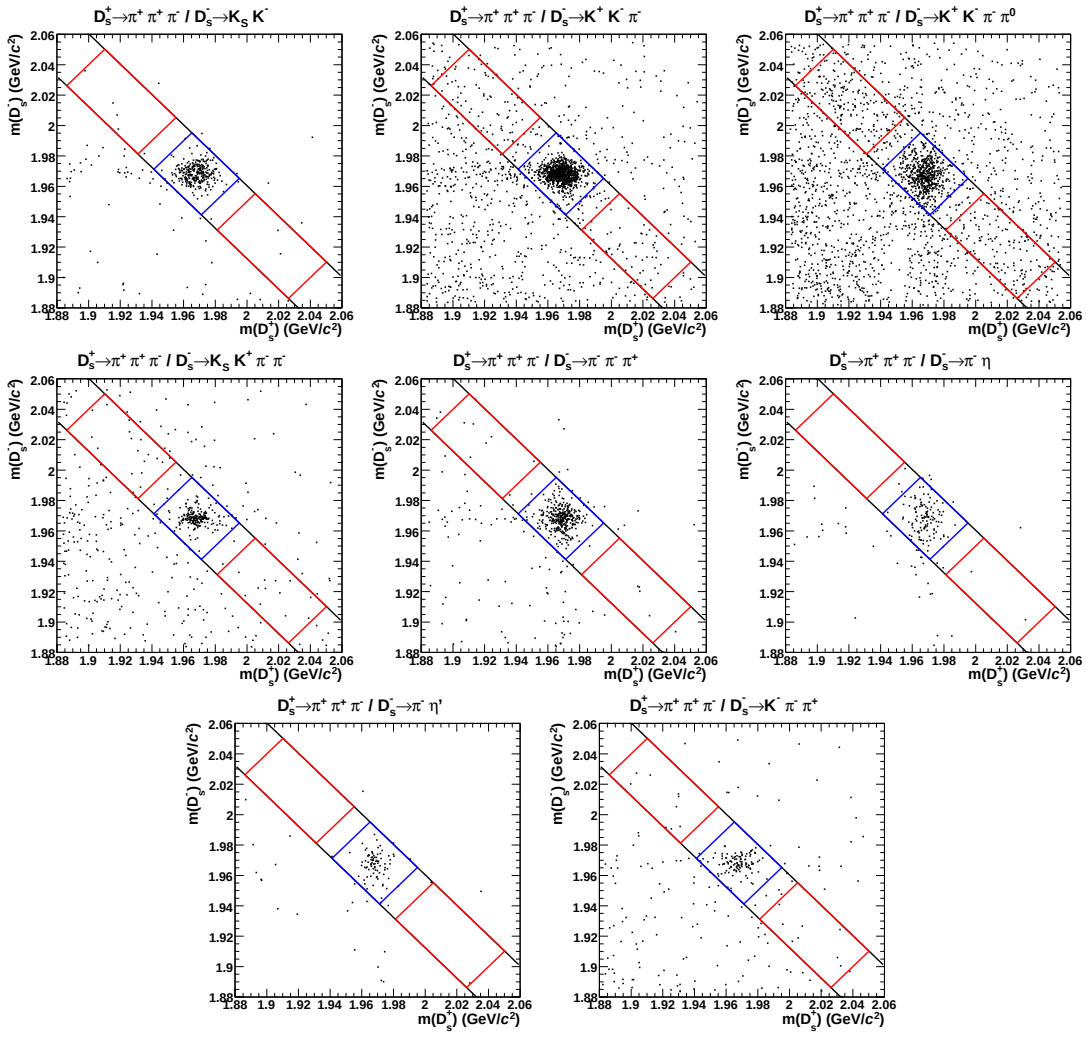

Figure A.46: Generic MC plots of $M_{\rm inv}(D_s^+)$ vs. $M_{\rm inv}(D_s^-)$ in double tag candidates for: (top left) $D_s^+ \to \pi^+\pi^+\pi^-/D_s^- \to K_S^0 K^-$; (top center) $D_s^+ \to \pi^+\pi^+\pi^- /D_s^- \to K^+K^-\pi^-$; (top right) $D_s^+ \to \pi^+\pi^+\pi^-/D_s^- \to K^+K^-\pi^-\pi^0$; (middle left) $D_s^- \to K_S^0 K^-\pi^+\pi^+$; (middle center) $D_s^+ \to \pi^+\pi^+\pi^-/D_s^- \to \pi^-\pi^-\pi^+$; (middle right) $D_s^+ \to \pi^+\pi^+\pi^-/D_s^- \to \pi^-\eta$; (bottom left) $D_s^+ \to \pi^+\pi^+\pi^-/D_s^- \to \pi^-\eta'$; (bottom right) $D_s^+ \to \pi^+\pi^+\pi^-/D_s^- \to K^+\pi^+\pi^-$.

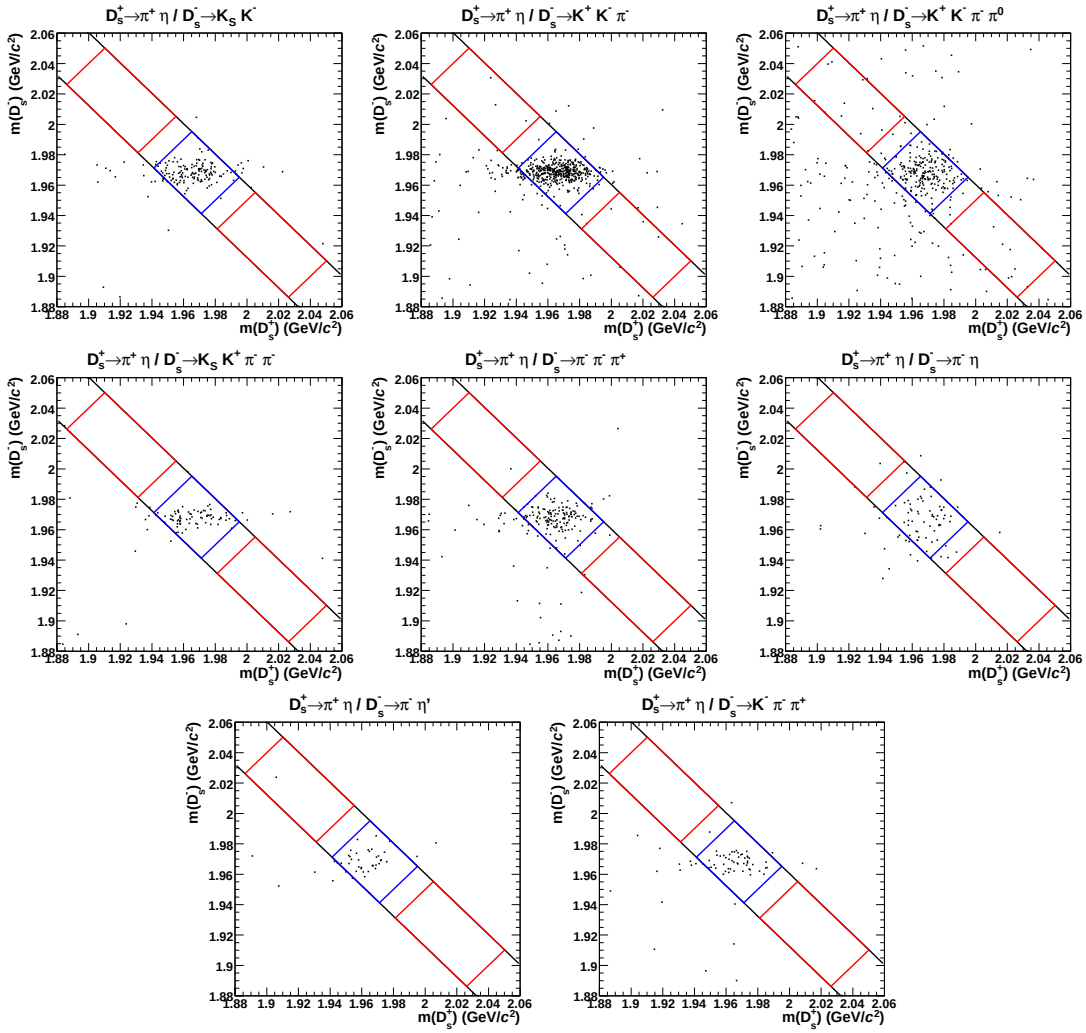

Figure A.47: Generic MC plots of $M_{\rm inv}(D_s^+)$ vs. $M_{\rm inv}(D_s^-)$ in double tag candidates for: (top left) $D_s^+ \to \pi^+\eta/D_s^- \to K_S^0 K^-$; (top center) $D_s^+ \to \pi^+\eta\ /D_s^- \to K^+K^-\pi^-$; (top right) $D_s^+ \to \pi^+\eta/D_s^- \to K^+K^-\pi^-\pi^0$; (middle left) $D_s^- \to K_S^0 K^-\pi^+\pi^+$; (middle center) $D_s^+ \to \pi^+\eta/D_s^- \to \pi^-\pi^-\pi^+$; (middle right) $D_s^+ \to \pi^+\eta/D_s^- \to \pi^-\eta$; (bottom left) $D_s^+ \to \pi^+\eta/D_s^- \to \pi^-\eta'$; (bottom right) $D_s^+ \to \pi^+\eta/D_s^- \to K^+\pi^+\pi^-$.

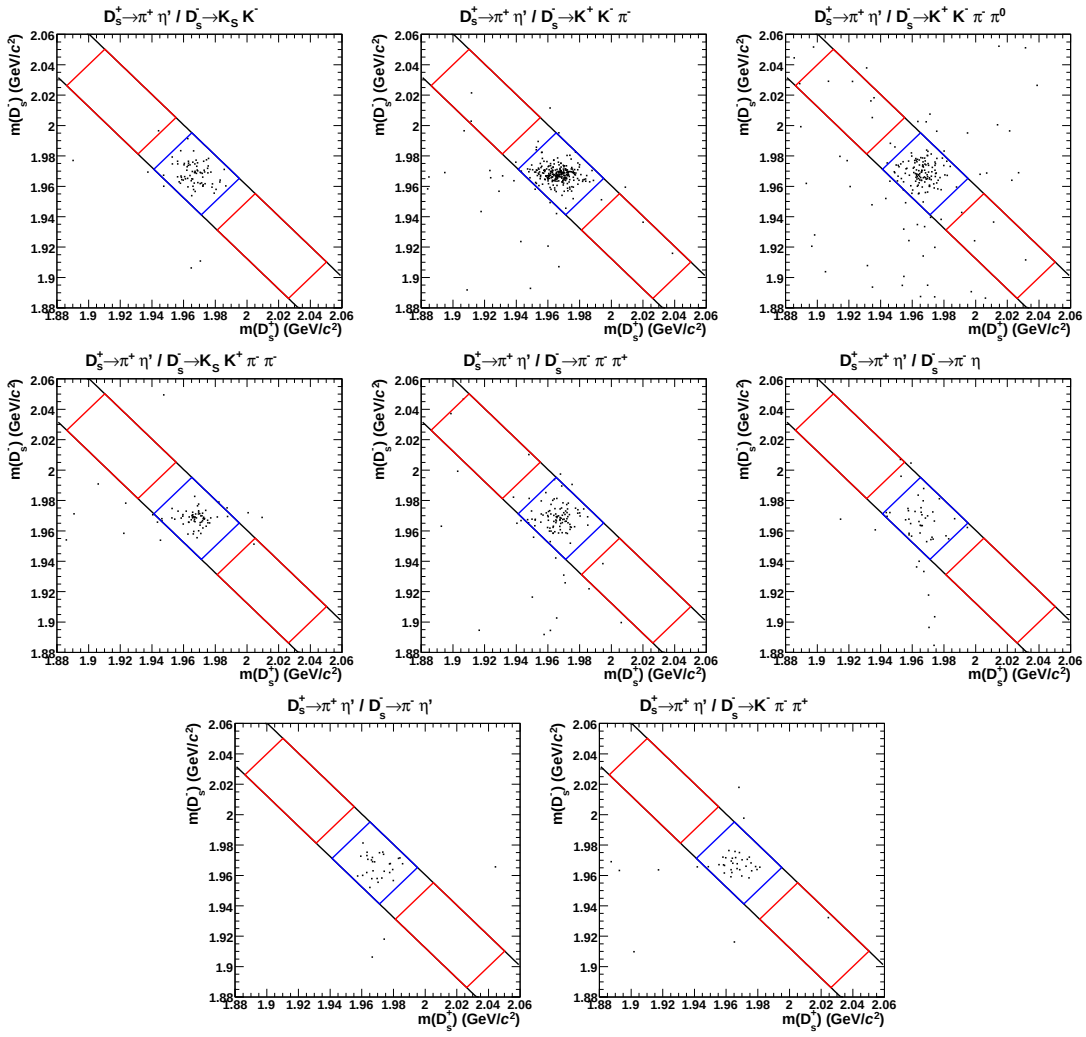

Figure A.48: Generic MC plots of $M_{\rm inv}(D_s^+)$ vs. $M_{\rm inv}(D_s^-)$ in double tag candidates for: (top left) $D_s^+ \to \pi^+\eta'/D_s^- \to K_S^0 K^-$; (top center) $D_s^+ \to \pi^+\eta'$ $/D_s^- \to K^+K^-\pi^-$; (top right) $D_s^+ \to \pi^+\eta'/D_s^- \to K^+K^-\pi^-\pi^0$; (middle left) $D_s^- \to K_S^0 K^-\pi^+\pi^+$; (middle center) $D_s^+ \to \pi^+\eta'/D_s^- \to \pi^-\pi^-\pi^+$; (middle right) $D_s^+ \to \pi^+\eta'/D_s^- \to \pi^-\eta$; (bottom left) $D_s^+ \to \pi^+\eta'/D_s^- \to \pi^-\eta'$; (bottom right) $D_s^+ \to \pi^+\eta'/D_s^- \to K^+\pi^+\pi^-$.

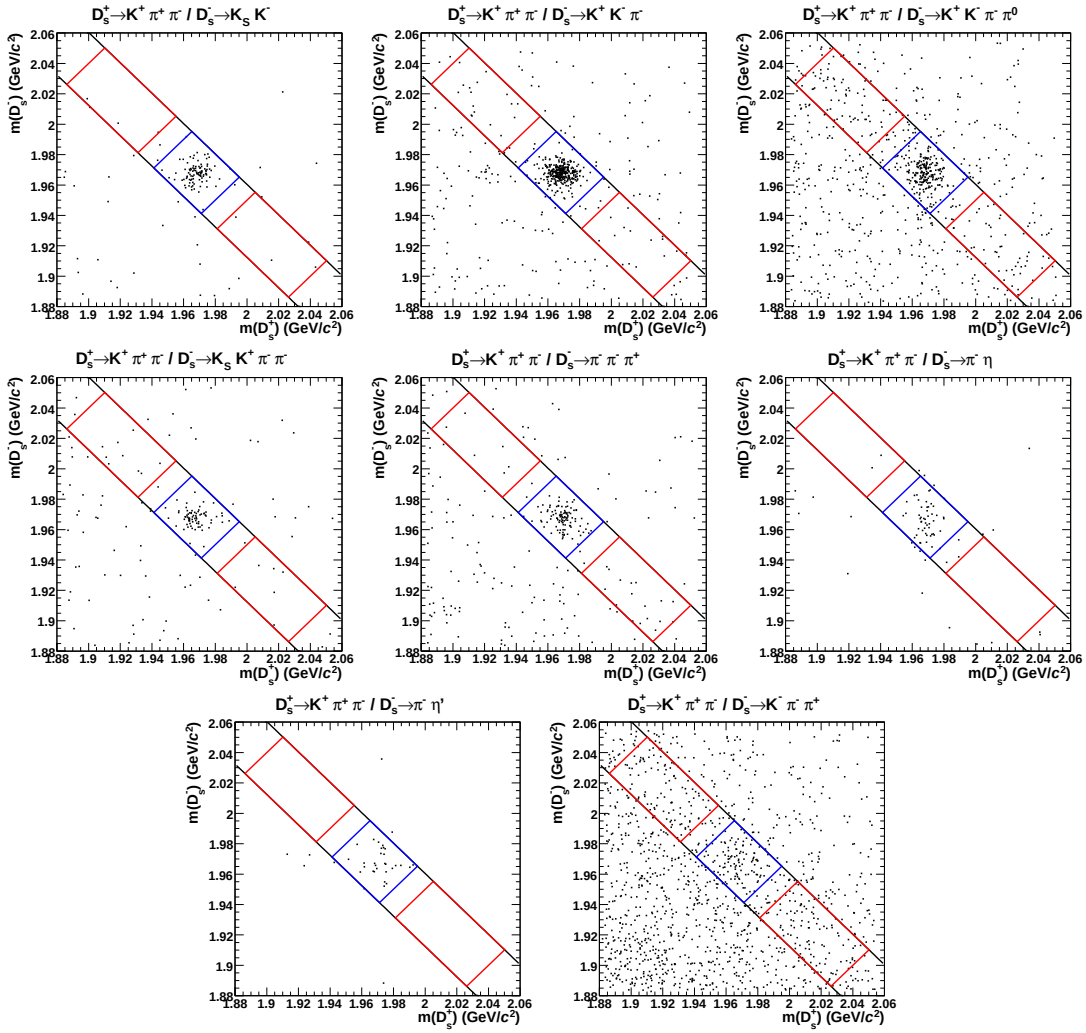

Figure A.49: Generic MC plots of $M_{\rm inv}(D_s^+)$ vs. $M_{\rm inv}(D_s^-)$ in double tag candidates for: (top left) $D_s^+ \to K^+\pi^+\pi^-/D_s^- \to K_S^0 K^-$; (top center) $D_s^+ \to K^+\pi^+\pi^-/D_s^- \to K^+K^-\pi^-$; (top right) $D_s^+ \to K^+\pi^+\pi^-/D_s^- \to K^+K^-\pi^-\pi^0$; (middle left) $D_s^- \to K_S^0 K^-\pi^+\pi^+$; (middle center) $D_s^+ \to K^+\pi^+\pi^-/D_s^- \to \pi^-\pi^-\pi^+$; (middle right) $D_s^+ \to K^+\pi^+\pi^-/D_s^- \to \pi^-\eta$; (bottom left) $D_s^+ \to K^+\pi^+\pi^-/D_s^- \to \pi^-\eta'$; (bottom right) $D_s^+ \to K^+\pi^+\pi^-/D_s^- \to K^+\pi^+\pi^-$.

A.7 Data Double Tag Yields

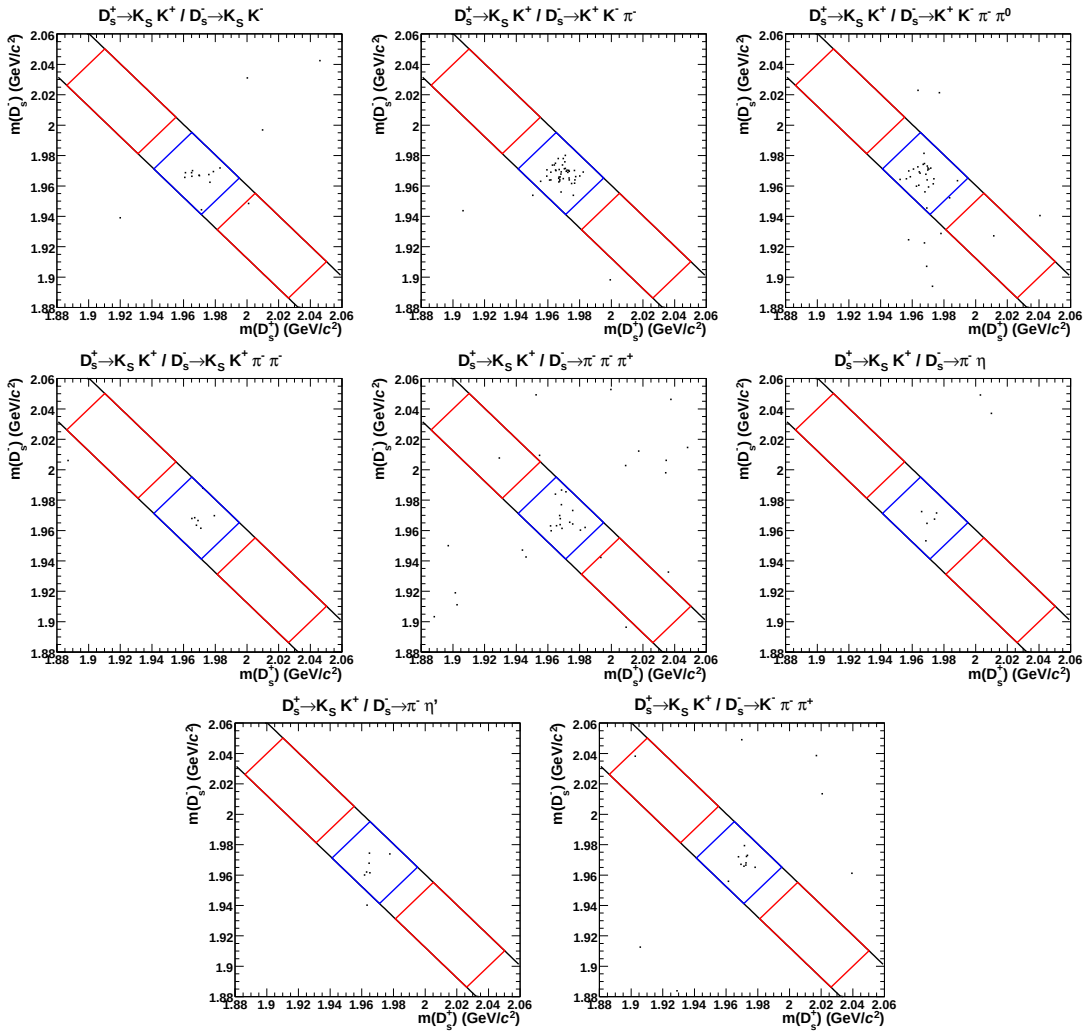

Figure A.50: Data plots of $M_{\rm inv}(D_s^+)$ vs. $M_{\rm inv}(D_s^-)$ in double tag candidates for: (top left) $D_s^+ \to K_S^0 K^+ / D_s^- \to K_S^0 K^-$; (top center) $D_s^+ \to K_S^0 K^+ / D_s^- \to K^+ K^- \pi^-$; (top right) $D_s^+ \to K_S^0 K^+ / D_s^- \to K^+ K^- \pi^- \pi^0$; (middle left) $D_s^- \to K_S^0 K^- \pi^+ \pi^+$; (middle center) $D_s^+ \to K_S^0 K^+ / D_s^- \to \pi^- \pi^- \pi^+$; (middle right) $D_s^+ \to K_S^0 K^+ / D_s^- \to \pi^- \eta$; (bottom left) $D_s^+ \to K_S^0 K^+ / D_s^- \to \pi^- \eta'$; (bottom right) $D_s^+ \to K_S^0 K^+ / D_s^- \to K^+ \pi^+ \pi^-$.

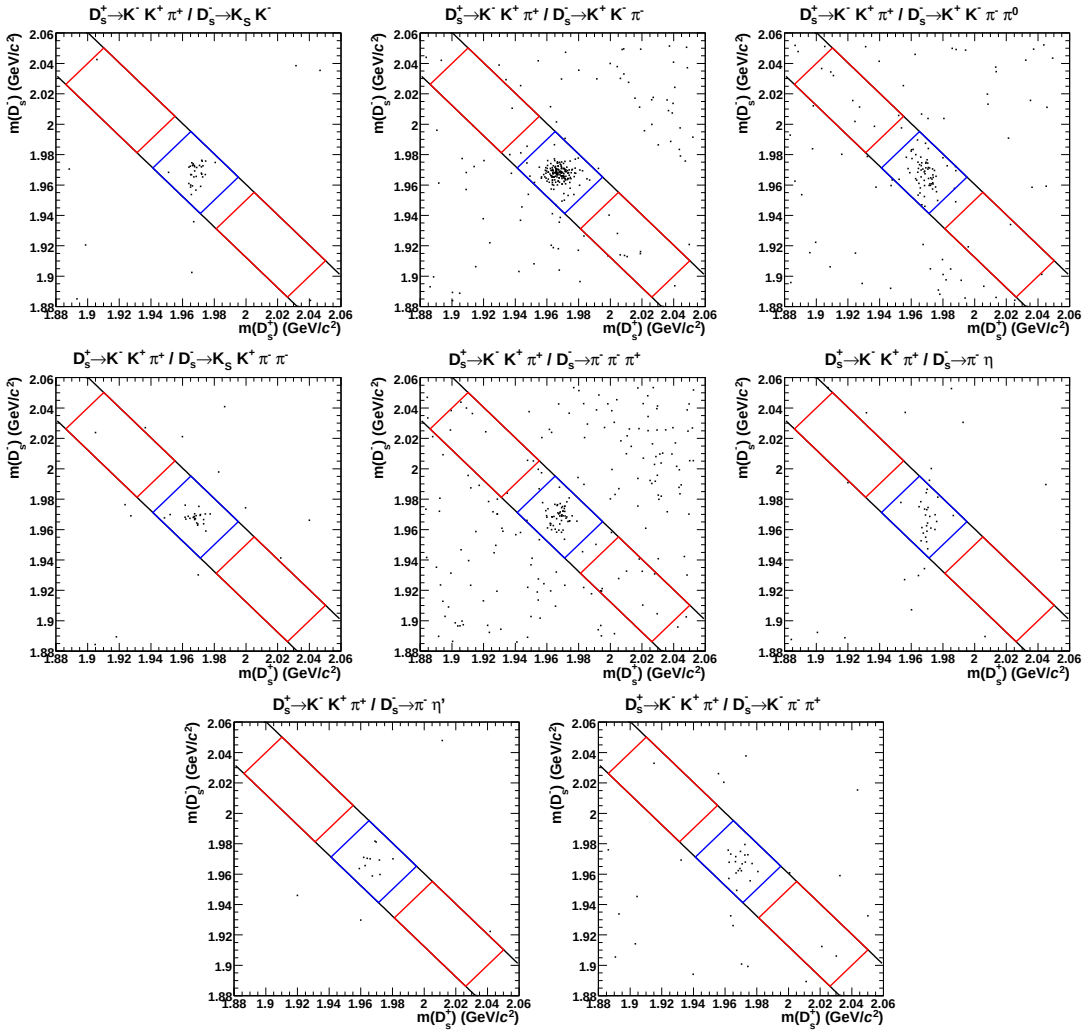

Figure A.51: Data plots of $M_{\rm inv}(D_s^+)$ vs. $M_{\rm inv}(D_s^-)$ in double tag candidates for: (top left) $D_s^+ \to K^-K^+\pi^+/D_s^- \to K_S^0K^-$; (top center) $D_s^+ \to K^-K^+\pi^+ /D_s^- \to K^+K^-\pi^-$; (top right) $D_s^+ \to K^-K^+\pi^+/D_s^- \to K^+K^-\pi^-\pi^0$; (middle left) $D_s^- \to K_S^0K^-\pi^+\pi^+$; (middle center) $D_s^+ \to K^-K^+\pi^+/D_s^- \to \pi^-\pi^-\pi^+$; (middle right) $D_s^+ \to K^-K^+\pi^+/D_s^- \to \pi^-\eta$; (bottom left) $D_s^+ \to K^-K^+\pi^+/D_s^- \to \pi^-\eta'$; (bottom right) $D_s^+ \to K^-K^+\pi^+/D_s^- \to K^+\pi^+\pi^-$.

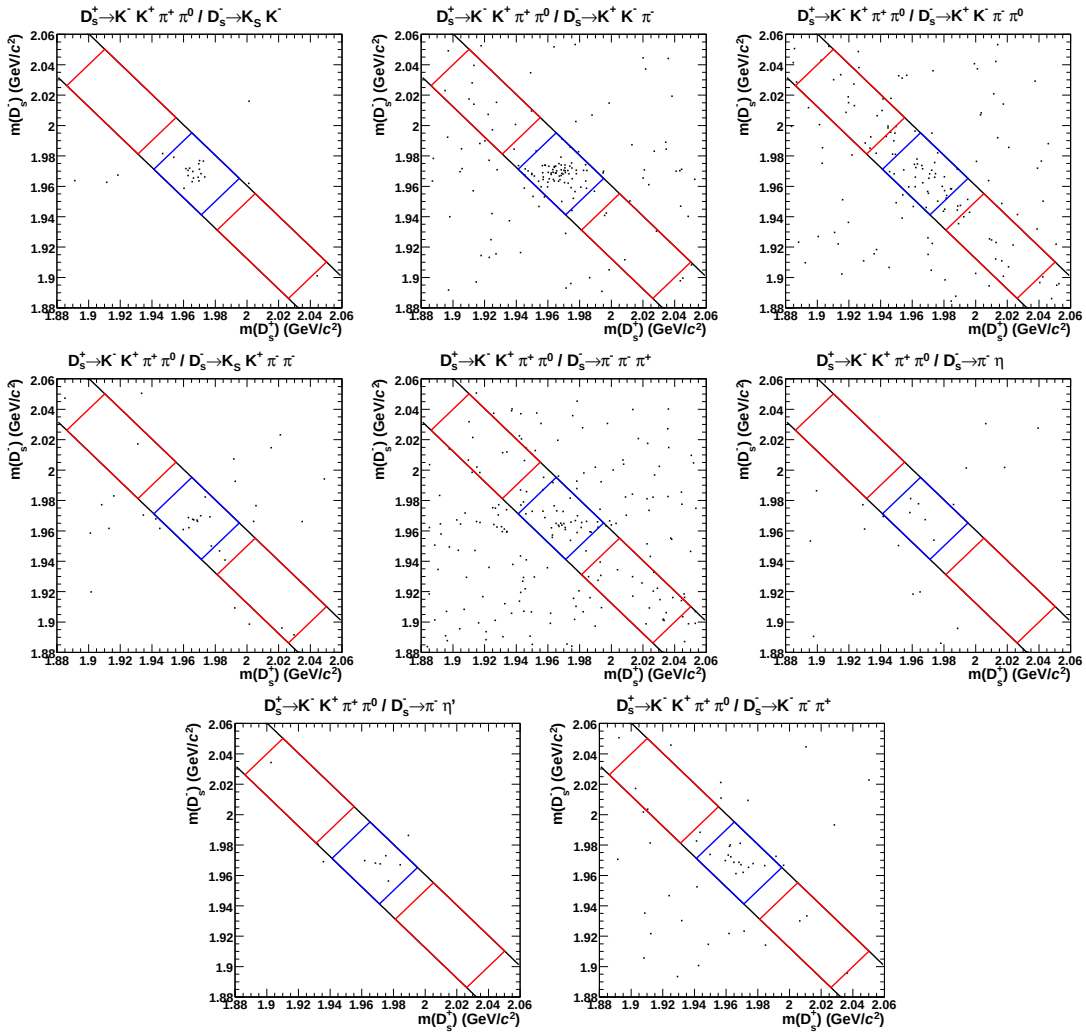

Figure A.52: Data plots of $M_{\text{inv}}(D_s^+)$ vs. $M_{\text{inv}}(D_s^-)$ in double tag candidates for: (top left) $D_s^+ \to K^-K^+\pi^+\pi^0/D_s^- \to K_S^0K^-$; (top center) $D_s^+ \to K^-K^+\pi^+\pi^0$ /$D_s^- \to K^+K^-\pi^-$; (top right) $D_s^+ \to K^-K^+\pi^+\pi^0/D_s^- \to K^+K^-\pi^-\pi^0$; (middle left) $D_s^- \to K_S^0K^-\pi^+\pi^+$; (middle center) $D_s^+ \to K^-K^+\pi^+\pi^0/D_s^- \to \pi^-\pi^-\pi^+$; (middle right) $D_s^+ \to K^-K^+\pi^+\pi^0/D_s^- \to \pi^-\eta$; (bottom left) $D_s^+ \to K^-K^+\pi^+\pi^0/D_s^- \to \pi^-\eta'$; (bottom right) $D_s^+ \to K^-K^+\pi^+\pi^0/D_s^- \to K^+\pi^+\pi^-$.

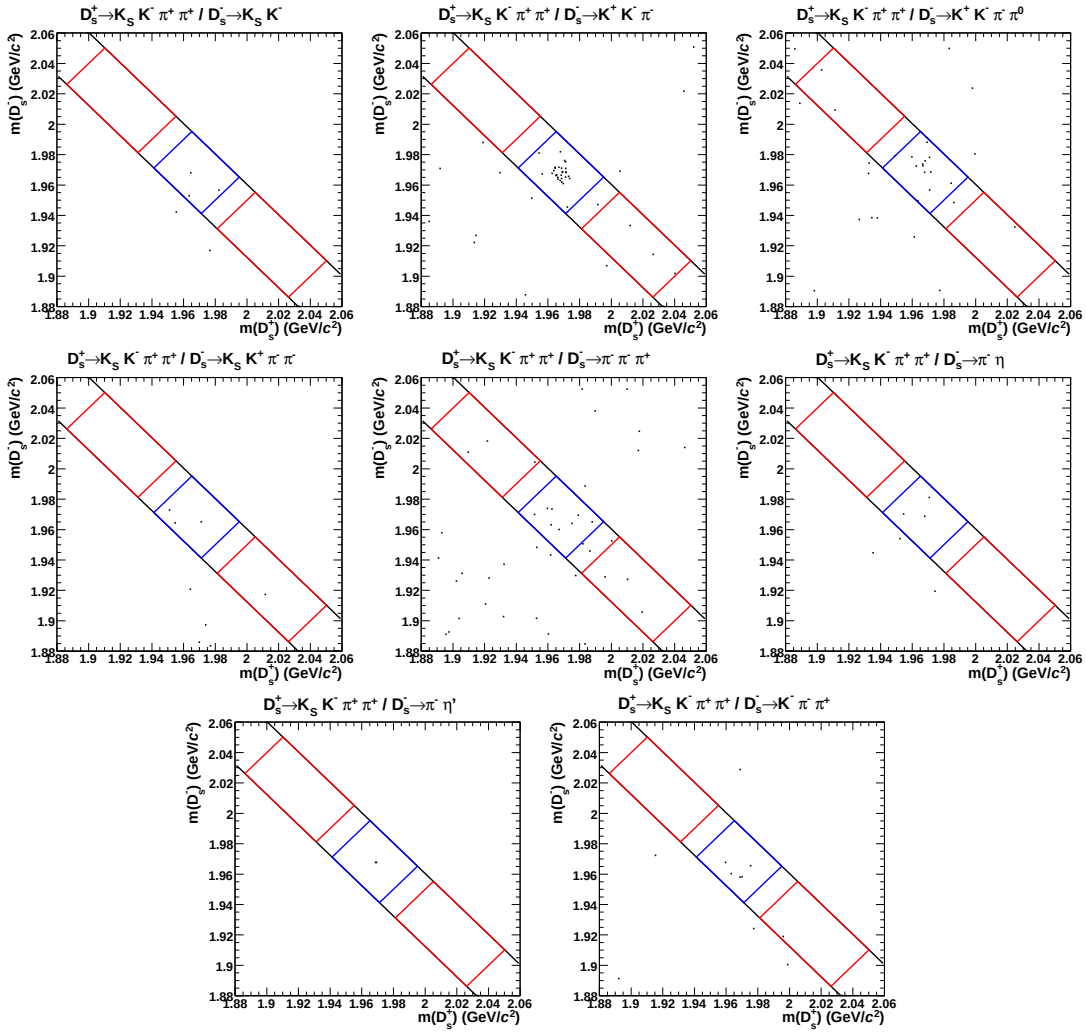

Figure A.53: Data plots of $M_{\text{inv}}(D_s^+)$ vs. $M_{\text{inv}}(D_s^-)$ candidates for: (top left) $D_s^+ \to K_S^0 K^- \pi^+ \pi^+ / D_s^- \to K_S^0 K^-$; (top center) $D_s^+ \to K_S^0 K^- \pi^+ \pi^+ / D_s^- \to K^+ K^- \pi^-$; (top right) $D_s^+ \to K_S^0 K^- \pi^+ \pi^+ / D_s^- \to K^+ K^- \pi^- \pi^0$; (middle left) $D_s^- \to K_S^0 K^- \pi^+ \pi^+$; (middle center) $D_s^+ \to K_S^0 K^- \pi^+ \pi^+ / D_s^- \to \pi^- \pi^- \pi^+$; (middle right) $D_s^+ \to K_S^0 K^- \pi^+ \pi^+ / D_s^- \to \pi^- \eta$; (bottom left) $D_s^+ \to K_S^0 K^- \pi^+ \pi^+ / D_s^- \to \pi^- \eta'$; (bottom right) $D_s^+ \to K_S^0 K^- \pi^+ \pi^+ / D_s^- \to K^+ \pi^+ \pi^-$.

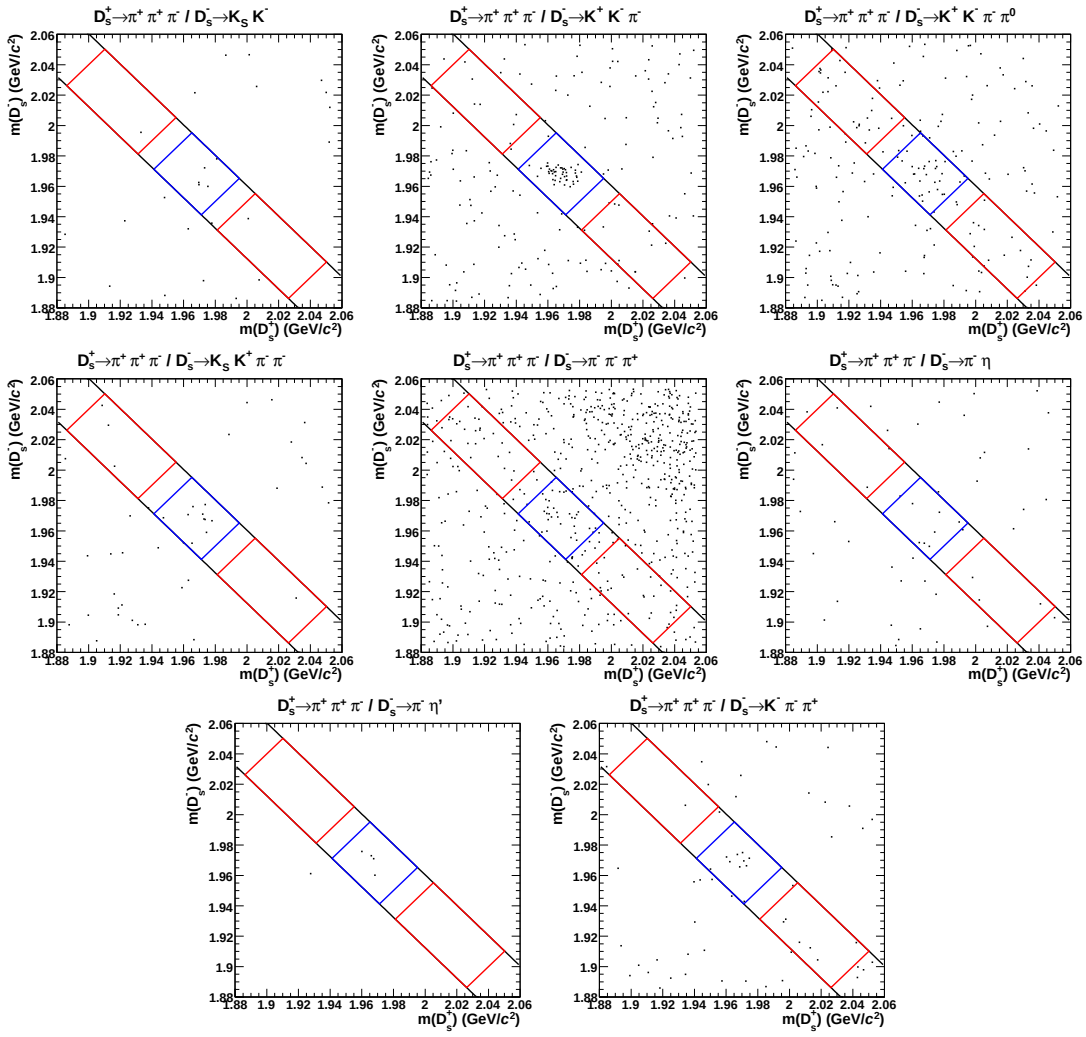

Figure A.54: Data plots of $M_{\rm inv}(D_s^+)$ vs. $M_{\rm inv}(D_s^-)$ in double tag candidates for: (top left) $D_s^+ \to \pi^+\pi^+\pi^-/D_s^- \to K_S^0 K^-$; (top center) $D_s^+ \to \pi^+\pi^+\pi^- /D_s^- \to K^+K^-\pi^-$; (top right) $D_s^+ \to \pi^+\pi^+\pi^-/D_s^- \to K^+K^-\pi^-\pi^0$; (middle left) $D_s^- \to K_S^0 K^-\pi^+\pi^+$; (middle center) $D_s^+ \to \pi^+\pi^+\pi^-/D_s^- \to \pi^-\pi^-\pi^+$; (middle right) $D_s^+ \to \pi^+\pi^+\pi^-/D_s^- \to \pi^-\eta$; (bottom left) $D_s^+ \to \pi^+\pi^+\pi^-/D_s^- \to \pi^-\eta'$; (bottom right) $D_s^+ \to \pi^+\pi^+\pi^-/D_s^- \to K^+\pi^+\pi^-$.

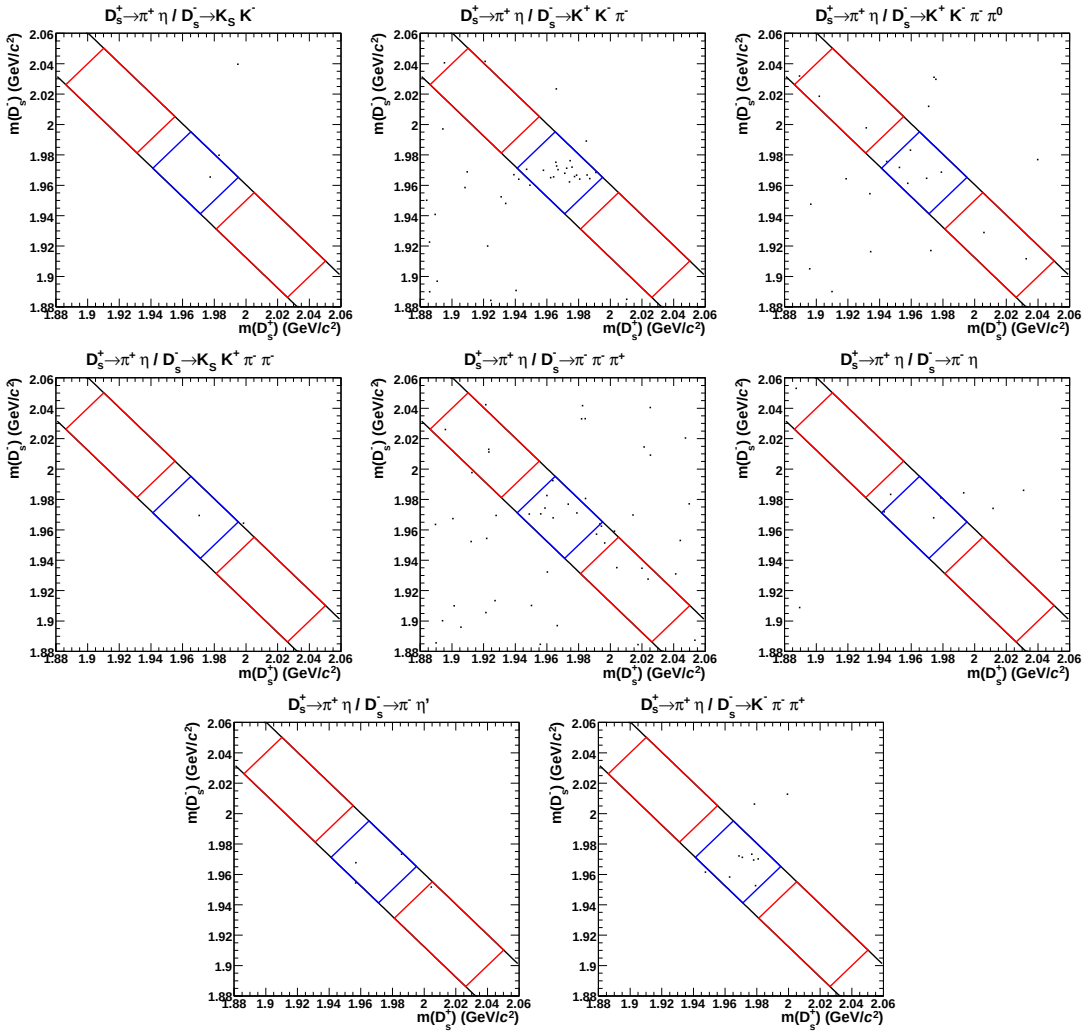

Figure A.55: Data plots of $M_{\rm inv}(D_s^+)$ vs. $M_{\rm inv}(D_s^-)$ in double tag candidates for: (top left) $D_s^+ \to \pi^+\eta/D_s^- \to K_S^0 K^-$; (top center) $D_s^+ \to \pi^+\eta/D_s^- \to K^+K^-\pi^-$; (top right) $D_s^+ \to \pi^+\eta/D_s^- \to K^+K^-\pi^-\pi^0$; (middle left) $D_s^- \to K_S^0 K^-\pi^+\pi^+$; (middle center) $D_s^+ \to \pi^+\eta/D_s^- \to \pi^-\pi^-\pi^+$; (middle right) $D_s^+ \to \pi^+\eta/D_s^- \to \pi^-\eta$; (bottom left) $D_s^+ \to \pi^+\eta/D_s^- \to \pi^-\eta'$; (bottom right) $D_s^+ \to \pi^+\eta/D_s^- \to K^+\pi^+\pi^-$.

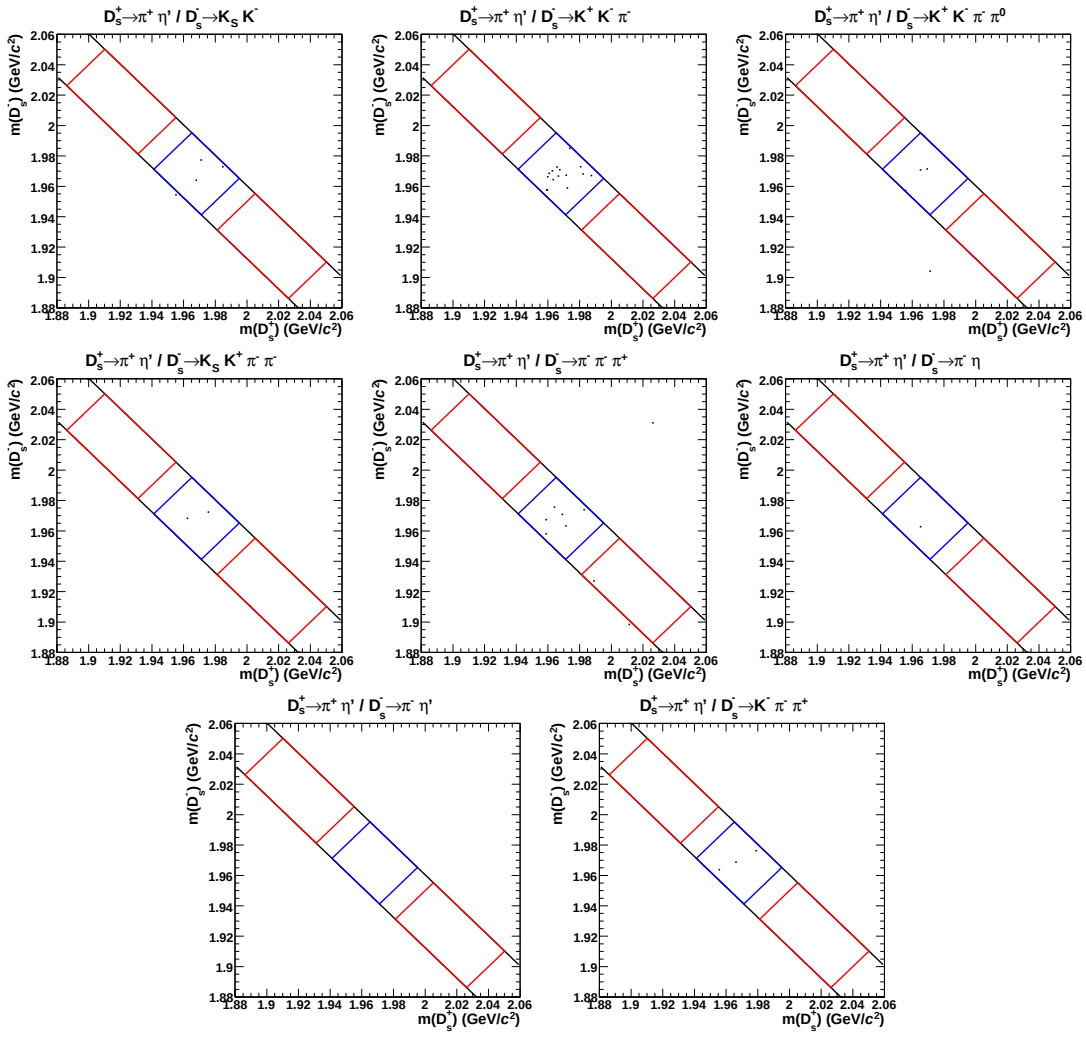

Figure A.56: Data plots of $M_{\rm inv}(D_s^+)$ vs. $M_{\rm inv}(D_s^-)$ in double tag candidates for: (top left) $D_s^+ \to \pi^+\eta'/D_s^- \to K_S^0 K^-$; (top center) $D_s^+ \to \pi^+\eta'$ $/D_s^- \to K^+K^-\pi^-$; (top right) $D_s^+ \to \pi^+\eta'/D_s^- \to K^+K^-\pi^-\pi^0$; (middle left) $D_s^- \to K_S^0 K^-\pi^+\pi^+$; (middle center) $D_s^+ \to \pi^+\eta'/D_s^- \to \pi^-\pi^-\pi^+$; (middle right) $D_s^+ \to \pi^+\eta'/D_s^- \to \pi^-\eta$; (bottom left) $D_s^+ \to \pi^+\eta'/D_s^- \to \pi^-\eta'$; (bottom right) $D_s^+ \to \pi^+\eta'/D_s^- \to K^+\pi^+\pi^-$.

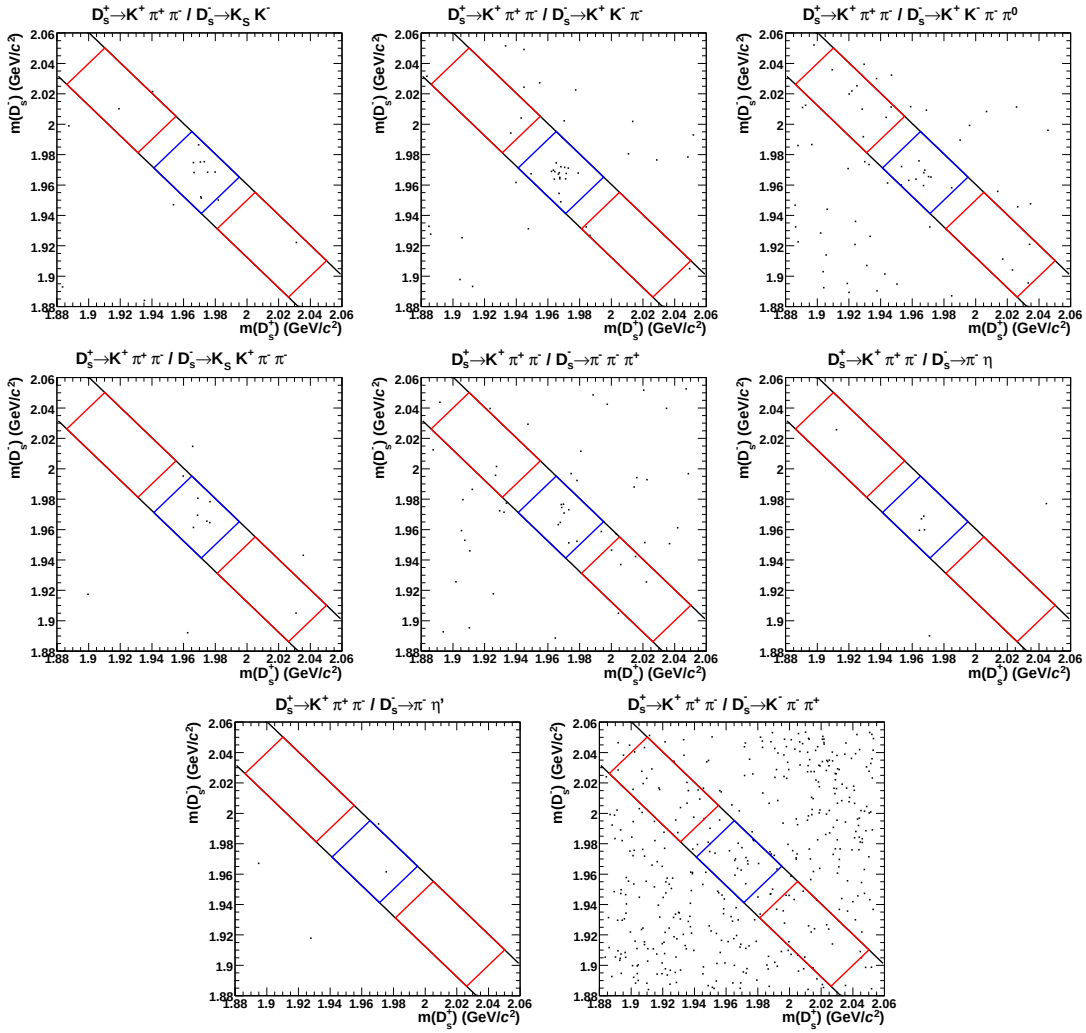

Figure A.57: Data plots of $M_{\rm inv}(D_s^+)$ vs. $M_{\rm inv}(D_s^-)$ in double tag candidates for: (top left) $D_s^+ \to K^+\pi^+\pi^-/D_s^- \to K_S^0 K^-$; (top center) $D_s^+ \to K^+\pi^+\pi^- /D_s^- \to K^+K^-\pi^-$; (top right) $D_s^+ \to K^+\pi^+\pi^-/D_s^- \to K^+K^-\pi^-\pi^0$; (middle left) $D_s^- \to K_S^0 K^-\pi^+\pi^+$; (middle center) $D_s^+ \to K^+\pi^+\pi^-/D_s^- \to \pi^-\pi^-\pi^+$; (middle right) $D_s^+ \to K^+\pi^+\pi^-/D_s^- \to \pi^-\eta$; (bottom left) $D_s^+ \to K^+\pi^+\pi^-/D_s^- \to \pi^-\eta'$; (bottom right) $D_s^+ \to K^+\pi^+\pi^-/D_s^- \to K^+\pi^+\pi^-$.

APPENDIX B

STUDY OF η DETECTION EFFICIENCY

B.1 Introduction

For D^0 and D^+ decays, data-Monte Carlo efficiency differences were determined by taking ratios between partially reconstructed and fully reconstructed events of given topologies [32]. For example, in the decay $\psi' \to J/\psi\pi^+\pi^- \to \ell^+\ell^-\pi^+\pi^-$, the $\ell^+\ell^-\pi^\mp$ system is reconstructed, the missing mass squared spectrum (peaking at the pion mass squared) is fit to determine the total yield of $\ell^+\ell^-\pi^+\pi^-$ events, and the extra $\pi^\pm$ is identified if possible giving the efficiency.

To investigate η efficiencies and possible data-MC discrepancies, we used the $\sim$ 28 million ψ' events produced in the CLEO-c configuration, in particular utilizing the $\psi' \to J/\psi\eta \to \mu^+\mu^-\eta$ decay.

B.2 Eta Efficiencies From $\psi' \to \eta J/\psi$

We reconstruct J/ψ candidates in the $\mu^+\mu^-$ decay mode. The electron decay is not used to avoid problems with bremsstrahlung and the background of radiative Bhabha scattering events.

Muon candidates are selected by the applying track quality criteria in Table B.1 and requiring E/p (the ratio of calorimeter energy associated with the track to the track momentum) to be less than 0.5. J/ψ candidates consist of oppositely-charged muon candidates with raw invariant mass satisfying $|m_{\mu^+\mu^-} - 3096\ \mathrm{MeV}/c^2| < 30\ \mathrm{MeV}/c^2$; the invariant mass spectrum is shown in Figure B.1. The J/ψ candidates are then vertex- and mass-constrained.

A center of mass (CM) four-vector is obtained in the following manner. Because the actual CM energy of the machine is slightly higher than the mass of the ψ', most events will involve a small amount of radiation (on the order of an MeV). Fixing the CM four-vector to the value reported by CESR produces an

Table B.1: Track quality criteria for η efficiency study

$0.05\ \text{GeV}/c < \lvert\mathbf{p}\rvert < 3\ \text{GeV}/c$
Track has a determined charge
$\lvert d_0\rvert < 5$ mm
$\lvert z_0\rvert < 5$ cm
$\lvert\chi^2\rvert < 10^5$
$\lvert\cos\theta\rvert < 0.93$
Hit fraction > 0.5

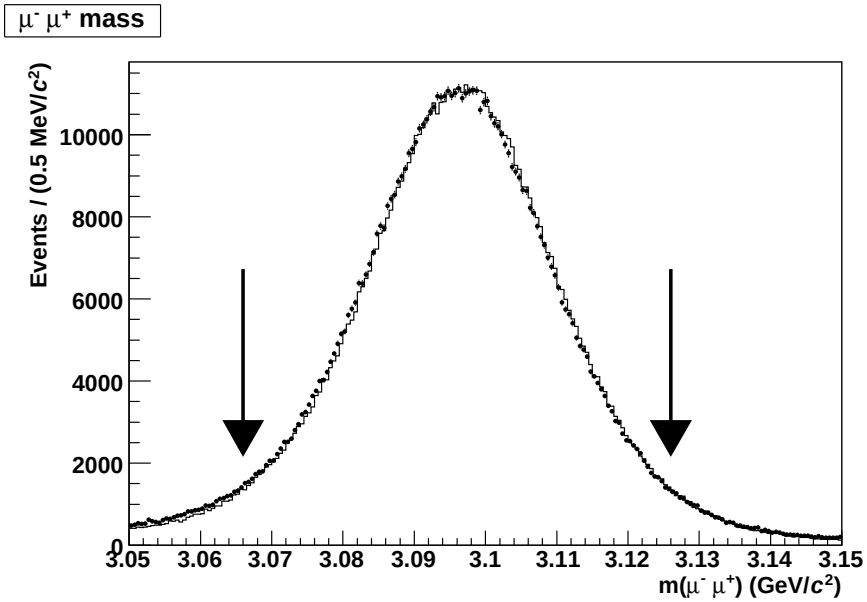

Figure B.1: Invariant mass spectrum of $J/\psi \to \mu^+\mu^-$ candidates. Points are data and histogram is MC. Arrows indicate mass cuts used for the rest of this analysis. This plot (and many later ones) are normalized to equal number of passing $\mu^+\mu^-$ candidates.

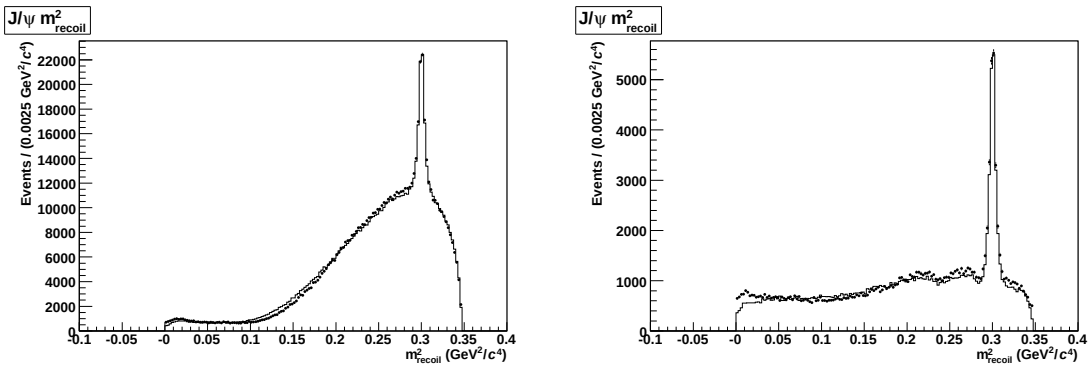

Figure B.2: J/ψ recoil mass squared before (left) and after (right) track and π^0 vetoes.

η mass in data that is too high by 2 MeV/c^2. We create an adjusted four vector by assuming that the three-momentum (from the crossing angle) is unchanged in the radiative process and that the state reached by radiative return has the ψ' mass. The resultant four-vector is thus $[(m^2_{\psi'}+|\mathbf{p}|^2)^{1/2}, \mathbf{p}]$ where $\mathbf{p}$ is obtained from the stated CESR beam energy and crossing angle. Not including the crossing angle causes significant resolution degradation.

The recoil mass squared $m^2_{\rm rec} \equiv |p_{\rm CM} - p_{J/\psi}|^2$ is computed using the adjusted CM and constrained J/ψ four-vectors. A clear peak at the η mass squared is seen on top of a large background primarily due to $\psi' \to \pi\pi J/\psi$.

The η peak lies near the peak of the $J/\psi\pi\pi$ background. Because of this, fitting for the η yield to the desired accuracy requires precise knowledge of both the signal shape and the $J/\psi\pi\pi$ spectrum, neither of which is, unfortunately, available. To reduce the impact of the $J/\psi\pi\pi$ background on the η yield determination, we impose track and π^0 vetoes. After accounting for the J/ψ daughters, any event with extra tracks meeting the quality requirements in Table B.1, or with a reconstructed π^0, is vetoed. This eliminates virtually all of the $J/\psi\pi^+\pi^-$ background and most of the $J/\psi\pi^0\pi^0$ background. In addition, most non-$\gamma\gamma$

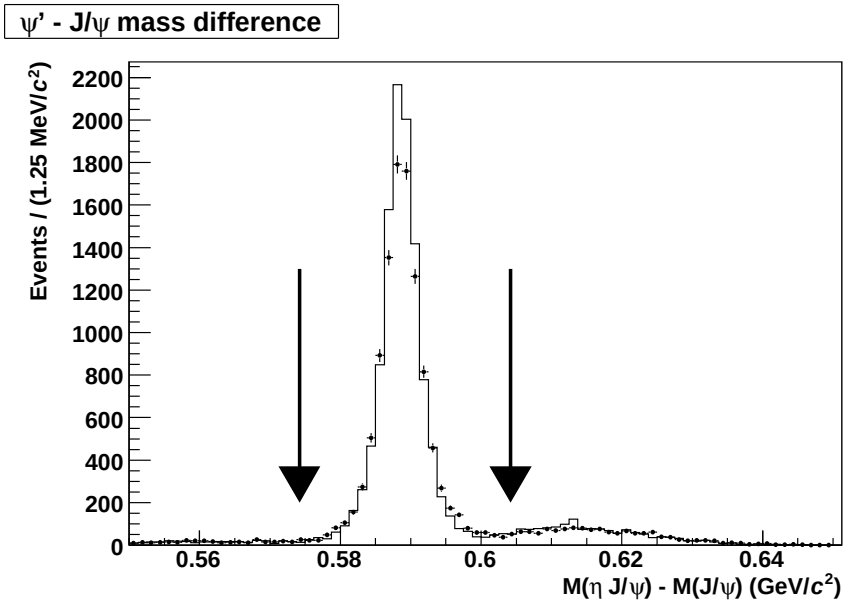

Figure B.3: Distribution of $M(\eta J/\psi) - M(J/\psi)$. The arrows show the accepted region for "found" etas. The broad structure to the right of the peak is due to χ_{cJ} cascades.

decays of the η are rejected. With the vetoes, we come close to a measurement of the efficiency of $\eta \to \gamma\gamma$ reconstruction, not including the branching fraction for that decay. The effect of the vetoes on the recoil mass spectrum are shown in Figure B.2.

We use the same η selection that is used to create D candidates; various properties of the η candidates are compared between data and Monte Carlo in Figures B.6–B.13. An eta candidate is considered "found" if, when combined with the J/ψ candidate, the mass difference between the resulting ψ' candidate and the constrained J/ψ candidate agrees with the 2006 PDG mass difference, 589.188 MeV/c^2 [19], to within 15 MeV/c^2, as shown in Figure B.3.

The J/ψ events are separated into "found" and "not found" samples. The remaining η's that do not decay to $\gamma\gamma$ are in the "not found" sample. These two samples are statistically independent.

The non-$J/\psi\pi\pi$ background considered in both samples is the two-photon cascade $\psi' \to \gamma\chi_{cJ} \to \gamma\gamma J/\psi$.

In the nominal fits (for both data and generic Monte Carlo), the following components are specified:

- The η **signal lineshape** is the sum of a narrow Gaussian and a wide Crystal Ball function [34], where the relative parameters of the two functions are determined from Monte Carlo of the $J/\psi\eta$ decay. The same shape is used for the signal in both the "found" and "not found" samples. The mean and overall width are allowed to float during the fit.
- The **dipion background** is parametrized by a 4th order polynomial in the "not found" sample. In the "found" sample the shape is obtained from a histogram of Monte Carlo events. The relative ratio between the "found" and "not found" contributions is fixed to the ratio found using MC truth tagging.
- The χ_{cJ} **background** shapes are histograms determined from generic Monte Carlo, which is also used to fix the relative sizes of the "found" and "not found" samples. The size of this background is absolutely normalized based on the number of $J/\psi \to \mu^+\mu^-$ events accepted.

The results of the fits are shown in Figures B.4 and B.5.

The result of interest is the following ratio:

$$\epsilon_{\text{eff}} \equiv \frac{Y_{\text{found}}}{Y_{\text{found}} + Y_{\text{not found}}}$$

where Y_{found} and $Y_{\text{not found}}$ are the η signal yields in the "found" and "not found" samples, respectively.

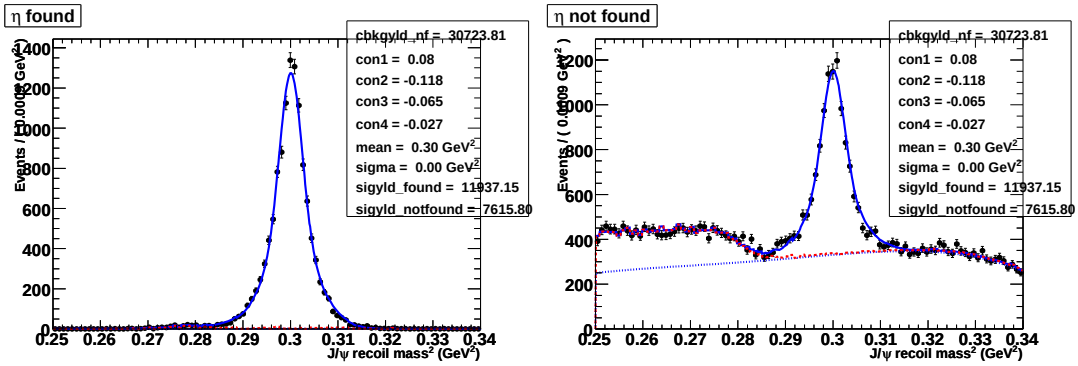

Figure B.4: Nominal fit to generic Monte Carlo sample.

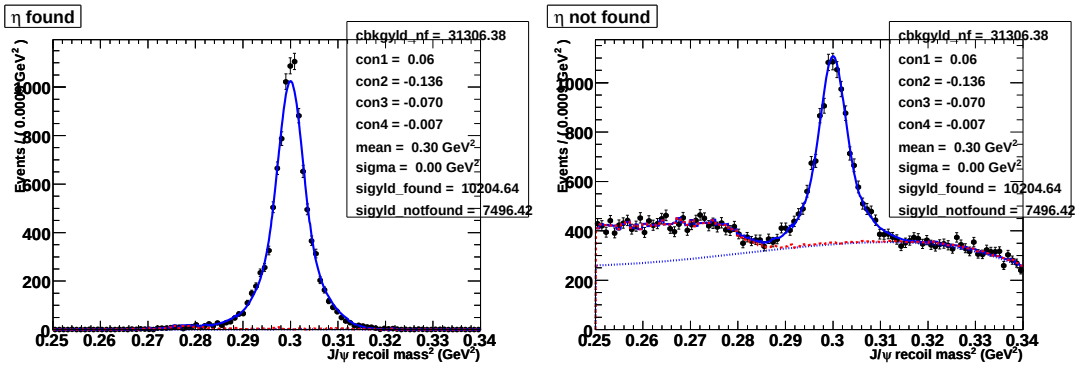

Figure B.5: Nominal fit to data sample.

Table B.2: Fit results, efficiencies, and data/MC discrepancies.

	Data	MC
Y_{found}	10205 ± 102	11937 ± 110
$Y_{\text{not found}}$	7496 ± 164	7616 ± 156
ϵ_{eff} (%)	57.6 ± 0.6	61.1 ± 0.5
Ratio − 1 (%)	−5.6 ± 1.3	

B.2.1 Systematic Checks

We consider the following sources of uncertainty in this measurement; the results of the checks are shown in Table B.3.

- **Dipion background shape.** We use a 5th order polynomial instead of a 4th order one. Because the background shape is not fixed, variations will occur because of changes in the other fit components, which are discussed below.

- **Signal lineshape.** We assume that all observed "found" events in fact arise from $\eta \to \gamma\gamma$ and use a histogram of such events to fit for the η peak in the "not found" events.

- χ_{cJ} **background normalization.** We have assumed that the absolute normalization of the χ_{cJ} background is known. We can relax this and let the number of χ_{cJ} events float. While the favored χ_{cJ} yield is 42% less in data and 22% less in Monte Carlo than is predicted, the changes in ϵ_{eff} are quite small. (The large change in the yield is a consequence of not having a good handle on what the $\pi\pi$ spectrum should be.)

- **Track and** π^0 **vetoes.** There are two effects to consider. The first is whether the efficiency for reconstructed $\eta \to \gamma\gamma$ events to pass the vetoes is the same for data and Monte Carlo. We compare the change in size of the "found" sample for both data and Monte Carlo when the veto is applied and when it is lifted. The efficiency in MC is 99.1%, while the efficiency in data is 98.7%. We conclude that the two agree to within 0.4%.

  The second effect is the *inefficiency* of the vetoes in rejecting other η decays, which contribute to the "not found" peak. Monte Carlo and data π^0 reconstruction efficiencies differ by $\sim$ 4%, which means that the efficiency for

Table B.3: Relative changes in ϵ_{eff} due to various systematic uncertainties.

Systematic	Data	MC
$\pi\pi$ background parametrization	−0.01%	−0.18%
η lineshape	+0.20%	−0.33%
χ_{cJ} normalization	−0.18%	−0.11%
$\eta \to \gamma\gamma$ passes veto	−0.4%	—
Other η decays in "not found" sample	—	−0.8%

vetoing $\eta \to 3\pi^0$ differs by $\sim 12\%$. Almost all η decays with charged pions are rejected by the track veto, so the $3\pi^0$ mode dominates the remaining decays.

In Monte Carlo, we find that 5.6% of the total number of η events (both "found" and "not found") arise from decays other than $\eta \to \gamma\gamma$. If we assume that this number is wrong by up to 15%, the total number of passing η events (the denominator in determining ϵ_{eff}) changes by 0.8%.

B.3 Interpretation

It is known that the photon energy resolution function is not modeled perfectly in the Monte Carlo, and smearing due to resolution is underestimated in the data when performing kinematic constraints; this gives rise to a known source of data-MC efficiency discrepancy. We repeated the analysis with new data and MC samples where the assumed errors are inflated for data and where extra smearing is applied to MC events. The data/MC difference changes to -3.3% when this is done.

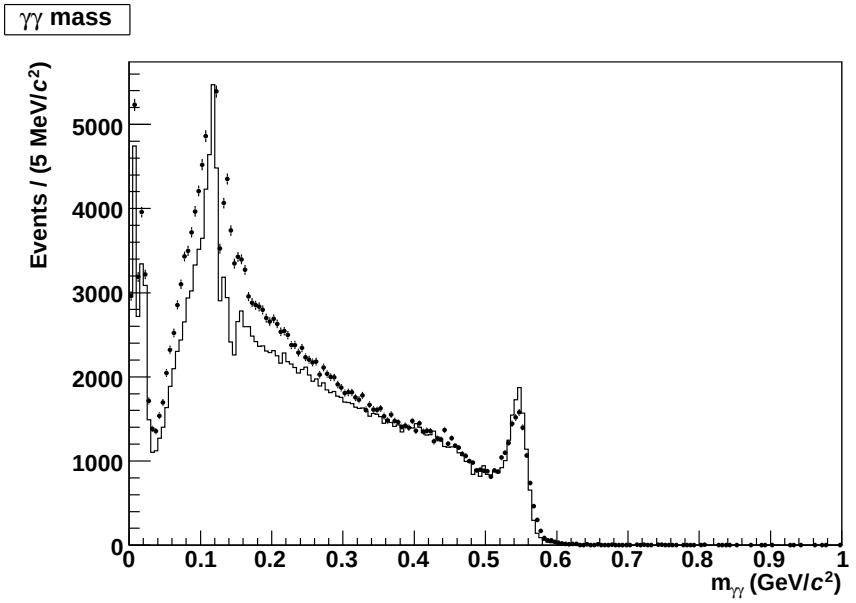

Figure B.6: $\gamma\gamma$ mass

For the purposes of the D_s^+ branching fraction analysis, η efficiencies in the MC are corrected by -5.6% when applied to data. The uncertainty used for this correction is 4.0%; this is obtained by adding in quadrature the statistical uncertainty in the ratio measurement, the systematic uncertainties listed in Table B.3, the unexplained remaining 3.3% discrepancy when extra photon energy resolution smearing is added, and an assumed 2.0% for the extrapolation from low momentum η candidates (as here) to high momentum (as in $D_s^+ \to \pi^+\eta$ for example).

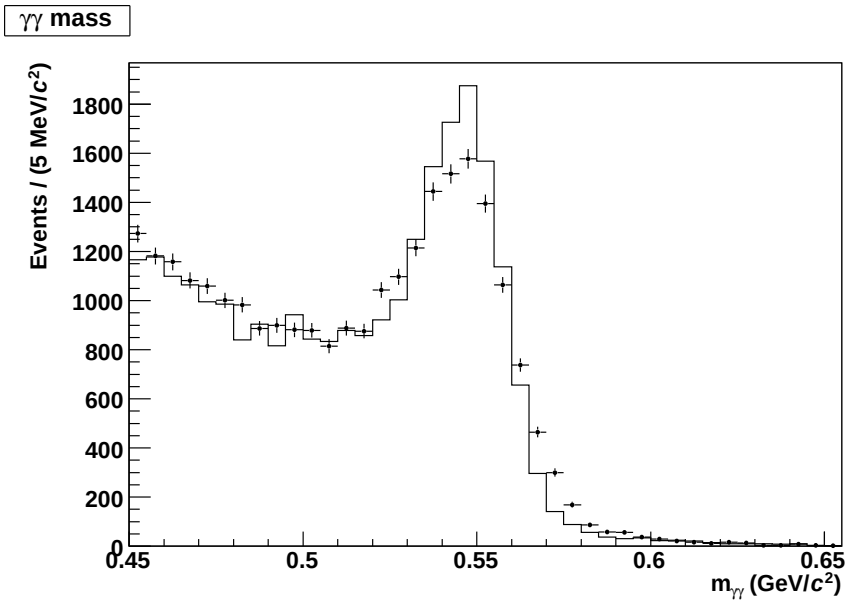

Figure B.7: $\gamma\gamma$ mass, zoomed in to η peak

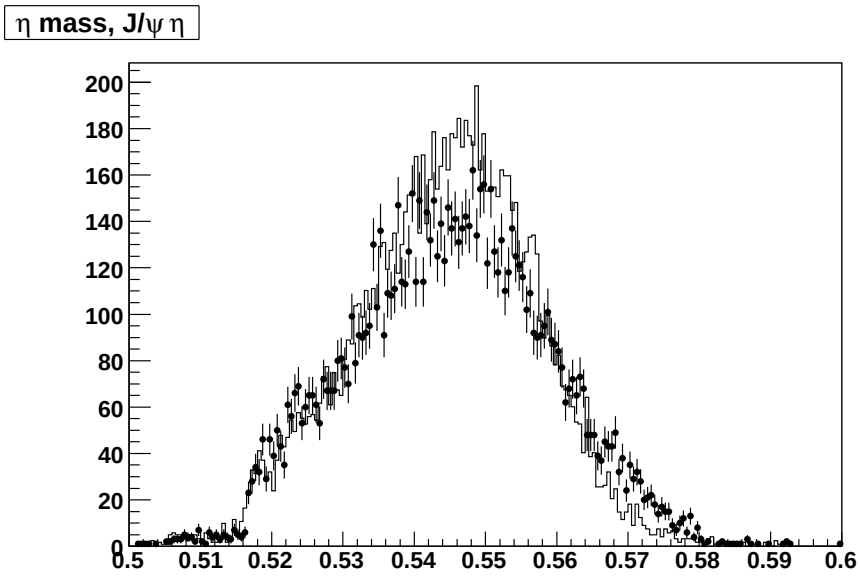

Figure B.8: η candidate mass (used η candidates, after pull mass cut)

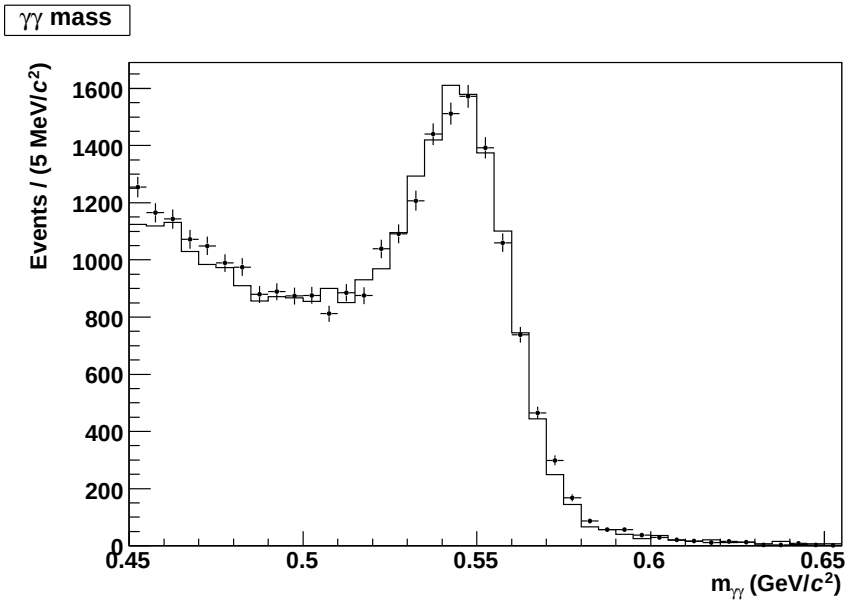

Figure B.9: $\gamma\gamma$ mass, data and MC smearing applied

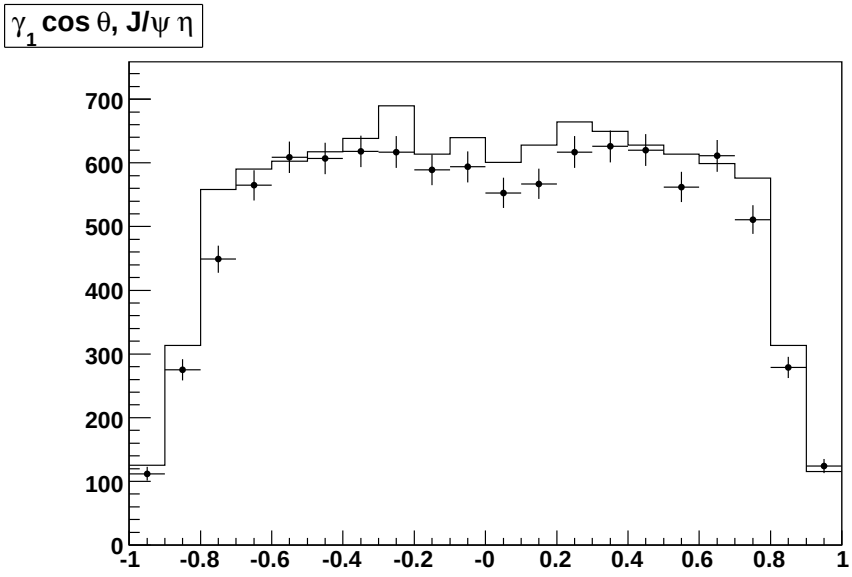

Figure B.10: $\cos(\theta_{\gamma_1})$, nominal η candidates

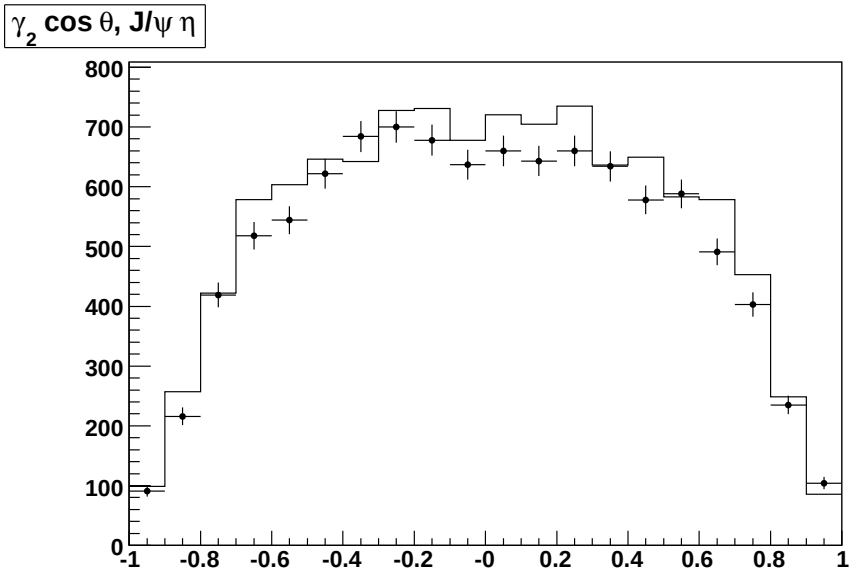

Figure B.11: $\cos(\theta_{\gamma_2})$, nominal η candidates

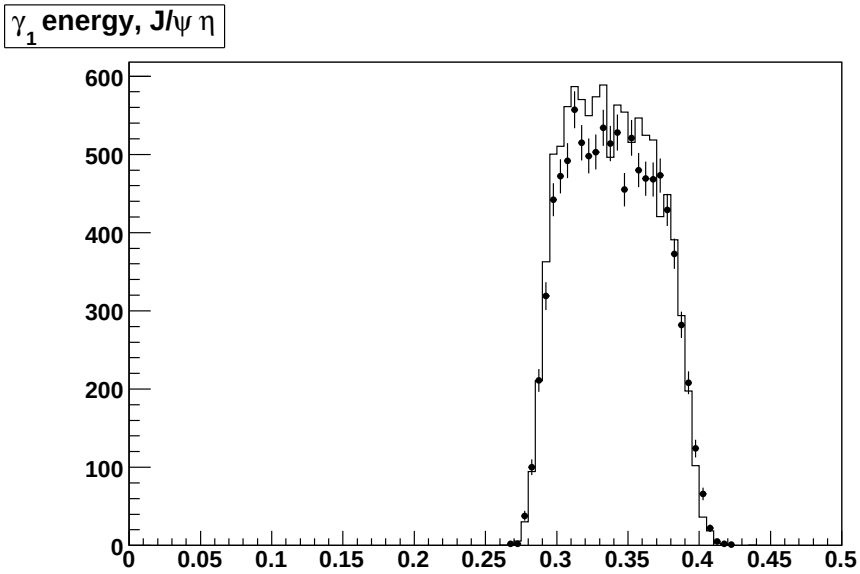

Figure B.12: E_{γ_1}, nominal η candidates

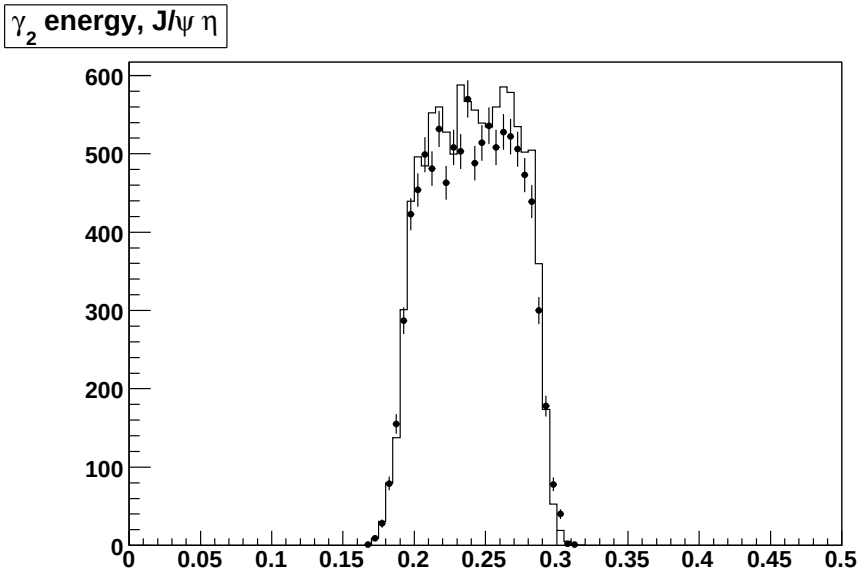

Figure B.13: E_{γ_2}, nominal η candidates

BIBLIOGRAPHY

[1] P. Ramond, *Journeys Beyond the Standard Model* (Perseus, 1999).

[2] L.-L. Chau and H.-Y. Cheng, Phys. Rev. D **36**, 137 (1987).

[3] E. Follana *et al.*, Phys. Rev. Lett. **100**, 062002 (2008), arxiv:0706.1726.

[4] C. Aubin *et al.*, Phys. Rev. Lett. **94**, 011601 (2005), hep-ph/0408306.

[5] CDF Note 7925, URL http://www-cdf.fnal.gov/physics/new/bottom/060316.blessed-bsdsds/DsDs_public.ps.

[6] B. Aubert *et al.* (BaBar Collaboration), Phys. Rev. Lett. **98**, 141801 (2007), hep-ex/0607094.

[7] ALEPH, DELPHI, L3, OPAL, and SLD Collaborations, Phys. Rept. **427**, 257 (2006), hep-ex/0509008.

[8] K. M. Ecklund *et al.* (CLEO Collaboration), Phys. Rev. Lett. **100**, 161801 (2008), arxiv:0712.1175.

[9] J. Z. Bai *et al.* (BES Collaboration), Phys. Rev. D **56**, 3779 (1997).

[10] J. Z. Bai *et al.* (BES Collaboration), Phys. Rev. D **52**, 3781 (1995).

[11] M. Artuso *et al.* (CLEO Collaboration), Phys. Lett. B **378**, 364 (1996).

[12] B. Aubert *et al.* (BaBar Collaboration), Phys. Rev. D **71**, 091104 (2005), hep-ex/0502041.

[13] B. Aubert *et al.* (BaBar Collaboration), Phys. Rev. D **74**, 031103 (2006), hep-ex/0605036.

[14] R. M. Baltrusaitis *et al.* (MARK-III Collaboration), Phys. Rev. Lett. **56**, 2140 (1986).

[15] J. Adler *et al.* (MARK-III Collaboration), Phys. Rev. Lett. **60**, 89 (1988).

[16] J. Adler *et al.* (MARK-III Collaboration), Phys. Rev. Lett. **64**, 169 (1990).

[17] CLEO-c/CESR-c Taskforces & CLEO-c Collaboration, Cornell LEPP preprint CLNS 01/1742 (2001) (unpublished).

[18] D. Peterson *et al.*, Nucl. Instrum. Meth. A **478**, 142 (2002).

[19] W.-M. Yao *et al.* (Particle Data Group), J. Phys. G **33**, 1 (2006), and 2007 partial update for the 2008 edition.

[20] R. Fruhwirth, Nucl. Instrum. Meth. A **262**, 444 (1987).

[21] M. Artuso *et al.*, Nucl. Instrum. Meth. A **554**, 147 (2005), physics/0506132.

[22] Y. Kubota *et al.* (CLEO Collaboration), Nucl. Instrum. Meth. A **320**, 66 (1992).

[23] Gollin *et al.*, IEEE Trans. Nucl. Sci. **48**, 547 (2001); Hans *et al.*, *ibid.*, 552; Selen *et al.*, *ibid.*, 562.

[24] A. Wolf *et al.*, Comput. Phys. Commun. **110**, 91 (1998).

[25] A. Osterheld *et al.*, SLAC-PUB-4160.

[26] J. Z. Bai *et al.* (BES Collaboration), Phys. Rev. Lett. **88**, 101802 (2002), hep-ex/0102003.

[27] D. Cronin-Hennessy *et al.* (CLEO Collaboration) (2008), arXiv:0801.3418.

[28] D. J. Lange, Nucl. Instrum. Meth. A **462**, 152 (2001).

[29] P. Avery *et al.*, *QQ: The CLEO Event Generator*, (unpublished), URL http://www.lns.cornell.edu/public/CLEO/soft/QQ.

[30] E. A. Kuraev and V. S. Fadin, Sov. J. Nucl. Phys. **41**, 466 (1985).

[31] R. Brun et al., GEANT 3.21, CERN Program Library Long Writeup W5013 (1993) (unpublished).

[32] S. Dobbs *et al.* (CLEO Collaboration), Phys. Rev. D **76**, 112001 (2007), arXiv:0709.3783.

[33] B. Andersson, G. Gustafson, *et al.*, Phys. Rept. **97**, 31 (1983).

[34] J. Gaiser, Ph.D. thesis, SLAC (1982), SLAC-0255.

[35] D. Cassel, *Partial* $D_s^+ \to K^-K^+\pi^+$ *Branching Fractions and* $\mathcal{B}(D_s^+ \to \phi\pi^+)$, CLEO CBX 07-37 (unpublished).

[36] F. Ambrosino *et al.* (KLOE Collaboration), Eur. Phys. J. C **48**, 767 (2006), hep-ex/0601025.

[37] I. Brock and R. Briere, *Pion and Kaon Identification Efficiencies for CLEO-c*, CLEO CBX 05-43 (unpublished).

[38] E. M. Aitala *et al.* (E791 Collaboration), Phys. Rev. Lett. **86**, 765 (2001), URL http://link.aps.org/abstract/PRL/v86/p765.

[39] D. Alde *et al.* (LAPP Collaboration), Phys. Lett. B **177**, 115 (1986).

[40] J. M. Link *et al.* (FOCUS Collaboration), Phys. Lett. B **601**, 10 (2004), hep-ex/0407014.